UNIVERSITY OF CALIFORNIA

Los Angeles

Free-Breathing Radial Magnetic Resonance Imaging Quantification of Fat and R_2*

A dissertation submitted in partial satisfaction of the

requirements for the degree Doctor of Philosophy

in Biomedical Physics

by

Tess Armstrong

2018

ABSTRACT OF THE DISSERTATION

Free-Breathing Radial Magnetic Resonance Imaging Quantification of Fat and R_2*

by

Tess Armstrong

Doctor of Philosophy in Biomedical Physics

University of California, Los Angeles, 2018

Professor Holden H. Wu, Chair

Purpose

Magnetic resonance imaging (MRI) can non-invasively quantify fat and the transverse relaxation rate (R_2*) in the human body. This quantitative information can provide further insight about diseases such as non-alcoholic fatty liver disease (NAFLD), obesity, and ischemic placental disease (IPD). Conventional MRI methods for quantifying fat and R_2* require breath-holding, which limits the spatial resolution, volumetric coverage, and signal-to-noise ratio that may be achieved. Moreover, several subject populations, including sick, elderly, and mentally impaired patients, as well as children, infants, and pregnant women, may have difficulty performing a breath-hold or are unable to breath-hold. The purpose of this work is to develop and evaluate a new free-breathing 3D stack-of-radial MRI technique (FB radial) for fat and R_2*

quantification at 3 Tesla (T) that overcomes the aforementioned limitations of conventional breath-holding MRI.

Methods

To enable free-breathing MRI, a multiecho golden-angle ordered 3D stack-of-radial radiofrequency-spoiled gradient echo sequence with gradient calibration and correction (FB radial) was developed. First, to evaluate FB radial without motion, fat quantification accuracy using FB radial was compared to conventional Cartesian and reference single-voxel magnetic resonance spectroscopy (SVS) sequences using a fat fraction phantom and in the pelvis of five healthy subjects at 3 T. To evaluate FB radial fat quantification accuracy in subjects capable of breath-holding, a population consisting of eleven healthy adults were recruited and imaged at 3 T. The fat quantification accuracy of FB radial was compared to conventional breath-held Cartesian (BH Cartesian) MRI and reference breath-held SVS (BH SVS).

The feasibility and repeatability of FB radial for hepatic fat quantification was evaluated in children, which represents a population that may have limited breath-hold ability or may have difficulty complying with operator instructions. Ten healthy children and nine overweight children with NAFLD, 7-17 years of age, were imaged at 3 T using FB radial, BH Cartesian and BH SVS. Acquisitions were performed twice to assess repeatability. Images and proton-density fat fraction (PDFF) maps were scored for image quality. Liver coverage was measured.

Ten healthy infants aged 2-7 months were recruited to evaluate the feasibility of FB radial for quantifying hepatic fat and body composition in a population incapable of breath-holding. The preparation time and scan time (median ± interquartile range) for each non-sedated MRI exam was recorded. Abdominal and head and chest FB radial scans and abdominal Cartesian scans were performed. Abdominal scans were scored for motion artifacts by a

radiologist, masked to the trajectory. Visceral adipose tissue (VAT), subcutaneous adipose tissue (SAT), and brown adipose tissue (BAT) (volume and PDFF) and hepatic PDFF were measured using FB radial. Repeatability of FB radial hepatic PDFF was assessed.

To evaluate the quantitative accuracy of FB radial for R_2* mapping without motion, FB radial was compared to a conventional Cartesian sequence using a R_2* phantom. To evaluate FB radial R_2* mapping in the presence of motion, thirty subjects with normal pregnancies and three subjects with ischemic placental disease (IPD) were scanned twice: between 14-18 and 19-23 weeks gestational age (GA). Feasibility and repeatability of FB radial placental R_2* mapping was assessed. The mean and spatial coefficient of variation (CV) of placental R_2* was determined for all subjects, and separately for anterior and posterior placentas, at each GA range.

For all analyses, quantitative accuracy of fat or R_2* quantification was evaluated using linear correlation (Pearson's correlation coefficient, r; Lin's concordance correlation coefficient, ρ_c) and Bland-Altman analyses (mean difference, MD; limits of agreement, LoA = MD ± 1.96 × standard deviation). The repeatability of FB radial between back-to-back scans for fat or R_2* quantification was assessed by calculating the within-technique mean difference (MD_{within}) and the coefficient of repeatability (CR). To compare image quality between FB radial and BH Cartesian, differences in the distribution of scores between FB radial and Cartesian were determined using McNemar-Bowker tests. For all statistical analyses, a p-value (P) < 0.05 was considered significant.

Results

In a fat fraction phantom, FB radial demonstrated accuracy with r and $\rho_c > 0.995$ ($P < 0.001$), absolute MD < 2.2 ± 4.9% compared to SVS and absolute MD < 0.6 ± 3.3% compared to Cartesian. In the pelvis of healthy adults, FB radial demonstrated fat quantification accuracy with

absolute MD < 1.2 ± 3.2% in low fat fraction regions (< 5% PDFF) and absolute MD < 4.6 ± 5.6% in high fat fraction regions (> 80% PDFF). In the liver and abdomen, PDFF showed significant correlation ($\rho > 0.986$, $\rho_c > 0.985$), and absolute MD < 1.0 ± 10.6% between FB radial and BH SVS, and significant correlation ($r > 0.996$, $\rho_c > 0.995$), and absolute MD < 0.9 ± 5.7% between FB radial and BH Cartesian.

In children with NAFLD, FB radial demonstrated significantly less motion artifacts compared to BH Cartesian ($P < 0.05$). FB radial PDFF demonstrated a linear relationship ($P < 0.001$) versus BH SVS PDFF and BH Cartesian PDFF with $r = 0.996$ and $\rho_c = 0.994$, and $r = 0.997$ and $\rho_c = 0.995$, respectively. The absolute MD in PDFF between FB radial, BH Cartesian, and BH SVS was less than 0.7 ± 2.6% Repeated FB radial had $MD_{within} = 0.25\%$ and CR = 1.53% for PDFF.

Ten infants were enrolled, and nine infants completed the study (90% completion). The preparation time and scan time were 32 ± 7 min and 24 ± 11 min, respectively. FB radial MRI demonstrated significantly higher image quality scores compared to Cartesian MRI ($P = 0.01$). The measurements using FB radial were VAT = 48.2 ± 16.5 cm^3; VAT-PDFF = 41.6 ± 3.8%; SAT = 281.6 ± 104.5 cm^3; SAT-PDFF = 86.1 ± 4.8%; BAT = 1.5 ± 0.6 cm^3; and BAT-PDFF = 28.9 ± 8.8%. Hepatic PDFF measured using FB radial was 3.5 ± 1.1% and had repeatability of $MD_{within} < 0.25\%$ and CR < 2.0%.

For R_2* mapping, FB radial demonstrated accurate ($\rho_c \geq 0.996$; $P < 0.001$; absolute MD < 0.2 ± 4 s^{-1}) and repeatable ($MD_{within} = 0.23$ s^{-1}; CR = 3.9 s^{-1}) quantification in a phantom, and repeatable ($MD_{within} < 0.5$ s^{-1}; CR ≤ 4.6 s^{-1}) quantification in thirty subjects with normal pregnancies. At 3T, placental R_2* mean ± standard deviation was 12.9 ± 2.7 s^{-1} for 14-18 and 13.2 ± 1.9 s^{-1} for 19-23 weeks GA. The CV was significantly greater ($P = 0.043$) at 14-18 (0.63 ±

0.12) than 19-23 (0.58 ± 0.13) weeks GA. At 19-23 weeks, the CV was significantly lower ($P < 0.001$) for anterior (0.49 ± 0.08) than posterior (0.67 ± 0.11) placentas. One IPD subject had a lower mean R_2* than normal subjects at both GA ranges ($\hat{Z} < -2$).

Conclusion

FB radial demonstrated quantitative accuracy compared to BH techniques in a fat fraction phantom and in the pelvis and liver of healthy volunteers. In healthy children and children with NAFLD, non-sedated free-breathing radial MRI provided accurate and repeatable hepatic PDFF measurements and improved image quality, compared to standard breath-held MR techniques. Finally, in a R_2* phantom FB radial provided accurate and repeatable three-dimensional R_2* mapping and in pregnant subjects FB radial provided repeatable R_2* mapping in the entire placenta at 3T during early GA.

The dissertation of Tess Armstrong is approved.

Grace Hyun Jung Kim

Kara Lynee Calkins

Peng Hu

Kyunghyun Sung

Holden H. Wu, Committee Chair

University of California, Los Angeles

2018

This is dedicated to

Peter, Sharon, and Aaron

TABLE OF CONTENTS

LIST OF TABLES

LIST OF FIGURES

LIST OF EQUATIONS

ACKNOWLEDGEMENTS

I would like to express my greatest thanks to my advisor Dr. Holden H. Wu who has helped me throughout the PhD process by giving me advice, feedback and opportunities. He has helped me to work on great projects that I have enjoyed tremendously and has given me the opportunity to present these projects to the scientific community.

I would like to thank my collaborators from Pediatrics, Radiology, and Obstetrics and Gynecology. Specifically, I would like to give special thanks Dr. Kara L. Calkins, Dr. Shahnaz Ghahremani, Dr. Grace Hyun J. Kim, Dr. Ely Felker, Karrie V. Ly, Dr. Rinat Masamed, Dr. Carla Janzen, Smruthi Murthy, Teresa Chanlaw, Dr. Sherin U. Devaskar, Dr. Joanna Yeh, Sarai Santos, Irish Del Rosario, Margarida Y. Y. Lei, and Sitaram Vangala. It has been a joy getting to know everyone and working together on exciting projects. These collaborations have helped me greatly to expand my knowledge in the field.

I would like to thank the students and faculty in MRRL and at UCLA who have had helpful discussions with me and provided feedback on my research. Specifically, I would like to thank Dr. Kyunghyun Sung, Dr. Peng Hu, and Dr. Daniel Ennis who have given me great advice and feedback throughout my PhD career. I would also like to thank the students I have worked alongside, Andres Saucedo, Dr. Thomas Martin, Dr. Fei Han, Dr. Dapeng Liu, Dr. Ziwu Zhou, Dr. Le Zhang, Xinzhou Li, Yu Gao, Samantha Mikiael, Cass Wong, Jiahao Lin, Xinran Zhong, Fadil Ali, Chang Gao, Alibek Danyalov, and Dr. Victoria Yu. They have given me support and it has been fun working alongside these students.

I would also like to thank the MR technologists at UCLA for all of their help with scanning patients and teaching me scanning techniques. Thank you Sergio Godinez and Glen

Nyborg for being supportive and helping me with my projects. I would also like to thank Barbara Lee and Tammy Floore for helping with our studies and subject recruitment.

I would like to give thanks to our collaborators at Siemens, Dr. Xiaodong Zhong, Dr. Alto Stemmer, Dr. Xiaoming Bi, Dr. Yutaka Natsuaki, Dr. Berthold Kiefer, Dr. Stephan Kannengiesser, and Dr. Gerhard Laub. You have been a great help with my project and have helped me develop my skills in sequence programming.

I would like to thank the students and the faculty in the department of Physics and Biology in Medicine. The students have helped and supported me throughout my PhD career. I would also specifically like to thank Reth Im and Dr. Michael McNitt-Gray who have been great supporters and have helped me navigate the University of California Los Angeles. I would also like to thank the late Terry Moore, who welcomed me into the program and helped me during the beginning stages of my PhD career.

I would like to thank my boyfriend, Aaron Scheffler, who has been with me during the ups and downs and has motivated me throughout my PhD career. Last but not least, I would like to thank my parents, Sharon and Peter Armstrong who have supported me my entire life. They have inspired me to work hard and strive to be the best I can be. I would also like to thank my brothers, who have also motivated me throughout my life. I could not have done this without all of your support.

VITA

EDUCATION

2012 – 2016	University of California Los Angeles M.S., Biomedical Physics	Los Angeles, CA
2008 – 2012	University of Miami B.S., Physics, minors in Mathematics and Chemistry	Coral Gables, FL
2008 – 2012	University of Miami B.S., General Engineering Science	Coral Gables, FL

HONORS & AWARDS

2018	Physics and Biology in Medicine IDP Moses A. Greenfield Award
2018	RSNA Trainee Research Prize
2017, 2018	ISMRM Summa Cum Laude Award
2016, 2017, 2018	ISMRM Magna Cum Laude Award
2015, 2016, 2017	ISMRM Educational Stipend
2012 – 2014	NIH Training Grant
2012	Joseph Hirschberg Prize in Physics
2008 – 2012	University of Miami President's Honor Roll
2008 – 2012	University of Miami PRISM Honors Program
2008 – 2012	University of Miami General Honors Program
2008	Florida Engineer Society Student Scholarship: Tampa Chapter

First Author Peer Reviewed Publications

1. **Armstrong T**, Ly KV, Ghahremani S, Calkins KL, Wu HH. Free-breathing 3D quantification of infant body composition and hepatic fat using a stack-of-radial MRI technique. Pediatric Radiology. *(Under Review)*
2. **Armstrong T**, Liu D, Martin T, Masamed R, Janzen Carla, Wong C, Chanlaw T, Devaskar SU, Sung K, and Wu HH. 3D R_2* mapping of the placenta during early gestation using free-breathing multiecho stack-of-radial MRI at 3 T. Journal of Magnetic Resonance Imaging 2018; Early View. doi: 10.1002/jmri.26203
3. **Armstrong T**, Ly KV, Murthy S, Ghahremani S, Kim GHJ, Calkins KL, Wu HH. Free-breathing quantification of hepatic fat in healthy children and children with nonalcoholic fatty liver disease using a multi-echo 3-D stack-of-radial MRI technique. Pediatric Radiology 2018; 48(7):941-953. doi: 10.1007/s00247-018-4127-7
4. **Armstrong T**, Dregely I, Stemmer A, Han F, Natsuaki Y, Sung K, Wu HH. Free-breathing liver fat quantification using a multiecho 3D stack-of-radial technique. Magnetic Resonance in Medicine 2018; 79(1):370-382. doi: 10.1002/mrm.26693

Co-Author Peer Reviewed Publications

5. Martin T, **Armstrong T**, Danyalov A, Lee E, Felker E, Sayre J, Raman S, Wu H, Sung K, Evaluation of fat-only SGS (SGSF) for respiratory motion extraction and compensation in the liver. Magnetic Resonance in Medicine. *(Under Review)*

6. Martin T, Liu D, Li X, Del Rosario I, Chanlaw T, Choi S, Devaskar S, Janzen C, **Armstrong T**, Masamed R, Wu H, Sung K, MRI characterization of uterine motion in early gestation using image-based motion tracking. Journal of Magnetic Resonance Imaging. *(Under Review)*
7. Ly KV, **Armstrong T**, Murthy S, Yeh J, Ghahremani S, Kim GHJ, Wu HH, Calkins KL. Free-breathing magnetic resonance imaging for the diagnosis of pediatric non-alcoholic fatty liver disease. Journal of Pediatrics. *(Under Review)*
8. Qi XS, Santhanam A, Neylon J, Min Y, **Armstrong T**, Sheng K, Staton RJ, Pukala J, Pham A, Low DA, Lee SP, Steinberg M, Manon R, Chen AM, Kupelian P. Near real-time assessment of anatomic and dosimetric variations for head and neck radiation therapy via graphics processing unit-based deformation framework. International Journal of Radiation Oncology Biology Physics. 2015; 92:415–422.

Selected Conference Abstracts: Oral Presentations

1. **Armstrong T**, Ly KV, Wang Y, Martin T, Ghahremani S, Sung K, Calkins KL and Wu HH. Free-breathing hepatic fat quantification in children and infants using a 3D stack-of-radial technique: assessment of accuracy and repeatability. In: Proceedings of the 26th Annual Meeting of ISMRM, Paris, France, 2018; p 522. **Summa Cum Laude Award.**
2. **Armstrong T**, Liu D, Martin T, Wong C, del Rosario I, Devaskar SU, Janzen C, Chanlaw T, Masamed R, Sung K, Wu HH. Free-breathing R_2* mapping in the entire placenta during early gestation using 3D stack-of-radial MRI at 3 T: investigation of spatial and temporal variation. In: Proceedings of the 26th Annual Meeting of ISMRM, Paris, France, 2018; p 1185. **Magna Cum Laude Award.**
3. **Armstrong T**, Ly K, Ghahremani S, Yeh J, Calkins KL, Wu HH. Free-breathing pediatric liver MRI using a multiecho 3D stack-of-radial technique enables accurate and repeatable liver fat quantification. In: Proceedings of the 103rd Scientific Assembly and Annual Meeting of RSNA, Chicago, Illinois, United States, 2017; **RSNA Trainee Research Prize.**
4. **Armstrong T**, Martin T, Stemmer A, Li X, Natsuaki Y, Sung K, Wu HH. Free-breathing fat quantification in the liver using a multiecho 3D stack-of-radial technique: investigation of motion compensation and quantification accuracy. In: Proceedings of the 25th Annual Meeting of ISMRM, Honolulu, Hawaii, United States, 2017; p 0363. **Summa Cum Laude Award.**
5. **Armstrong T**, Liu D, Martin T, Stemmer A, Natsuaki Y, Sherin DU, Janzen C, Chanlaw T, Masamed R, Margolis D, Sung K, Wu HH. Free-breathing R_2* characterization of the placenta during normal early gestation using a multiecho 3D stack-of-radial technique. In: Proceedings of the 25th Annual Meeting of ISMRM, Honolulu, Hawaii, United States, 2017; p 0117.
6. **Armstrong T**, Dregely I, Han F, Zhou Z, Sung K, Hu P, Wu H. Free-breathing fat-water-separated liver MRI using a multi-echo 3D stack-of-stars technique. In: Proceedings of the 23rd Annual Meeting of ISMRM, Toronto, Canada, 2015; p 0143. **Magna Cum Laude Award.**

1 INTRODUCTION

Obesity has become a global epidemic with prevalence rates tripling since 1975[1]. Globally, overweight and obesity currently affects an estimated 1.9 billion adults, 340 million children from 5-19 years of age, and 41 million children under 5 years of age[1]. Obesity is associated with metabolic syndrome, a collection of symptoms that include insulin resistance, dyslipidemia, hypertension, and non-alcoholic fatty liver disease (NAFLD)[2–4]. NAFLD, defined as the intracellular accumulation of >5% triglycerides in the hepatocytes[5], ranges from simple steatosis to non-alcoholic steatohepatitis (NASH), which is hallmarked by liver fibrosis[6,7]. Fibrosis culminates in cirrhosis and can lead to hepatocellular carcinoma and liver failure[5,7,8]. For these reasons, NAFLD is currently the number two indication for liver transplant in adults[9]. Liver biopsies are considered the gold standard for diagnosing and staging steatosis[10,11]. However, liver biopsies are costly, invasive, require anaesthesia, can be technically challenging, and are limited by sampling bias[12,13]. Non-invasive magnetic resonance techniques have been developed to quantify hepatic fat. Magnetic resonance spectroscopy (MRS) is regarded as a

reference standard for non-invasive fat quantification[14,15] and accurately quantifies hepatic steatosis[16–18]; however, MRS is also limited by spatial sampling bias[14,15].

Body composition analysis is a valuable tool to provide information about the amount, distribution, and content of adiposity beginning at an early age and throughout later stages of life to provide insight regarding the risk of metabolic syndrome[19–21]. Body composition involves quantifying the volume and/or tissue fat content of visceral adipose tissue (VAT), subcutaneous adipose tissue (SAT), brown adipose tissue (BAT), and other organs[19–21].

Preeclampsia, intrauterine growth restriction (IUGR), and placental abruption are obstetrical conditions associated with placental hypoxia and are collectively referred to as ischemic placental disease (IPD)[22–26]. IPD conditions account for more than half of all medically indicated preterm births less than 35 weeks in the United States[22,23,26,27] and contribute to higher rates of infant and maternal morbidity and mortality[23]. Uterine artery (UA) Doppler can be used to detect IPD[26]; however, UA Doppler has low sensitivity for the detection of IPD[26,28], particularly during early gestation and for low risk pregnancies[26,29]. Development of accurate methods to predict or detect IPD early in pregnancy would be of great importance to enable prevention strategies and improve outcomes[26]. MRI can be used to characterize oxygenation in the placenta through quantification of the transverse relaxation rate ($R_2^* = 1/T_2^*$)[30–33]. R_2^* is known to increase due to local field inhomogeneities caused by deoxyhemoglobin. Thus, R_2^* is higher (or T_2^* is lower) in hypoxic tissues than in normoxic tissues[30–33].

The MRI gradient echo signal model contains contributions from the proton-density of fat, the proton-density of water, and R_2^*[34–36]. Therefore, a multiecho gradient echo MRI sequence can be used to quantify fat and/or R_2^*[34–38]. To obtain accurate quantitative maps of fat and/or R_2^*, all factors in the signal model must be considered (see **section 2.5**)[39]. Conventional

MRI techniques typically employ Cartesian trajectories for fat or R_2* quantification[30–33,37,38,40–57]. Cartesian trajectories are limited by their sensitivity to respiratory motion-induced coherent aliasing artifacts, which degrade image quality and negatively impact fat and R_2* quantification accuracy. Therefore, Cartesian MRI acquisitions in the abdomen and pelvis are performed during a breath-hold. Because imaging parameters are selected to reduce scan times to fit within a breath-hold (typically 10 to 20 sec), spatial coverage, resolution and/or signal to noise ratio (SNR) may be reduced. Many populations such as children, infants, elderly patients, patients with chronic diseases, patients with disabilities, or pregnant women may have limited or no breath-hold ability, may have involuntary motion, and/or may not be able to comply with operator instructions[43,58,59].

Therefore, the purpose of this work was to develop and evaluate a new free-breathing (FB) 3D stack-of-radial (FB radial) MRI technique for fat or R_2* quantification at 3T in adults, children, infants, and pregnant women. This technique can eliminate the need for a breath-hold and allow for higher spatial resolutions and/or larger volumetric coverage. Since 3D stack-of-radial trajectories have greater sensitivities to system imperfections, including gradient delays, eddy current effects, and off-resonance effects[60], the main technical development of this work was a system calibration and correction approach to ensure quantification accuracy. A brief summary of the background and overview of these methods are discussed next.

1.1 Development and Evaluation of a Free-Breathing Stack-of-Radial MRI Fat Quantification Technique

Non-Cartesian trajectories have greater inherent robustness to motion[61,62]. Therefore, we proposed to develop a non-Cartesian free-breathing multiecho golden-angle ordered[63] 3D stack-of-radial radiofrequency-spoiled gradient echo sequence (FB radial) for hepatic fat

quantification. A potential challenge for utilizing non-Cartesian trajectories for quantitative MRI is the sensitivity to gradient delay errors and eddy current effects[60]. Therefore, a gradient delay calibration and correction approach was developed and evaluated in healthy subjects. The purpose of the study is to develop and evaluate a FB radial MRI technique with gradient calibration and correction for fat quantification in healthy adults. FB radial fat quantification accuracy was compared to both conventional Cartesian and reference SVS techniques.

Chapter 3 describes the development and evaluation of a FB radial technique for fat quantification in healthy adult subjects. This technique may be useful for many applications in the abdomen and pelvis and can be used to quantify hepatic fat for the diagnosis and monitoring of NAFLD.

1.2 Evaluation of a Free-Breathing Radial MRI Technique for Hepatic Fat Quantification in Children

Performing MRI experiments in children may pose additional challenges because they may have greater difficulty performing a breath-hold. Previous techniques have utilized conventional Cartesian trajectories[43,44,55,56]; however, children may have anxiety during the MRI exam and may have difficulty complying with operator instructions[43,64]. A FB radial technique may be a desirable alternative for hepatic fat quantification in this population. The feasibility, accuracy, and repeatability of FB radial MRI fat quantification were evaluated in a pediatric population consisting of healthy children and children with NAFLD. FB radial hepatic fat quantification accuracy was assessed with respect to BH Cartesian and BH SVS techniques. FB radial MRI image quality was compared to Cartesian MRI image quality.

Chapter 4 describes the work of evaluating the feasibility, image quality, accuracy, and repeatability of FB radial MRI technique in children at 3 T.

1.3 Free-Breathing Radial MRI Quantification of Body Composition and Hepatic Fat in Infants

Previous studies have used Cartesian MRI for fat quantification in infants[49–53]. However, infants are not capable of breath-holding. A technique that is robust to breathing motion is needed for performing MRI in infants. Body composition analysis and quantification of hepatic fat may provide insight into the origins of metabolic syndrome. Body composition analysis may be another useful application for the FB radial technique because it can provide larger volumetric coverage without the scan time limitations required for a breath-hold scan. Therefore, we proposed to evaluate the feasibility, repeatability and image quality of a FB radial MRI technique for body composition and hepatic fat quantification in infants. The image quality was compared to a conventional Cartesian MRI technique.

Chapter 5 describes the work on the evaluation of feasibility of a FB radial MRI technique for measuring body composition and feasibility, image quality and repeatability for hepatic fat quantification and in infants at 3 T.

1.4 Free-Breathing Radial MRI Quantification of Placental R_2*

In pregnant subjects, the uterus and placenta can undergo motion due to uterine contractions, maternal respiration, fetal motion, and other organ motion[65,66]. A breath-hold may avoid artifacts due to maternal respiration but involuntary motion due to fetal motion and uterine contractions may still occur. Furthermore, breath-holding limits the volumetric coverage achieved in the placenta. Previous studies investigating R_2* (R_2* = 1/T_2*) or T_2* mapping in the placenta have been performed using 2D breath-hold techniques using 1.5 T MRI[30–33]. Currently, there has been limited research involving R_2* or T_2* mapping in the placenta at 3 T or early gestation[67]. Therefore, we propose to investigate the feasibility and repeatability of the FB radial

MRI technique for R_2* quantification in the placenta during early gestation and report R_2* characteristics at 3T. This technique may enable the investigation of spatial R_2* variation throughout the placental volume and may improve the evaluation of IPD conditions.

Chapter 6 describes the work on the evaluation of feasibility and repeatability of a FB radial MRI technique for placenta R_2* quantification and report baseline placental R_2* findings during early gestation at 3 T.

2 THEORY

2.1 Applications for the Quantification of Fat and R_2*

MRI can quantify fat and R_2*[30–33,38,51,53–56,68,69] to provide important information for studying obesity[19,21,70,71], liver diseases[39,70,72,73], and diseases involving tissue hypoxia[30–33]. Obesity is associated with higher amounts of visceral fat and ectopic fat, such as in the liver[73–75], contributing to higher risk of insulin resistance, end-organ dysfunction, and cardiovascular disease[73–81]. For these reasons, accurate fat quantification techniques are needed to investigate ectopic fat and body composition, their effects on organ health and disease progression, and to assess the effectiveness of potential treatments. In this work, we will focus on the applications of MRI for hepatic fat quantification and body composition analysis. There are other potential applications in the pancreas, kidney, and heart[73–75,79,82–84]. For example, elevated pancreatic ectopic fat has shown correlations to β-cell dysfunction[79,85], and obese patients have shown kidney dysfunction[79] and cardiac steatosis causing cleft ventricular dysfunction[82]. These additional directions may be investigated in future work.

The placenta is an organ with an arterial-venous network that provides oxygen and

nutrients to the infant during gestation. IPD conditions are associated with abnormal placental vascular development, resulting in malperfusion and placental hypoxia[22–26] and contribute to higher rates of infant and maternal morbidity and mortality[23]. Hemoglobin is an iron-containing metalloprotein. When oxygen binds to hemoglobin (oxyhemoglobin), it becomes diamagnetic and does not affect the local magnetic field. On the other hand, the form of hemoglobin without oxygen, deoxyhemoglobin, is paramagnetic and causes local field inhomogeneities that affect nearby protons. Therefore, R_2* is higher (T_2* is lower) in hypoxic tissues and may be used to detect placental hypoxia[30–33]. Iron can also be deposited in other organs, including the liver and heart[86]. Tissue iron is also paramagnetic and causes a local field inhomogeneity for protons near iron[86]. Therefore, quantification of R_2* can also be used to detect liver or myocardial iron overload[86].

2.2 Multiecho MRI Sequences

Multiecho gradient echo sequences can be used to quantify hepatic fat[38,54–56,68], placental R_2*[30–33], and body composition[51,53,69]. There are two types of multiecho readout gradients that can acquire MRI signal at different echo times, unipolar (monolopar) and bipolar readouts. Unipolar readouts acquire MRI signals at each echo time using the same gradient polarity (Figure 2-1a), while bipolar readouts alternate the gradient polarity (Figure 2-1b). Compared to unipolar readouts, bipolar multiecho readout gradients are more sensitive to phase errors caused by gradient delays, eddy currents, and other factors[87–89]. However, bipolar gradients achieve higher SNR efficiency (number of TEs in each repetition time) for improved fitting to the signal model compared to unipolar gradients[87,88,90].

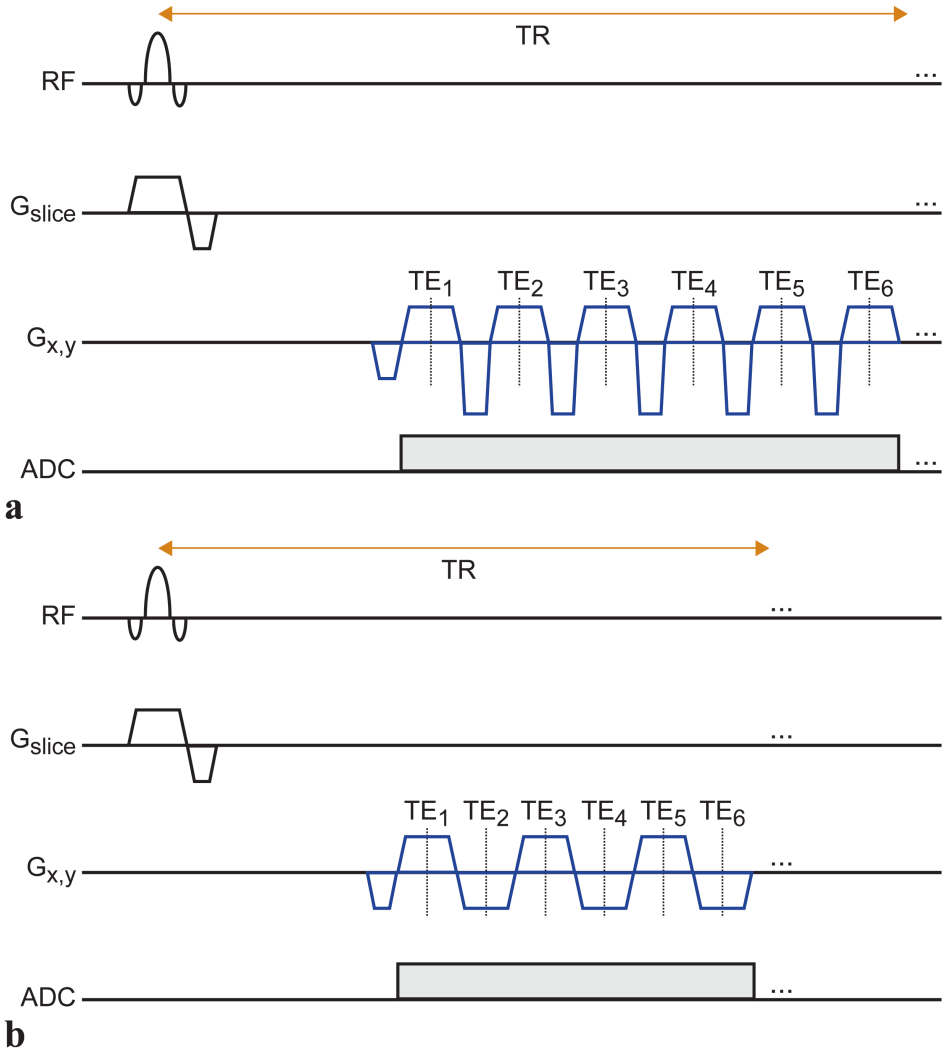

Figure 2-1 (a) Unipolar (monopolar) multiecho readout gradients. Each echo time (TE_n) is acquired using the same gradient polarity. (b) Bipolar multiecho readout gradients. Each TE_n is acquired using alternating gradient polarity. TR, repetition time; RF, radiofrequency; G_{slice}, slice select gradient; $G_{x,y}$, readout gradient; ADC, analog to digital converter.

2.3 R_2 and R_2* Relaxation

After RF excitation, there are two effects that cause decay of the transverse magnetization, spin-spin decay due to inherent tissue properties and additional dephasing caused by off-resonance effects[86]. These off-resonance effects may be due to inhohomoeneities of the main field (B_0), susceptibility differences, chemical shift, and gradients applied for spatial

encoding[86]. Spin echo sequences use 180° refocusing pulses to refocus the intra-voxel dephasing that occurs after the radiofrequency pulse to compensate for this dephasing caused by off-resonance effects[86]. Therefore, for spin echo sequences, the signal ($S_q(TE_n)$) decays at voxel q as a function of the echo time (TE_n) with time constant $R_{2,q}$

Equation 2-1

$$S_q(TE_n) = S_{0,q} \cdot e^{-R_{2,q}TE_n}$$

where $S_{0,q}$ is the MRI signal due to all protons and main field (B_0) inhomogeneity at an echo time of 0 and $R_{2,q}$ is the transverse relaxation rate for spin echo sequences (R_2) at voxel q. In gradient echo sequences there is no 180° refocusing pulse[86]. Thus, the signal decays exponentially as described by

Equation 2-2

$$S_q(TE_n) = S_{0,q} \cdot e^{-R^*_{2,q}TE_n}$$

where $R_{2,q}$* is the transverse relaxation rate for gradient echo sequences (R_2*) at voxel q. In gradient echo sequences, field inhomogeneities cause the signal to decay more rapidly[86]. Thus, R_2* is greater than R_2 and R_2* is related to R_2 by

Equation 2-3

$$R^*_{2,q} = R_{2,q} + \gamma \Delta B_{0,q}$$

where γ is the gyromagnetic ratio and $\Delta B_{0,q}$ is the main field inhomogeneity across the voxel q[86].

2.4 MRI Quantification of R_2*

R_2* quantification can be performed by using a multiecho sequence to obtain images from multiple different echo times (TE) and processing the data. Because the echo times (TE_n)

and signal at each echo time ($S_q(TE_n)$) are known, the R_2* (Equation 2-2) can be solved using non-linear least squares fitting, assuming $S_{0,q}$ and R_2* are free parameters[91]. In general, acquiring signals at more echo times improves fitting for R_2* as long as the signal has not decayed below the noise floor (Figure 2-2). To improve fitting for a small R_2* value, more echo times with longer echo spacing are beneficial. On the other hand, to improve fitting for a larger R_2*, more echo times with a short initial echo time and smaller echo spacing are desired. Another consideration is that R_2* estimation can be confounded by fat and noise bias, which will need to be considered for accurate R_2* quantification. Conventional magnitude fitting has Rician distribution noise which can lead to bias in R_2* estimation[92]. A potential method to mitigate noise bias for R_2* estimation is to truncate the signals below the noise floor (Figure 2-2)[92]. Another strategy is to perform complex fitting because complex data has zero mean Gaussian noise instead of Rician noise[92]. Another confounder for R_2* estimation is fat[92]. To improve the accuracy of R_2* estimation in fatty tissues, fat should be included in the signal model (see **section 2.5**)[92].

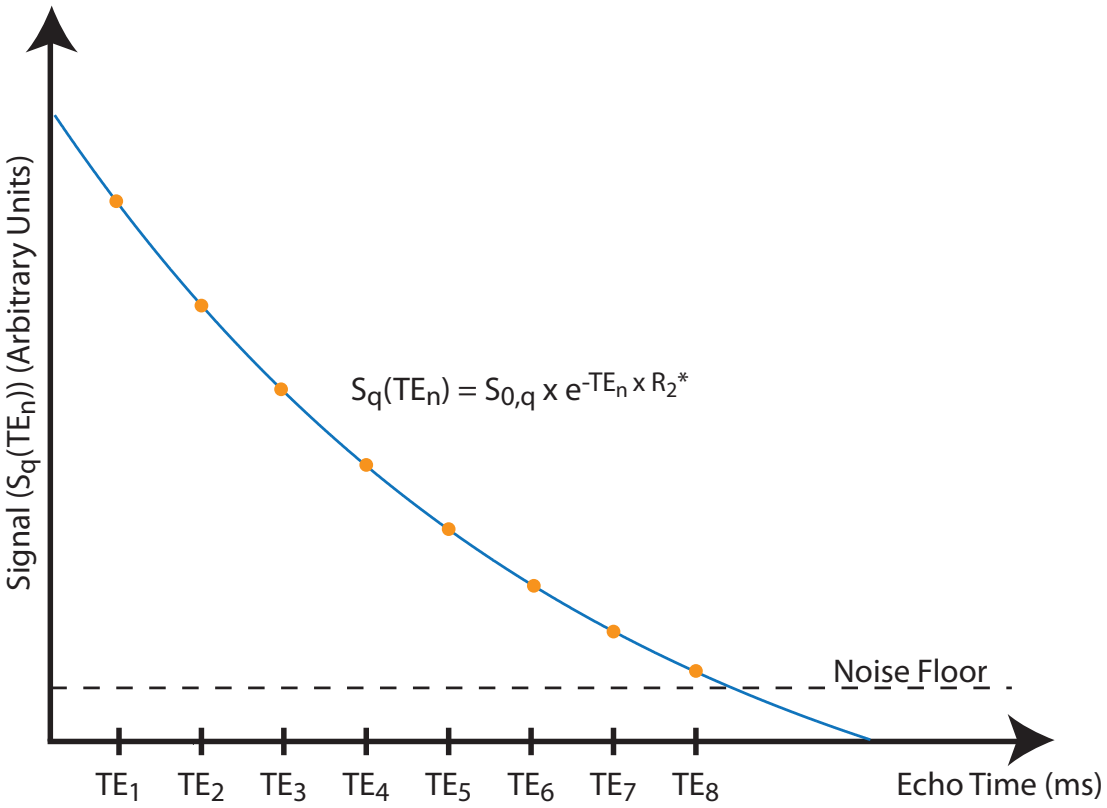

Figure 2-2 Signal ($S_q(TE_n)$) as a function of echo time (TE_n).

2.5 MRI Quantification of Fat and R_2*

In chemical shift encoded MRI (CSE-MRI), proton-density fat fraction (PDFF), a standardized MR-based biomarker for tissue fat quantification[70], is calculated by acquiring multiple echo time (TE) images and obtaining fat-only and water-only maps by fitting the data to a signal model[37,38]. Confounding factors such as T_1[41] and T_2^* decay[36,42,44,57], eddy current effects[87,88,93], gradient delay errors[87,88,93], noise[41], and complexities in the spectral model of fat[36,40,94,95] must be addressed to ensure the quantitative accuracy of PDFF[39].

Fat and water content can be quantified using CSE-MRI by fitting the acquired MR signal for each TE ($S_q(TE_n)$) to the gradient echo signal model[34–36]

Equation 2-4

$$S_q(TE_n) = \left(W_q + F_q \cdot \left(\sum_{j=1}^{M} a_j \cdot e^{i2\pi f_j TE_n} \right) \right) \cdot e^{-R^*_{2,q} TE_n} \cdot e^{i2\pi \varphi_q TE_n}$$

to solve for the signal contribution from water protons W_q, fat protons F_q, the effective transverse relaxation rate $R^*_{2,q}$ $(1/T^*_{2,q})$, and the frequency shift due to field inhomogeneity φ_q at each pixel location q. To account for multiple peaks in the fat spectrum, the signal model uses an a priori fat spectral model with relative peak amplitudes a_j and corresponding frequencies f_j for peaks j = 1,…,M where M is the number of peaks. In this work, a multi-peak fat model with M = 7 fixed frequencies and relative amplitudes[96] is employed. T_1 bias is reduced by using a low flip angle[41]. Gradient delay and eddy current effects are corrected using a gradient calibration and correction approach (see **section 3.2.2**). Hepatic fat quantification using this signal model in Equation 2-4 has been validated in many studies for healthy subjects and patients[38,54–56,68] including concomitant NAFLD and iron overload patients[57]. After correcting for confounding factors, PDFF (0-100%) is calculated using the fat-only (F_q) and water-only (W_q) signals in each pixel by

Equation 2-5

$$PDFF_q = \frac{F_q}{F_q + W_q} \times 100\%$$

2.6 Cartesian CSE-MRI for Fat and R_2* Quantification

Current CSE-MRI methods are mainly based on Cartesian sampling[30–33,37,38,40–57] (Figure 2-3a). A major limitation of Cartesian sampling for abdominal imaging is that it is susceptible to respiratory-motion-induced coherent aliasing artifacts that present along the phase encode direction. As a result, scans are performed during a single breath-hold and face challenges in

achieving full volumetric coverage, high spatial resolution, desirable echo times, high signal to noise ratio (SNR), and artifact-free images for hepatic fat quantification. Moreover, breath holding may not be possible for many patients and the accuracy of fat quantification becomes severely compromised.

Free-breathing MRI techniques using Cartesian trajectories have been developed and investigated to mitigate motion artifacts. These techniques involve respiratory gating using respiratory bellows[64,97] or navigators[64], and self-navigation[98–102]. Studies found accurate hepatic fat quantification using these investigational free-breathing techniques compared to breath-held techniques in populations who can perform a breath-hold[64,100]. However, respiratory gating or self-navigation can be technically challenging and may fail in cases when breathing is heavy or irregular[43,64]. Moreover, respiratory gating may have longer and more variable acquisition times[97]. Due to these limitations, these techniques may not be desirable in children. Children may have heavy or irregular breathing due to anxiety in the MRI scanner and may not comply with operator instructions[43,64]. Therefore, further investigation using respiratory gating and self-navigation is needed to determine the performance of these techniques in pediatric populations.

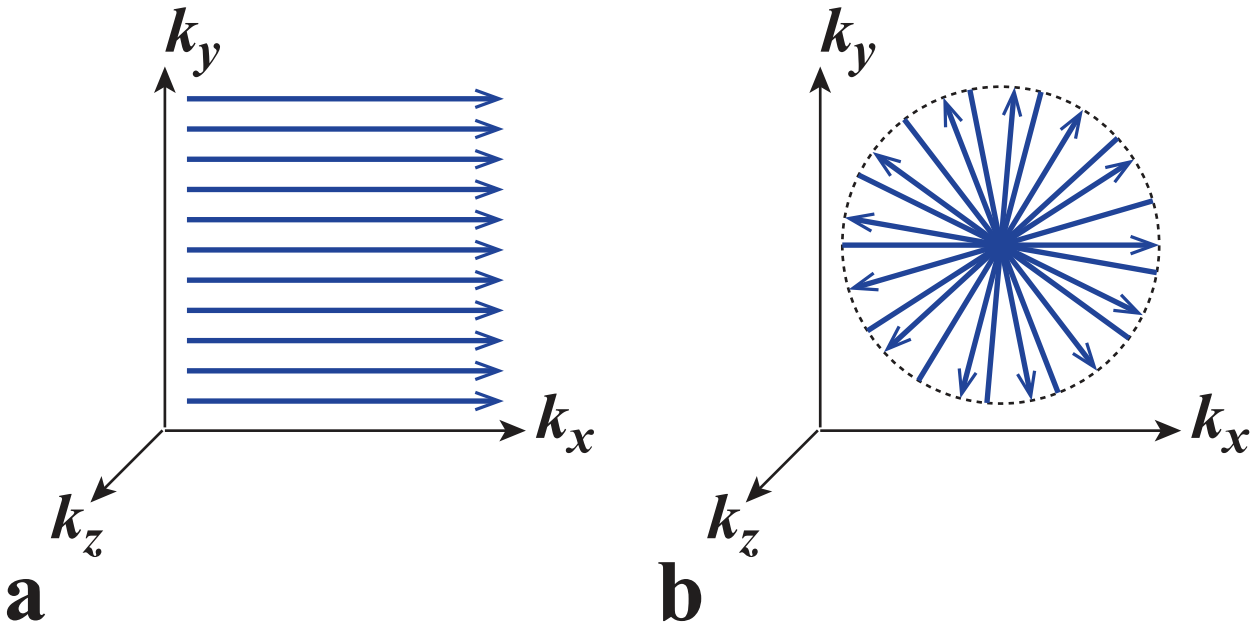

Figure 2-3 (a) Cartesian trajectory. (b) Radial trajectory.

2.7 Radial CSE-MRI for Fat and R_2* Quantification

A free-breathing MRI-based fat and R_2* quantification technique may improve the diagnosis and management of NAFLD, help investigate obesity, and may allow for the investigation of IPD. Non-Cartesian sampling trajectories have greater inherent robustness to motion and may provide a desirable alternative for performing fat quantification in the liver without the need for breath holding[61,62]. For 2D Cartesian trajectories, coherent-aliasing artifacts present along the phase encode direction in the presence of motion. For 2D radial trajectories (Figure 2-3b), the phase-encode direction changes throughout the acquisition. Thus, aliasing artifacts due to motion are distributed in-plane (k_x-k_y) and present as diffuse radial streaking artifacts. Therefore, the 2D stack-of-radial trajectory has considerably less obtrusive motion artifacts than 2D Cartesian sampling, even when data is continuously acquired during free-breathing and all of the data is used for reconstruction[62]. In 3D, both the 3D stack-of-radial and 3D Cartesian trajectories have Cartesian-encoding along the partition-encoded direction (k_z),

which may exhibit aliasing artifacts. During radial acquisitions, spokes or radial views can be acquired for each azimuthal angle along k_z prior to incrementing the azimuthal angle and acquiring the next set of spokes. If the time scale to acquire all k_z lines for a given azimuthal angle is very short, less than the time in which the motion occurs, the motion effects will primarily be distributed across the different azimuthal angles rather than along the k_z direction and manifest as in-plane radial streaking artifacts. For these reasons, 3D stack-of-radial trajectories have greater inherent robustness to motion compared to 3D Cartesian trajectories.

T_1-weighted 3D stack-of-radial sequences has been used for abdominal imaging[103–106], in organs such as the liver and pancreas and has shown improved image quality in pediatric patients who may have limited breath-holding capability or may have difficulty complying with operator instructions[103,104]. These studies investigated the image quality using a 3D stack-of-radial trajectory, but did not develop the technique to perform fat or R_2* quantification[103–106]. Other non-Cartesian trajectories such as PROPELLER[105], radial[99,106], spiral[107,108], and concentric rings[109] have been explored for fat-water separation but have not been evaluated for fat quantification, particularly in the liver. A major challenge to enable accurate fat quantification using non-Cartesian sampling trajectories is their sensitivity to gradient errors, which requires a correction (see **section 2.8**). The main technical development to realize a free-breathing 3D stack-of-radial fat quantification technique is to design an effective approach for calibrating and correcting these sources of error (see **section 3.2.2)**.

2.8 The Impact of Gradient Delays, Eddy Currents, and Off-Resonance on Cartesian and Radial Trajectories

Cartesian trajectories acquire readouts along the same direction for each repetition time (TR) (Figure 2-3a). Therefore, the effect of gradient delays on Cartesian trajectories is a bulk

shift of k-space data along the readout direction and a corresponding phase offset in image space (Φ_{del}) which will be accounted for when solving for the effective phase offset (Φ_{eff}) due to the field inhomogeneity (Φ_{off}) in Equations 2-7, 2-8, 2-9, and 2-10.

Equation 2-6

$$\phi_{off} = 2\pi\varphi_q TE_n$$

Equation 2-7

$$e^{i\phi_{eff}} = e^{i\phi_{off}} \cdot e^{i\phi_{del}}$$

Equation 2-8

$$\phi_{eff} = 2\pi\varphi_{eff,q} TE_n$$

Equation 2-9

$$S_q(TE_n) = \left(W_q + F_q \cdot \left(\sum_{j=1}^{M} a_j \cdot e^{i2\pi f_j TE_n} \right) \right) \cdot e^{-R^*_{2,q} TE_n} \cdot e^{i2\pi\varphi_{eff,q} TE_n}$$

Radial trajectories acquire readouts that pass through the center of k-space during each readout and the readout direction changes throughout the acquisition (Figure 2-3b) making them more sensitive to system imperfections such as gradient delay errors, eddy current effects, and off-resonance effects[60]. For radial trajectories, effects due to gradient delay errors, eddy current effects, and off-resonance should be addressed to achieve accurate fat and R_2* quantification. Gradient delays, eddy currents and off-resonance can cause misalignment of the center of k-space[60]. A simulation shows the effect of off-resonance effects on the point-spread function using radial trajectories with 0Hz off-resonance (Figure 2-4a) and off-resonance equal to 1-pixel k-space sample shift (Figure 2-4b). Off-resonance causes blurring of the radial point-spread function (Figure 2-4b). In addition, gradient delays can be different for the x (G_x) and y (G_y) directions[60]. Differences between gradients errors due to G_x and G_y result in different phase

errors for each acquired spoke[60]. Therefore, development and evaluation of a gradient calibration and correction method is necessary to ensure accurate PDFF and R_2* quantification using non-Cartesian trajectories.

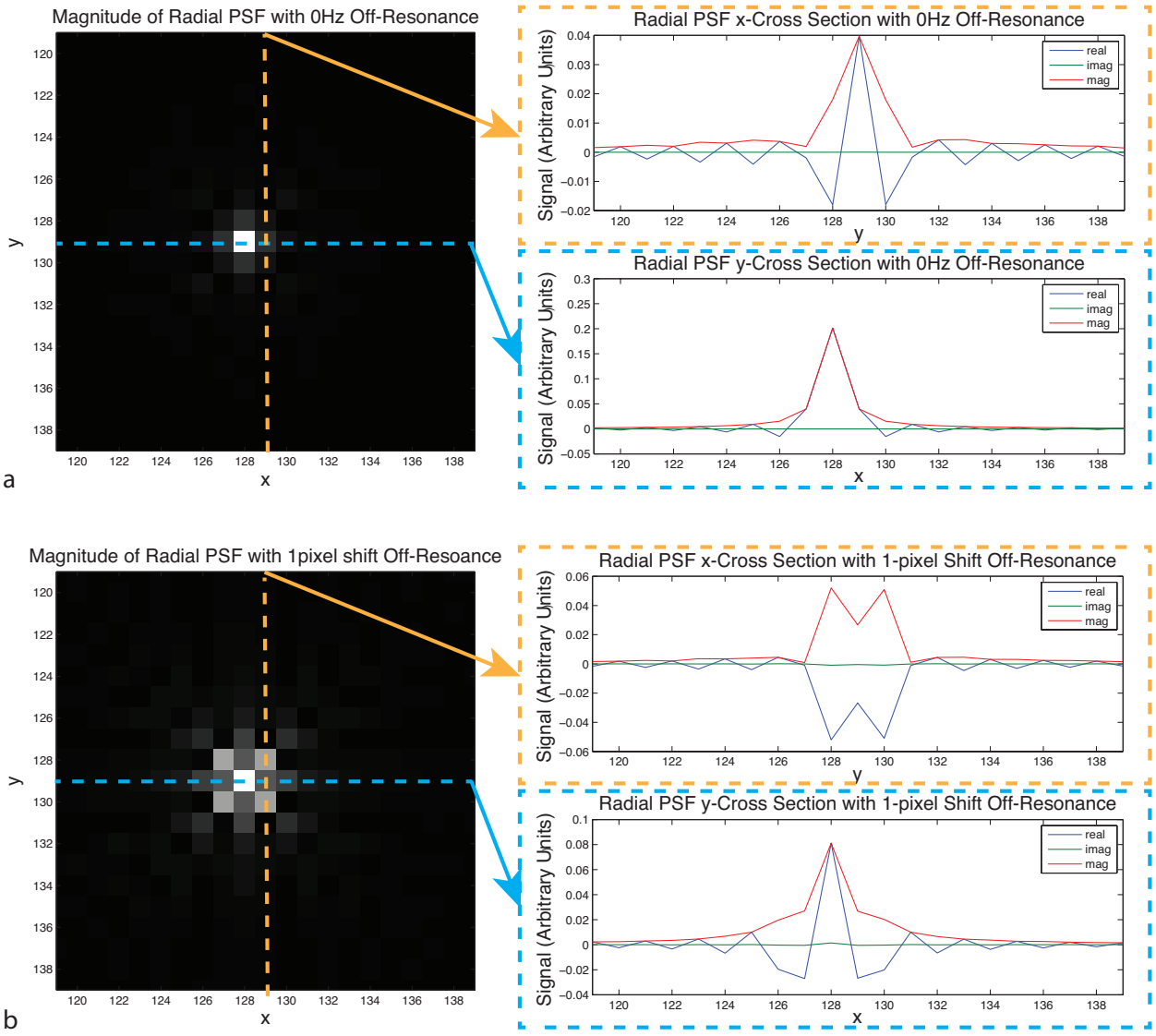

Figure 2-4 (a) Radial point-spread function with 0Hz off-resonance. (b) Radial point-spread function with off-resonance equal to 1-pixel shift. The dashed lines indicate the x and y cross sections of the point-spread function plotted as a function of position (x) and (y).

2.9 Evaluation of PDFF or R_2* Quantitative Accuracy

To assess quantification accuracy, simple linear regression analysis was performed to compare techniques (new and reference) by determining the equation for the linear relationship,

Pearson's correlation coefficient (r)[110], and Lin's concordance correlation coefficient (ρ_c)[111]. Pearson's correlations were calculated to evaluate the strength of the linear associations between the two techniques, whereas ρ_c's were calculated to estimate the degree of quantitative agreement (i.e. to estimate whether FB radial or BH techniques produce the exact same value for the range of hepatic PDFF). For example, when two techniques produce the exact same hepatic PDFF, ρ_c is 1. Lin's ρ_c was reported in this study because a high Pearson's correlation coefficient (r) does not necessarily imply identical measurements between FB radial and BH techniques. The equation for the concordance coefficient comparing FB radial to BH techniques is shown in Equation 2-10. Bland-Altman analysis[112] was performed to assess differences between two techniques by plotting the difference in PDFF between two techniques against the mean PDFF between two techniques. Specifically, the Bland-Altman analysis measures the mean difference (MD) or bias between two methods and the 95% limits of agreement (LoA), reported as the mean difference (MD) ± 1.96 times the standard deviation (SD) (i.e. ±LoA = MD ± 1.96 × SD).

Lin's concordance correlation coefficient (ρ_c)[111] for FB radial compared to BH (Cartesian and SVS) techniques:

Equation 2-10

$$\rho_c = \frac{2r\sigma_{BH}\sigma_{FB}}{\sigma_{BH}^2 + \sigma_{FB}^2 + (\mu_{BH} - \mu_{FB})^2}$$

μ_{BH} and μ_{FB} are the means and σ_{BH} and σ_{FB} are the standard deviations of the FB radial and BH techniques, respectively; r is the correlation coefficient between the FB and BH technique. All statistical analyses were performed in STATA software version 12.0 (Statacorp, College Station, TX) and MATLAB (MathWorks, Natwick, MA, United States). A P-value of < 0.05 was considered significant.

2.10 Evaluation of PDFF or R_2* Repeatability

To assess repeatability for each technique, the MD_{within} between repeated scans, within-subject standard deviation (SD_{within}) and coefficient of repeatability (CR) were reported[113,114]. The CR measures the variability for repeated measurements of the same technique (i.e. $CR = 1.96 \cdot \sqrt{2} \cdot SD_{within}$), therefore a smaller CR demonstrates smaller differences between repeated measurements[114]. All statistical analyses were performed in STATA software version 12.0 (Statacorp, College Station, TX, United States) and MATLAB (MathWorks, Natwick, MA, United States). A P-value of < 0.05 was considered significant.

3 DEVELOPMENT AND EVALUATION OF A FREE-BREATHING STACK-OF-RADIAL MRI FAT QUANTIFICATION TECHNIQUE

3.1 Introduction

Non-alcoholic fatty liver disease (NAFLD) is the most prevalent chronic liver disease worldwide, affecting up to 45% of the general population[115–117]. NAFLD is characterized by steatosis, or intracellular accumulation of triglycerides in the hepatocytes. NAFLD can progress to NASH, which affects about 2-5% of the general population and is a leading cause for liver cirrhosis, hepatocellular carcinoma and liver failure[115–118]. In addition, NAFLD is associated with cardiovascular disease and type 2 diabetes mellitus[115–119]. The increased prevalence of NAFLD, due to a rise in the rates of obesity and type 2 diabetes, is expected to make NAFLD a major

indication for liver transplantation[116,118]. The current gold standard for diagnosing and monitoring NAFLD or NASH is an invasive biopsy to characterize intracellular accumulation of triglycerides in the liver; however, biopsy has associated morbidity and suffers from spatial sampling bias[115–120]. Therefore, non-invasive techniques for hepatic fat quantification have been developed to improve the diagnosis and management of NAFLD.

Historically, MR spectroscopy (MRS) is considered the non-invasive reference standard for hepatic fat quantification[117]; however, MRS is also limited by spatial sampling bias. Non-invasive and spatially resolved fat quantification of the entire liver is possible with chemical-shift-encoded MRI (CSE-MRI) methods[68,121]. Current CSE-MRI methods are mainly based on Cartesian sampling[37,38,40–42,54–57] and are performed during a single breath-hold (see **section 2.6**). Compared to Cartesian sampling, 3D stack-of-radial sampling trajectories have greater inherent robustness to motion and may provide fat quantification in the liver without the need for breath holding (see **section 2.7**)[62].

In this work, a novel FB hepatic fat quantification technique using a bipolar multiecho non-Cartesian 3D stack-of-radial sequence with golden-angle ordering (FB radial) is developed and evaluated in a preliminary study. Importantly, a technique to characterize and correct the gradient errors in bipolar multiecho radial imaging is developed to ensure accurate PDFF quantification. Various degrees of radial undersampling are investigated to reduce scan time. The fat quantification performance of FB radial is compared to conventional breath-held Cartesian (BH Cartesian) MRI and reference standard breath-held single-voxel MR spectroscopy (BH SVS) approaches in a fat-water phantom and the pelvis and liver in a pilot cohort of healthy subjects.

3.2 Methods

3.2.1 Sequence Design: Multiecho Stack-of-Radial Sequence

A 3D stack-of-radial image acquisition provides inherent robustness to motion for liver imaging[61–63,98,122]. To enable free-breathing fat quantification, a bipolar multiecho RF-spoiled gradient echo prototype sequence using a golden-angle-ordered[63] 3D stack-of-radial trajectory was developed (Figure 3-1). Radial spokes with the same azimuthal angle were acquired for all k_z increments prior to azimuthal angle rotation. For azimuthal angle rotation, golden angle ordering (Figure 3-1b) was performed to support flexible reconstruction of an arbitrary number of radial views to balance spatiotemporal resolution, image SNR, and scan time[63]. This flexibility is highly favorable for data undersampling to accelerate FB radial imaging[123,124].

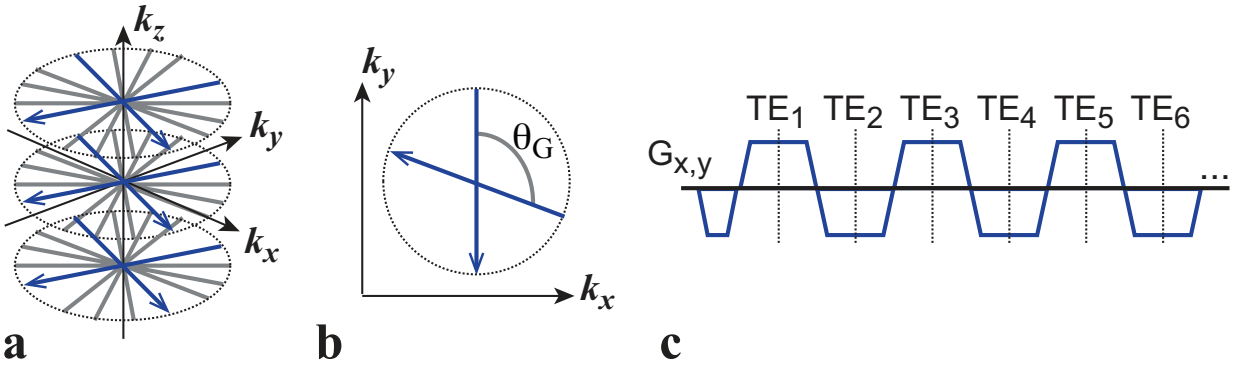

Figure 3-1 (a) 3D stack-of-radial trajectory. Radial readouts with the same azimuthal angle are acquired for all k_z increments before rotating the azimuthal angle. (b) Radial readouts are rotated continually by the golden angle (θ_G). (c) Six echoes are acquired every TR using a bipolar multiecho readout gradient.

Bipolar multiecho readout gradients (Figure 3-1c) were implemented for each spoke because they achieve higher SNR efficiency for improved fitting to the signal model compared to unipolar gradients[87,88,90]. However, both bipolar and radial imaging gradients are more sensitive to errors in the k-space trajectory and phase due to uncompensated gradient delays and eddy currents[60,87,88,125–127], which is a major source of error in PDFF quantification. Therefore, a main

requirement for developing a bipolar radial imaging technique for quantitative PDFF is to characterize and compensate for gradient errors (see **next subsection**).

3.2.2 Gradient Calibration and Correction

The main effect of gradient imperfections and deviations, including various delays and eddy current effects, can be modeled as an effective gradient delay and characterized by measuring the corresponding apparent shift of acquired data samples in k-space. Following image data acquisition, deviations in the bipolar and radial gradients were characterized[125] by collecting 80 additional calibration spokes for G_x and G_y in total (20 spokes for each azimuthal angle of 0 vs. π and $\pi/2$ vs. $3\pi/2$, respectively) (Fig. 3-2a). The calibration spokes of the same azimuthal angle were acquired for all k_z increments prior to rotating to the next azimuthal angle to induce similar gradient effects as the image data acquisition. The k-space signals for the azimuthal angles 0 vs. π and $\pi/2$ vs. $3\pi/2$ were compared with cross correlation to determine the apparent k-space sample shifts $\Delta\kappa_x$ and $\Delta\kappa_y$, due to effective gradient delays in G_x and G_y, respectively (Fig. 3-2b-c). The k-space signal was averaged over the 20 calibration spokes for each azimuthal angle, and 4-fold interpolation of the k-space signal was performed prior to cross correlation to achieve 0.25 k-space sample shift accuracy. Apparent k-space sample shifts were estimated for each spoke in the radial k-space trajectory ($\Delta\kappa_\theta$) according to

Equation 3-1

$$\Delta\kappa_\theta = \Delta\kappa_x(\cos\theta)^2 + \Delta\kappa_y(\sin\theta)^2$$

where θ is the azimuthal angle of the radial spoke and $\Delta\kappa_x$ and $\Delta\kappa_y$ are obtained from calibration[60,128]. The effective gradient delay and apparent k-space sample shift ($\Delta\kappa_x$, $\Delta\kappa_y$) potentially varies for each receiver channel and echo. Therefore, $\Delta\kappa_x$ and $\Delta\kappa_y$ for each channel

and echo were characterized independently. Previous methods[125] have used 15 spokes to calibrate each angle and averaged data from each channel, but since this proposed strategy for calibration is performed for each individual channel and echo, more calibration spokes are needed to maintain sufficient SNR. Correction of the effective gradient delays was performed using $\Delta\kappa_\theta$ to shift the radial k-space trajectory for each spoke of each channel and echo during 3D gridding reconstruction. The scan time for acquiring 80 additional spokes for calibration was $t_{scan} = 80 \cdot TR \cdot N_{k_z}$ (approximately 31 seconds for $N_{k_z} = 44$).

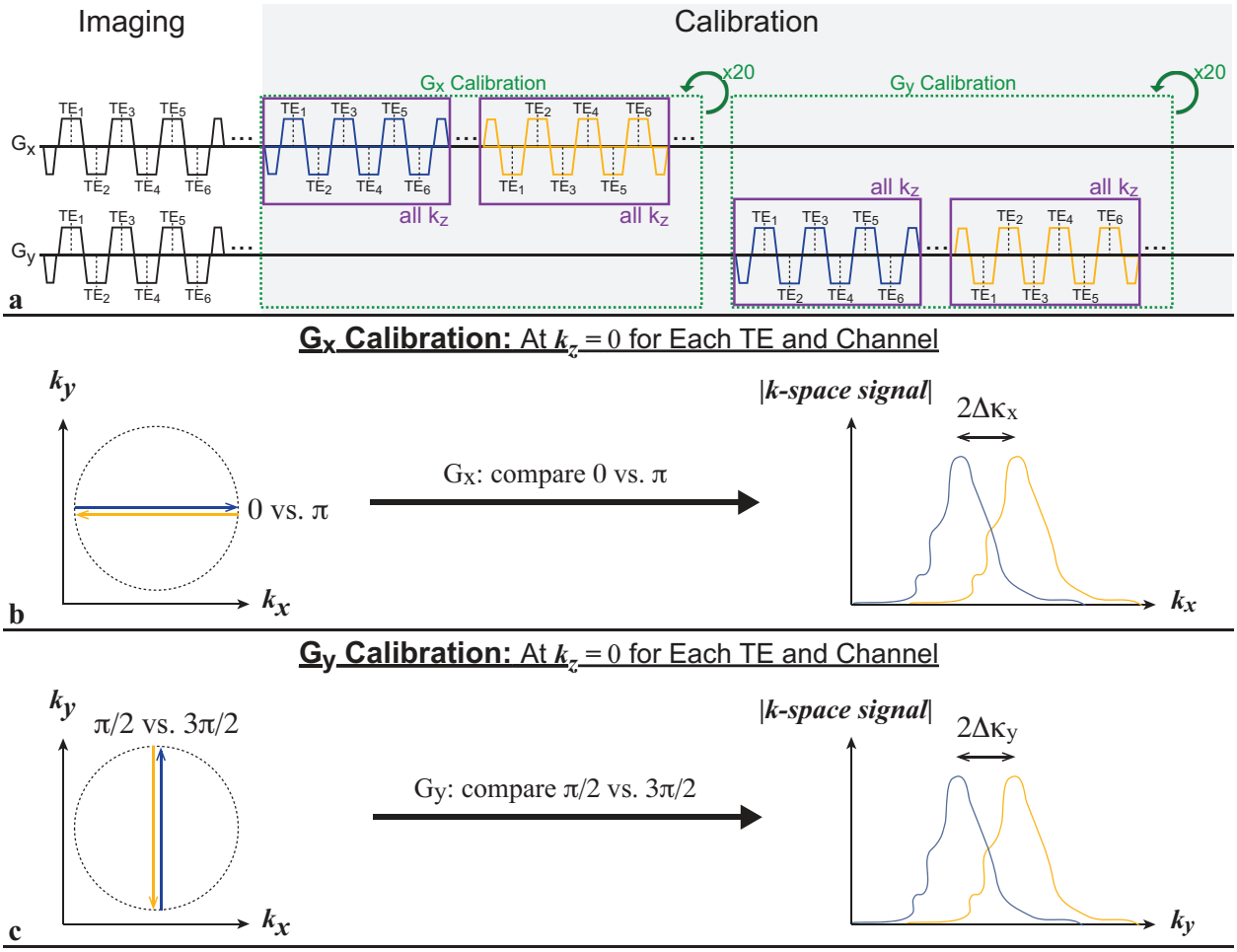

Figure 3-2 (a) Gradient calibration sequence design. As in the imaging module, a bipolar multiecho readout calibration module is repeated for all k_z increments to induce similar gradient effects. (b) The azimuthal angles 0 vs. π are compared to calibrate G_x and (c) $\pi/2$ vs. $3\pi/2$ are compared to calibrate G_y. The k-space sample shifts $\Delta\kappa_x$ and $\Delta\kappa_y$ are determined for both G_x and G_y, respectively, and used to correct the k-space trajectory for arbitrary azimuthal angles. TE, echo time.

3.2.3 Reconstruction and PDFF Calculation

The Cartesian and SVS sequences were reconstructed and PDFF maps were determined by the prototype scanner software. The Cartesian PDFF was calculated with mixed fitting using a Levenberg-Marquardt algorithm[56] with the signal model in Equation 2-4 with a 7-peak fat model with peaks at [0.97, 1.37, 1.66, 2.10, 2.32, 2.84, 5.38] ppm[96] and single effective R_2^* per voxel (see **section 2.5**). SVS PDFF results were calculated by peak integration from 3.6 to 5.8 ppm for water and 0 to 3.6 ppm for fat and T_2 correction was applied[129]. The SVS results were calibrated

by measuring PDFF in a test tube containing 100% fat. In this tube, SVS measured a PDFF of 92%; therefore all results were calibrated by dividing SVS PDFF by 0.92. This compensates for fat peaks that overlap with the water peak (not modeled in the prototype scanner SVS software), corresponding to about 8-9% of the total fat fraction[96,129,130].

Radial datasets were reconstructed and fat-water separation was performed offline with MATLAB R2013b (MathWorks, Natwick, MA, UNITED STATES). 3D gridding, a linear density compensation function, and adaptive coil combine[131] were used. Since golden angle ordering supports flexible selection of any contiguous subset of radial readouts for reconstruction, we emulated accelerated scans by retrospectively reconstructing the first 33% of readouts (R = 3), first 50% of readouts (R = 2), and 100% of readouts (R = 1, i.e. fully-sampled based on Nyquist criteria with the number of readouts = $N_{x,y} \times \pi/2$ where $N_{x,y}$ is the image size along x or y). Non-Cartesian parallel imaging reconstruction was not employed. Fat-water separation was performed using the signal model in Equation 2-4 with complex-fitting using a graph cut algorithm[34,35,132] with a 7-peak fat model[96] and a single effective R_2^* per voxel[36,42,57] (i.e., the same signal model as the prototype scanner-based Cartesian reconstruction) (see **section 2.5**). PDFF was calculated according to Equation 2-5 with magnitude discrimination to reduce noise bias[41] (see **section 2.5**). The offline radial reconstruction pipeline is shown in Figure 3-3.

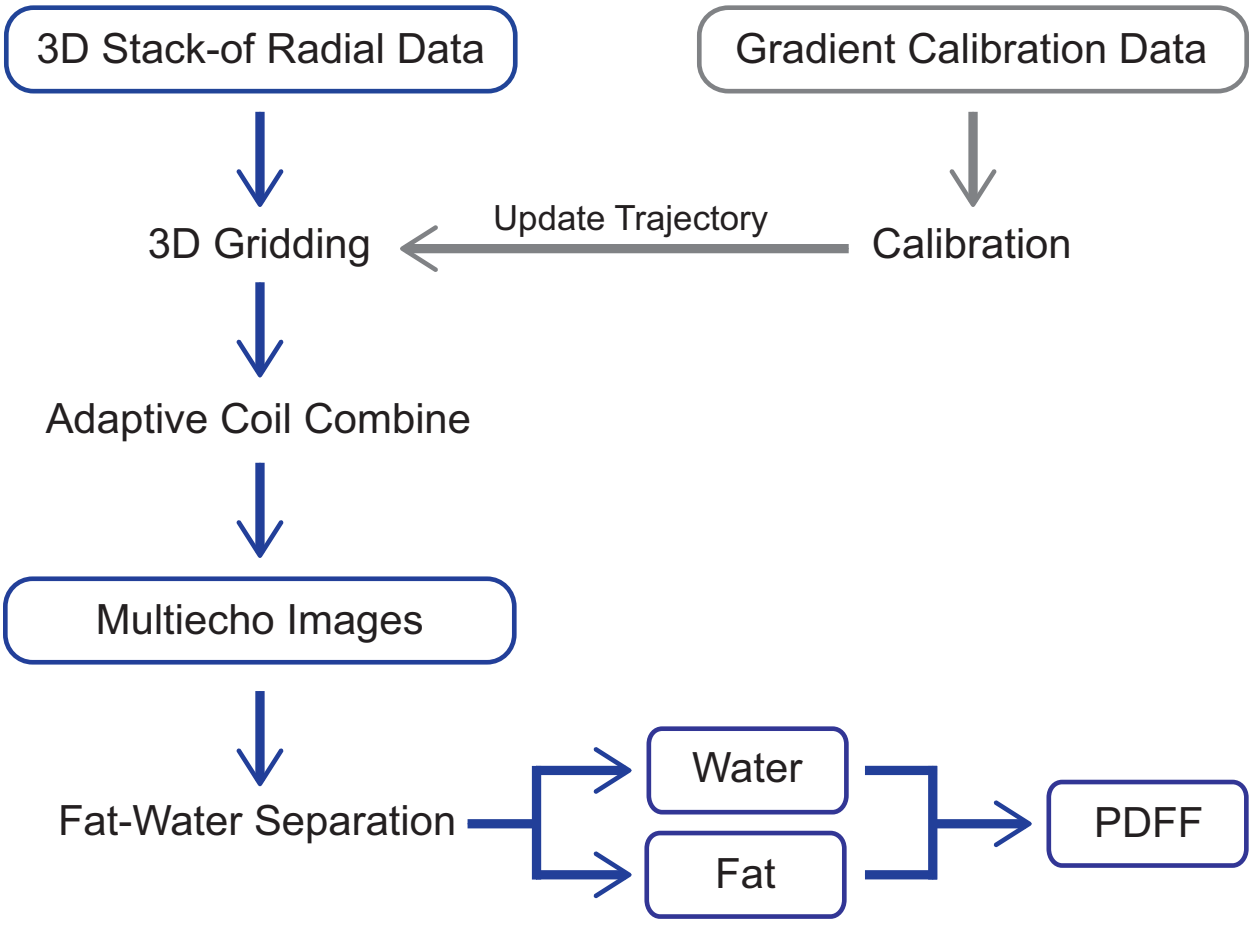

Figure 3-3 Reconstruction pipeline for the 3D stack-of-radial data.

3.2.4 MRI Experimental Design

This research study was approved by our local institutional review board. All experiments were performed on a 3 T MRI system (MAGNETOM Skyra, Siemens Healthcare GmbH, Erlangen, Germany) using a body array matrix and spine array coil. PDFF (%) was compared for the following techniques: FB bipolar multiecho 3D stack-of-radial prototype sequence with golden angle ordering (FB radial), BH bipolar multiecho 3D Cartesian prototype sequence (BH Cartesian)[56] and BH stimulated-echo acquisition mode (STEAM) single-voxel MR spectroscopy (SVS) prototype sequence (BH SVS)[129]. All human subjects gave written informed consent prior to scanning. For radial and Cartesian sequences, a low flip angle of 5°

was used to reduce T_1 bias[41], a large bandwidth was chosen to confine fat chemical shift blurring within a single pixel[133], and imaging parameters were matched as much as possible to enable a fair comparison (Table 3-1). Scan time is reported as minutes:seconds.

Table 3-1 Representative sequence parameters for in vivo liver experiments. A slice oversampling factor of 10% was used for all acquisitions.

Imaging Parameters	BH Cartesian	FB Radial	BH Radial
TE (ms)	1.23, 2.46, 3.69, 4.92, 6.15, 7.38		
ΔTE (ms)	1.23	1.23	1.23
TR (ms)	8.85	8.85	8.85
Matrix (Nx x Ny x Nz)	256 x 256 x 40	256 x 256 x 40	256 x 256 x 10
FOV (mm x mm x mm)	400 x 400 x 200	400 x 400 x 200	400 x 400 x 50
Slice Thickness (mm)	5	5	5
Radial Spokes	N/A	403 / 210 / 202 / 135	210
Flip Angle (degrees)	5	5	5
Bandwidth (Hz/pixel)	1150	1150	1150
Acceleration Factor (R)	4	1 / 1.92 / 2 / 3	1.92
Scan Time (min:sec)	0:27	3:08* / 1:53* / 1:50* / 1:24*	0:27*

***The radial gradient calibration scan time (31 sec for FB radial and 4.25 sec for BH radial) is included.**

In the phantom and in vivo pelvis experiments where there is no breath holding, both fully-sampled Cartesian (R = 1) and 4-fold accelerated Cartesian (R = 4) with CAIPIRINHA (2-fold acceleration along k_y, 2-fold acceleration along k_z)[134] were compared to the fully-sampled radial sequence (R = 1). In the liver, BH Cartesian R = 4 was compared to FB radial R = 1. Radial with scan acceleration (R = 2, 3) was emulated during reconstruction (see **subsection**) for all experiments and included in the comparisons. Imaging parameters for phantom and in vivo pelvis experiments are similar to those for in vivo liver experiments (Table 3-1).

3.2.5 Phantom Study

A PDFF phantom was constructed using nine 50mL test tubes each with different volumes of fat and water to obtain PDFF varying from 0% to 100%. The water solution was prepared with deionized water, 43mM of NaCl and 0.3mM of Gd-BOPTA (MultiHance) to reduce the T_1 to approximately 600ms[38]. Unrefined peanut oil was selected for fat due to similarities between the peanut oil fat spectrum and the subcutaneous fat spectrum[36].

The phantom was scanned using the SVS, Cartesian R = 1 and R = 4, and radial R = 1 sequences in the coronal plane at a specified position along the anterior-posterior (A-P) direction that resulted in a range of PDFF from 0% to 100% when eight coronal slices were combined to form a slab. The Design PDFF for each test tube in the coronal slab was obtained by first measuring the filling heights of fat and water on the axial and sagittal MRI images corresponding to the SVS ROIs in OsiriX software version 6.0 (Pixmeo Sarl, Bernex, Switzerland) to calculate the volume fat fraction (VFF). The VFF was then converted to Design PDFF by using the molecular weight (MW), density (d) and number of protons (λ) of peanut oil and water. The constants used were: MW_W = 18.015g/mol, MW_F = 283.275g/mol, d_W = 0.998g/mL, d_F = 0.910g/mL, $\lambda_W = 2$, and $\lambda_F = 33.926$[38,135].

SVS was performed in each test tube with voxel size 15mm x 15mm x 40mm, five echoes with TE = 12ms, 24ms, 36ms, 48ms, and 72ms, TR = 3000ms, mixing time = 10ms, vector size = 1024, and bandwidth = 1200Hz/pixel. The total acquisition time for the SVS scan was 0:15. 20 slices were imaged using radial R = 1, Cartesian R = 1, and Cartesian R = 4 with scan times of 2:00, 0:55, and 0:14, respectively.

3.2.6 In Vivo Pelvis Volunteer Study

In vivo pelvis scans of n = 5 (5 male) healthy subjects were performed to evaluate the agreement of PDFF between the Cartesian, radial, and the SVS scans. Scans in the pelvis have minimal inter-scan motion, which facilitates the comparison of fat quantification among these techniques. Pelvis scans were acquired in the axial plane using the radial R = 1, Cartesian R = 1 and Cartesian R = 4 techniques with scan times of 3:08, 1:40, and 0:27, respectively. SVS was performed in selected ROIs in the prostate, muscle, bone marrow and subcutaneous fat with a 10mm x 10mm x 15mm voxel size. The other parameters for the SVS scan were the same as in the phantom study.

To assess the accuracy of gradient calibration and effectiveness of gradient correction, two additional scans were performed in the pelvis of a healthy subject with the same scan parameters as shown in Table 3-1, except that the bulk gradient delay (default 0.65μs, corresponding to $\Delta\kappa_{x,d}, \Delta\kappa_{y,d}$) was prescribed to be 2.348μs and 4.047μs to induce additional apparent k-space sample shifts of 1- and 2-samples, respectively (i.e., $\Delta\kappa_{x,+1}, \Delta\kappa_{y,+1}$ and $\Delta\kappa_{x,+2}, \Delta\kappa_{y,+2}$).

3.2.7 In Vivo Liver Volunteer Study

In vivo liver scans of n = 11 (7 male) healthy subjects were acquired in the axial plane using the FB radial R = 1 sequence and BH Cartesian R = 4 sequences. The scan time for these acquisitions were 3:08 and 0:27, respectively. BH SVS was performed in six regions of interest (ROIs) with a voxel size of 10mm x 10mm x 15mm in the muscle, bone marrow, subcutaneous fat and the Couinaud-Bismuth segments II/IV, VII, and VIII in the liver[136,137]. These ROIs were selected to avoid major blood vessels and bile ducts. The other parameters for the SVS scan were

the same as in the phantom study.

To evaluate the performance of gradient calibration and correction, FB radial R = 1 images were reconstructed with and without gradient error correction in a subset of n = 5 (4 male) subjects. The resulting PDFF maps were randomized and scored by an abdominal radiologist blinded to the reconstruction technique on a quality scale of 1 to 4 (1: definite artifacts that would confound PDFF estimation in a large extent of the liver; 2: definite artifacts that would confound PDFF estimation in some regions of the liver; 3: mild artifacts that would not confound PDFF estimation; 4: no discernable artifacts and would not confound PDFF estimation.) In the remaining subjects, the gradient bulk delay in the sequence was adjusted to account for the calibrated effective gradient delay and prospectively reduce gradient errors.

To evaluate the robustness of FB radial PDFF in the presence of motion, an additional BH radial R = 1.92 scan was acquired in a subset of n = 5 (4 male) subjects and compared to a FB radial scan that was retrospectively undersampled to R = 1.92 (i.e., only reconstructing the first 53% of readouts).

3.2.8 Image and Statistical Analysis

All images and PDFF maps were converted to DICOM for viewing and analyzing in OsiriX. For quantitative evaluation, ROIs corresponding to the SVS ROIs were drawn on the Cartesian and radial PDFF maps. PDFF for all ROIs are reported as mean ± standard deviation (SD). Statistical analysis was performed in MATLAB and STATA software version 12.0.

For the phantom experiments, linear correlation and Bland-Altman analyses (see **section 2.9**) were performed between radial R = 1,2,3 and Cartesian R=1,4, SVS or Design PDFF. For the in vivo pelvis experiments, separate Bland-Altman analyses for low (< 5%) and high (> 80%)

PDFF regions were performed. For the in vivo liver experiments, linear correlation and Bland-Altman analysis were performed. For all statistical comparisons, r and ρ_c were tested for significance . $P < 0.05$ was considered significant.

3.3 Results

3.3.1 Gradient Calibration and Correction

Prior to gradient calibration, the radial PDFF maps in the pelvis (Figure 3-4a) show artifacts originating from gradient delays and eddy current effects. The $\Delta\kappa_{x,d}$, $\Delta\kappa_{y,d}$ (corresponding to the default bulk gradient delay) for different channels from the same echo ranged from 1- to 4.25-sample k-space shifts. This result supports the need to calibrate independently for each channel. Effects of the prescribed additional 1-sample and 2-sample k-space shifts were characterized by gradient calibration, obtaining $\Delta\kappa_{x,+1}, \Delta\kappa_{y,+1}$ and $\Delta\kappa_{x,+2}, \Delta\kappa_{y,+2}$, respectively. The incremental differences in apparent k-space sample shifts ($\delta\kappa_{x,+1}, \delta\kappa_{y,+1}, \delta\kappa_{x,+2}, \delta\kappa_{y,+2}$) were calculated by subtracting the calibrated apparent k-space shifts ($\Delta\kappa_{x,+1}, \Delta\kappa_{y,+1}, \Delta\kappa_{x,+2}, \Delta\kappa_{y,+2}$) from the default apparent k-space shifts ($\Delta\kappa_{x,d}$, $\Delta\kappa_{y,d}$). That is, $\delta\kappa_{x,+1} = \Delta\kappa_{x,+1} - \Delta\kappa_{x,d}$, $\delta\kappa_{x,+2} = \Delta\kappa_{x,+2} - \Delta\kappa_{x,d}$, $\delta\kappa_{y,+2} = \Delta\kappa_{y,+2} - \Delta\kappa_{y,d}$, $\delta\kappa_{y,+1} = \Delta\kappa_{y,+1} - \Delta\kappa_{y,d}$ average of $\delta\kappa_{x,+1}, \delta\kappa_{y,+1}, \delta\kappa_{x,+2}$ and $\delta\kappa_{y,+2}$ over all channels was calculated for each echo. Representative values of $\delta\kappa_{x,+2}$ for TE_1-TE_6 were: 1.95 ± 0.06, 2.03 ± 0.06, 1.95 ± 0.07, 2.03 ± 0.06, 1.95 ± 0.06, and 2.07 ± 0.08 samples, respectively. A two-tailed Student's t-test determined that the shifts averaged over all echoes were not statistically different from the prescribed additional 2-sample k-space shifts ($P > 0.5$ for $\delta\kappa_{x,+2}, \delta\kappa_{y,+2}$). The same result was obtained for 1-sample k-space shifts ($P > 0.9$ for $\delta\kappa_{x,+1}, \delta\kappa_{y,+1}$). The gradient correction strategy successfully removed the artifacts to produce accurate radial PDFF maps (Figure 3-4).

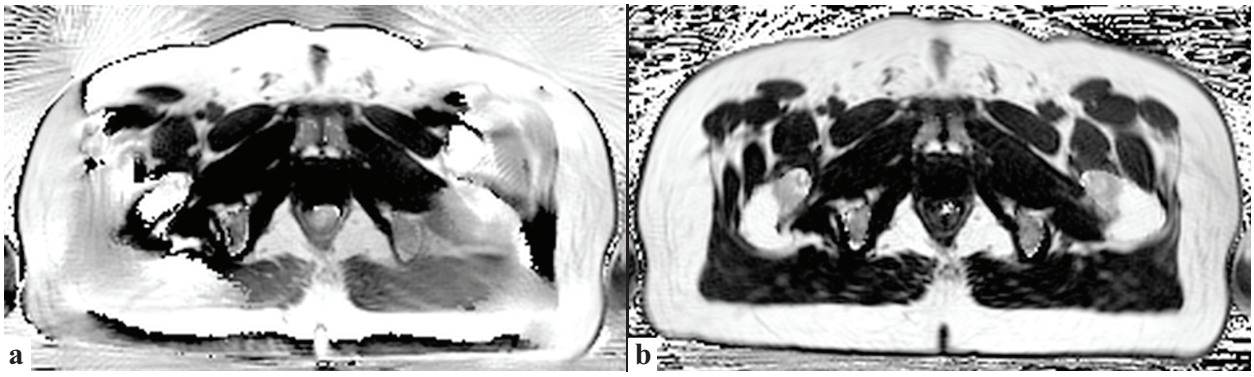

Figure 3-4 (a) An in vivo pelvis PDFF map with prescribed additional 2-sample k-space shifts ($\Delta\kappa_{x,+2}$, $\Delta\kappa_{y,+2}$) and no gradient error correction. (b) The corresponding in vivo pelvis PDFF map after gradient error correction.

The mean and SD of the average of all apparent k-space shifts across subjects, the range of the apparent k-space shifts among channels, and the range of the apparent k-space shifts among echoes were evaluated for the phantom, in vivo pelvis and in vivo liver data (Table 3-2). For the axial in vivo liver and pelvis scans, the logical G_x and G_y correspond to the physical G_x and G_y, while for the coronal phantom scan, the logical G_x and G_y correspond to the physical G_x and G_z. Similar mean apparent k-space sample shifts were observed for the phantom ($\Delta\kappa_x = 0.2$ samples, $\Delta\kappa_y = 0.2$ samples), in vivo pelvis ($\Delta\kappa_x = -0.17 \pm 0.04$ samples, $\Delta\kappa_y = -0.18 \pm 0.05$ samples), and in vivo liver experiments ($\Delta\kappa_x = -0.22 \pm 0.04$ samples, $\Delta\kappa_y = -0.21 \pm 0.04$ samples). Higher mean apparent k-space sample shift values were observed for the n = 5 FB radial scans acquired without prospective bulk gradient delay adjustment ($\Delta\kappa_x = 0.81 \pm 0.08$ samples, $\Delta\kappa_y = 0.86 \pm 0.09$ samples). In addition, channel and echo variation in $\Delta\kappa_x$ and $\Delta\kappa_y$ in the in vivo pelvis and liver experiments was observed with a mean range of shifts of 0.71-1.56 samples and 0.53-0.93 samples, respectively.

Table 3-2 The apparent k-space sample shifts for the phantom, in vivo pelvis, and in vivo liver experiments reported as mean ± standard deviation ($\mu \pm \sigma$) of the individual means determined from each subject. In (a) the Mean represents the mean (μ_{allx}, μ_{ally}) of $\Delta\kappa_x$ and $\Delta\kappa_y$ over all subjects, channels, and echoes. In (b) and (c) the Mean Range represents the mean of the range (μ_{Rx}, μ_{Ry}) of $\Delta\kappa_x$ and $\Delta\kappa_y$ (b) over all subjects and echoes as a function of channels (i.e. channel variability), and (c) over all subjects and channels as a function of echoes (i.e. echo variability). For the coronal phantom scans, logical G_x and G_y correspond to physical G_x and G_z, respectively. For the axial in vivo scans, logical G_x and G_y correspond to physical G_x and G_y, respectively.

	$\Delta\kappa_x$ (Logical G_x)	$\Delta\kappa_y$ (Logical G_y)
(a) All Channels and Echoes	**Mean ($\mu_{allx} \pm \sigma_{allx}$)**	**Mean ($\mu_{ally} \pm \sigma_{ally}$)**
Phantom	0.02	0.02
Pelvis	−0.17 ± 0.04	−0.18 ± 0.05
Liver	−0.22 ± 0.04	−0.21 ± 0.04
Liver*	0.81 ± 0.08	0.86 ± 0.09
(b) Channel Variability	**Mean Range ($\mu_{Rx} \pm \sigma_{Rx}$)**	**Mean Range ($\mu_{Ry} \pm \sigma_{Ry}$)**
Phantom	0.42	0.56
Pelvis	1.11 ± 0.39	1.14 ± 0.42
Liver	0.90 ± 0.16	0.71 ± 0.09
Liver*	1.56 ± 0.73	0.89 ± 0.43
(c) Echo Variability	**Mean Range ($\mu_{Rx} \pm \sigma_{Rx}$)**	**Mean Range ($\mu_{Ry} \pm \sigma_{Ry}$)**
Phantom	0.16	0.18
Pelvis	0.65 ± 0.13	0.63 ± 0.17
Liver	0.93 ± 0.21	0.77 ± 0.13
Liver*	0.88 ± 0.38	0.53 ± 0.21

***The sequence bulk gradient delay was not adjusted prospectively.**

3.3.2 Phantom Study

The Design PDFF was calculated as 0%, 11%, 13%, 16%, 32%, 50%, 55%, 80%, and 100%. (Figure 3-5a-b) CSE-MRI reconstructed PDFF maps using Cartesian and radial methods are presented in Figure 3-5c and 3-5d, respectively. The image quality and PDFF maps were very similar between Cartesian R = 1 and radial R = 1,2,3. Linear correlation and Bland-Altman plots for each comparison with radial R = 1 are shown in Figure 3-6. Full results from the linear correlation and Bland-Altman analysis are shown in Table 3-3 for radial R = 1,2,3.

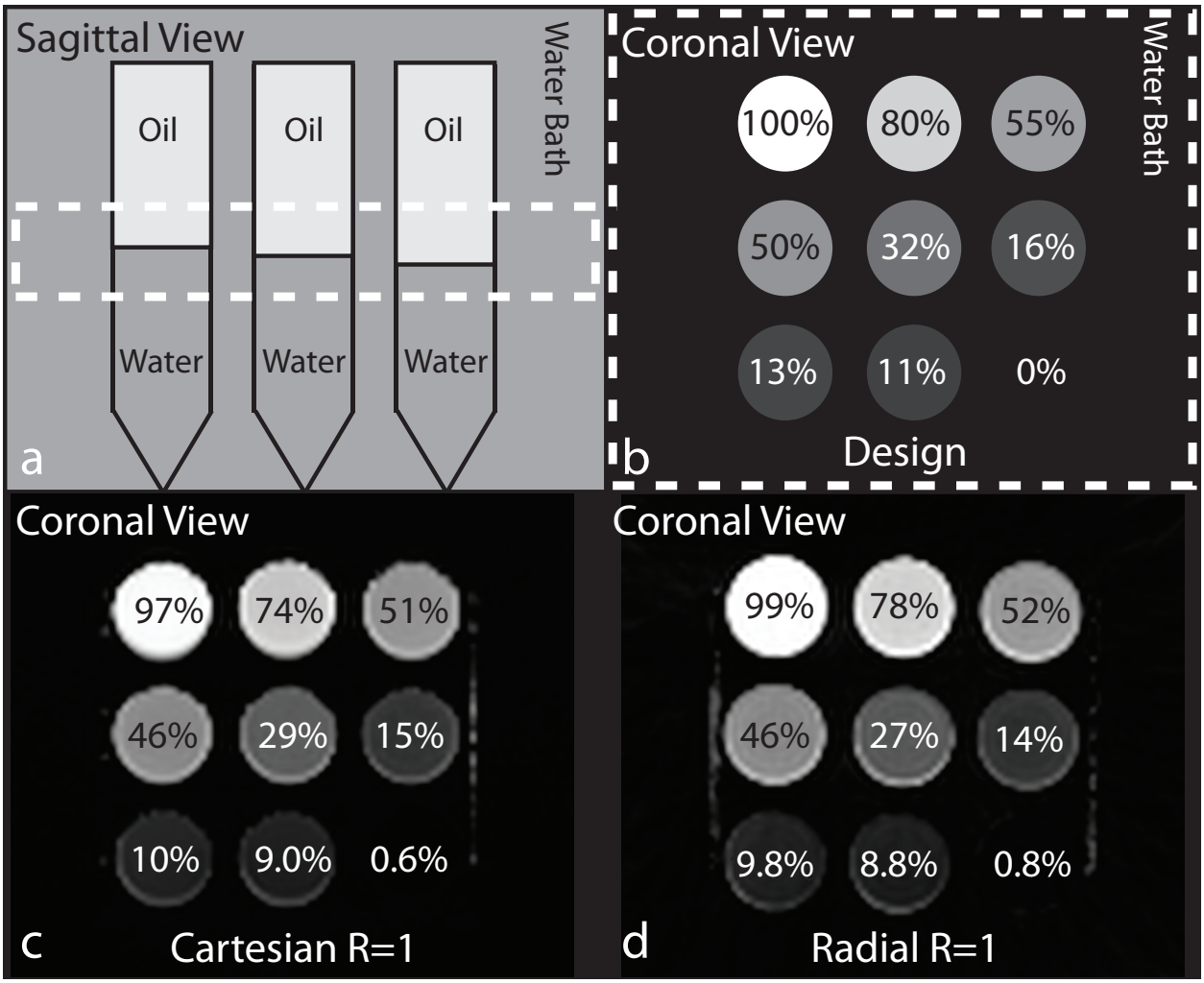

Figure 3-5 (a) Sagittal and (b) coronal views of the PDFF phantom design. A slab defined by the dotted lines (a) is combined to form the PDFF values shown in the coronal view (b). The PDFF maps for (c) Cartesian R = 1 and (d) radial R = 1.

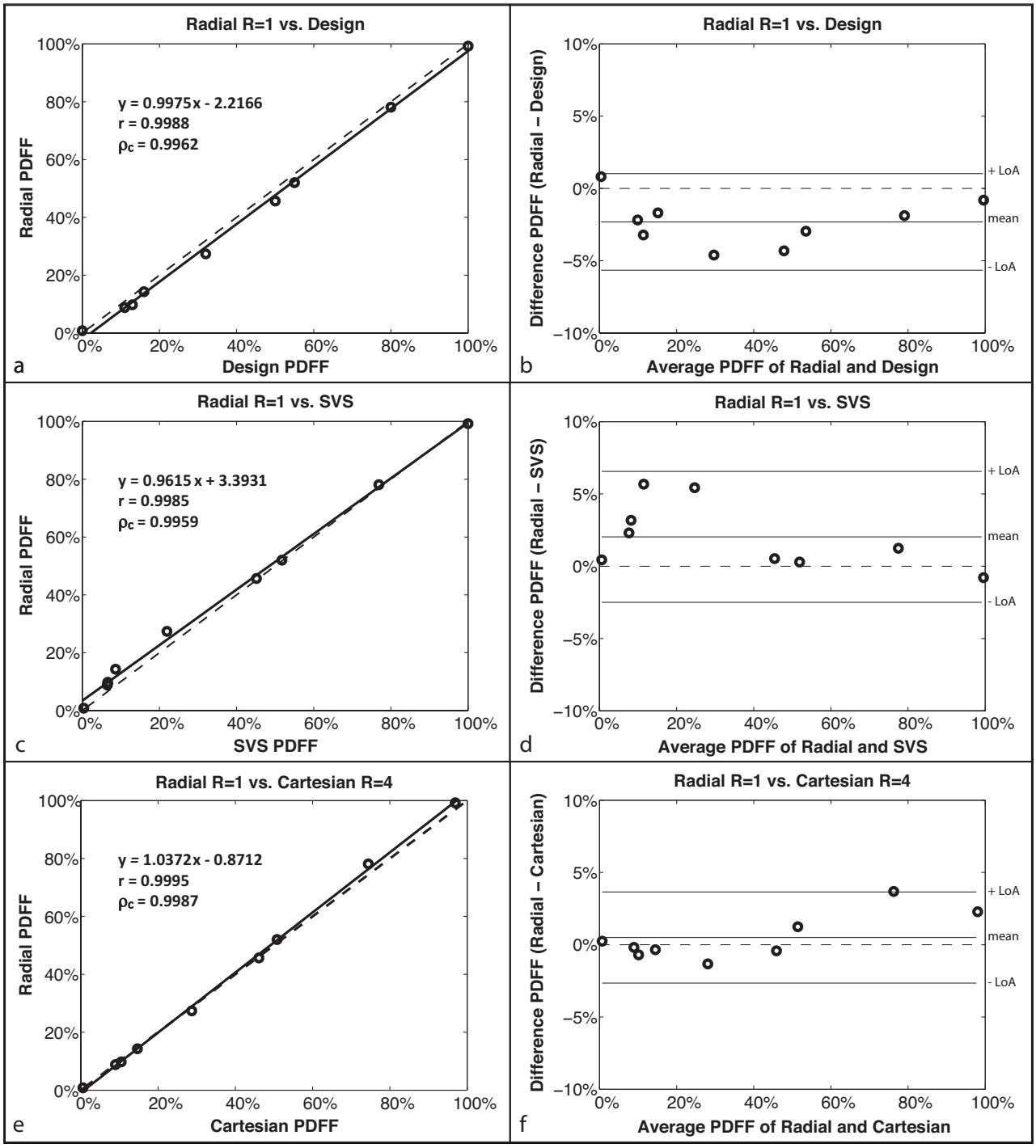

Figure 3-6 Phantom study (a,c,e) linear correlation plots and (b,d,f) Bland-Altman plots. For the comparison between (a-b) radial R = 1 and Design PDFF (described in the phantom design section of the methods) the MD = −2.32% and LoA = MD ± 3.34%, (c-d) radial R = 1 PDFF and SVS PDFF the MD = 2.03% and LoA = MD ± 4.53%, and (e-f) radial R = 1 PDFF and Cartesian R = 4 PDFF the MD = 0.5% and LoA = MD ± 3.15%. The correlation coefficients r and ρ_c are statistically significant in all cases (P < 0.001). The dashed lines represent y = x in the linear correlation plots and y = 0 in the Bland-Altman plots.

For the comparison between the radial R = 1 and Design PDFF (Figure 3-6a-b), the results showed a significant linear correlation with r = 0.9988 ($P < 0.001$) and $\rho_c = 0.9962$ ($P < 0.001$) for the mean PDFF. There was a mean difference of −2.32% between radial R = 1 and Design PDFF. The linear correlation and Bland-Altman analysis show a constant difference that does not depend on PDFF, which is likely due to un-modeled effects in the calculation of Design PDFF.

Linear correlation and Bland-Altman plots for the comparison between the proposed radial R = 1 and the non-invasive reference standard SVS (Figure 3-5c-d) also showed a significant linear correlation with r = 0.9985 ($P < 0.001$) and $\rho_c = 0.9959$ ($P < 0.001$) for mean PDFF. The mean difference between radial R = 1 and SVS PDFF was 2.03%. This is likely due to a combination of partial-volume effects and the difference in fat models used. The correction for the SVS PDFF may not be sufficient to address all of the differences in the fat models.

The comparison between radial R = 1 and the conventional Cartesian R = 1 showed a significant linear correlation for the mean PDFF. The correlation coefficients r and ρ_c were 0.9994 and 0.9987, respectively ($P < 0.001$). These results were similar to the comparison between radial R = 1 and Cartesian R = 4 (Figure 3-5e-f) which also had a significant linear correlation with r = 0.9995 ($P < 0.001$) and $\rho_c = 0.9987$ ($P < 0.001$). Comparing radial R = 1 versus Cartesian R = 1 and R = 4, the Bland-Altman plots show |mean differences| < 0.6% and LoA < mean difference ± 3.3%. Results from radial R = 2,3 are very similar to radial R = 1 for all comparisons (Table 3-3). These results show that a radial CSE-MRI technique can provide accurate PDFF results in a phantom.

Table 3-3 Bland-Altman and linear correlation analysis results for the phantom experiments. The mean difference (MD), limits of agreement (LoA), equation for the linear regression, Pearson's correlation coefficient (r) and Lin's concordance coefficient (ρ_c) for each comparison are reported. All coefficients r and ρ_c are significant with $P < 0.001$.

Phantom		LoA (MD ± 1.96SD)	Regression (y = mx + b)	r	ρ_c
Radial R = 1 vs.	Cartesian R = 4	0.5000% ± 3.1544%	y = 1.0372x − 0.8712	0.9995	0.9987
	Cartesian R = 1	0.4922% ± 3.2082%	y = 1.0345x − 0.7811	0.9994	0.9987
	SVS	2.0333% ± 4.5261%	y = 0.9615x + 3.3931	0.9985	0.9959
	Design PDFF	−2.3167% ± 3.3387%	y = 0.9975x − 2.2166	0.9988	0.9962
Radial R = 2 vs.	Cartesian R = 4	0.5944% ± 3.2117%	y = 1.0384x − 0.8216	0.9995	0.9986
	Cartesian R = 1	0.5867% ± 3.2886%	y = 1.0357x − 0.7306	0.9994	0.9986
	SVS	2.1278% ± 4.5119%	y = 0.9626x + 3.4488	0.9985	0.9957
	Design PDFF	−2.2222% ± 3.1630%	y = 0.9988x − 2.1735	0.9989	0.9965
Radial R = 3 vs.	Cartesian R = 4	0.5356% ± 3.0648%	y = 1.0307x − 0.5954	0.9994	0.9988
	Cartesian R = 1	0.5278% ± 3.1870%	y = 1.0280x − 0.5047	0.9992	0.9987
	SVS	2.0689% ± 4.8490%	y = 0.9555x + 3.6401	0.9984	0.9955
	Design PDFF	−2.2811% ± 3.3397%	y = 0.9914x − 1.9390	0.9988	0.9962

3.3.3 In Vivo Pelvis Volunteer Study

The study population comprised n = 5 (5 male) healthy subjects with age = 29.20 ± 2.86 years and body mass index (BMI) = 23.75 ± 3.51 kg/m^2. Representative CSE-MRI reconstructed PDFF maps using Cartesian R = 1, Cartesian R = 4, and radial R = 1 methods are presented in the axial and reformatted coronal orientations. (Figure 3-7) In all subjects, these three techniques produce very similar PDFF maps without fat-water swaps. Similar image quality was observed for radial R = 2,3 as was seen for radial R = 1. Bland-Altman plots were constructed separately for the low (<5%) and high (>80%) PDFF regions because of the absence of ROIs with intermediate PDFF values. Table 3-4 summarizes the Bland-Altman analysis for the low- and high-PDFF regions for radial R = 1,2,3 versus SVS, radial R = 1,2,3 versus Cartesian R = 1, and radial R = 1,2,3 versus Cartesian R = 4.

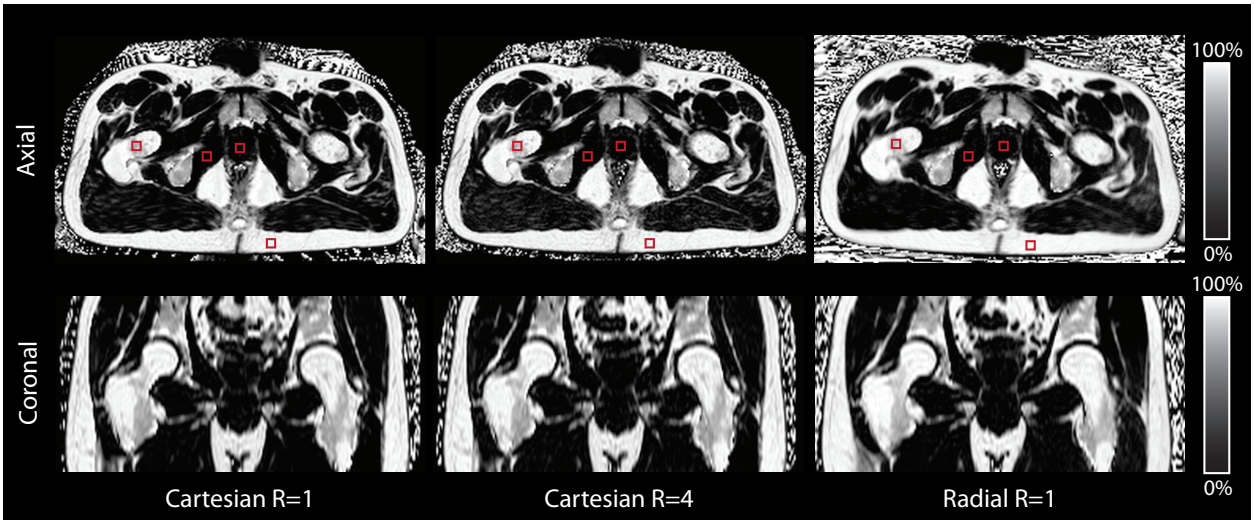

Figure 3-7 Representative in vivo pelvis PDFF maps for Cartesian R = 1, Cartesian R = 4 and radial R = 1 for a representative subject in axial and coronal orientations. The red squares indicate ROIs in the bone marrow, prostate, muscle, and subcutaneous fat for this subject.

Table 3-4 Bland-Altman analysis results for the in vivo pelvis experiments. The mean difference (MD) and limits of agreement (LoA) for each comparison are reported.

In Vivo Pelvis, Low PDFF (<5%)		LoA (MD ± 1.96SD)
Radial R = 1 vs.	**Cartesian R = 4**	−0.0770% ± 1.7543%
	Cartesian R = 1	0.2070% ± 1.2888%
	SVS	−0.7480% ± 1.6433%
Radial R = 2 vs.	**Cartesian R = 4**	0.8410% ± 2.6306%
	Cartesian R = 1	1.1250% ± 2.5350%
	SVS	0.1700% ± 3.0261%
Radial R = 3 vs.	**Cartesian R = 4**	0.8480% ± 2.9529%
	Cartesian R = 1	1.1320% ± 2.4274%
	SVS	0.1770% ± 3.1749%
In Vivo Pelvis, High PDFF (>80%)		**LoA (MD ± 1.96SD)**
Radial R = 1 vs.	**Cartesian R = 4**	3.6220% ± 3.0983%
	Cartesian R = 1	3.4210% ± 3.7526%
	SVS	4.4790% ± 5.0454%
Radial R = 2 vs.	**Cartesian R = 4**	3.5960% ± 3.5936%
	Cartesian R = 1	3.3950% ± 4.0773%
	SVS	4.4530% ± 5.1190%
Radial R = 3 vs.	**Cartesian R = 4**	3.7050% ± 4.1526%
	Cartesian R = 1	3.5040% ± 4.6885%
	SVS	4.5620% ± 5.5879%

For the low-PDFF regions: radial R = 1 versus Cartesian R = 1 and R = 4 had |mean differences| < 0.21% and LoA < MD ± 1.76%; radial R = 1 versus SVS had |mean differences| < 0.75% and LoA = MD ± 1.65%. For the high-PDFF regions: radial R = 1 versus Cartesian R = 1 and R = 4 had |mean differences| < 3.7% and LoA < MD ± 3.8%; radial R = 1 versus SVS had

|mean differences| < 4.5% and LoA = MD ± 5.1%. These results illustrate agreement in mean PDFF for in vivo pelvis data between radial R = 1, the conventional Cartesian R = 4 and radial R = 1, and the reference standard SVS. Similar results were observed for radial R = 2,3 as was seen for R = 1.

3.3.4 In Vivo Liver Volunteer Study

The study population comprised n = 11 (7 male) healthy subjects with age = 26.09 ± 2.84 years and BMI = 23.17 ± 4.21 kg/m^2. Representative axial, reformatted coronal and reformatted sagittal PDFF maps from FB radial R = 1,2,3 and BH Cartesian R = 4 are shown in Figure 3-8. The PDFF maps from FB radial R = 1,2,3 and BH Cartesian R = 4 are very similar, but have slight differences in liver position due to breath holding. Radial readouts of the same angle were acquired for all k_z encoding steps (along the superior-inferior direction for axial scans) prior to azimuthal angle rotation. Since the time to acquire all readouts of the same angle is small (≈389ms), there is limited motion along the Cartesian encoding direction k_z prior to each angle rotation. The effects of the motion are therefore distributed predominantly in the in-plane k_x-k_y directions and manifest as radial incoherent motion aliasing artifacts, thereby minimizing Cartesian-encoded through-plane coherent motion artifacts. This is confirmed by inspecting reformatted sagittal and coronal images of the 3D axial dataset (example in Figure 3-8). Mean PDFF results from corresponding ROIs using FB radial R = 1, BH Cartesian R = 4 and BH SVS are compared in linear correlation and Bland-Altman analysis (Figure 3-9). Full Bland-Altman and linear correlation results for all comparisons in the liver experiments are shown in Table 3-5.

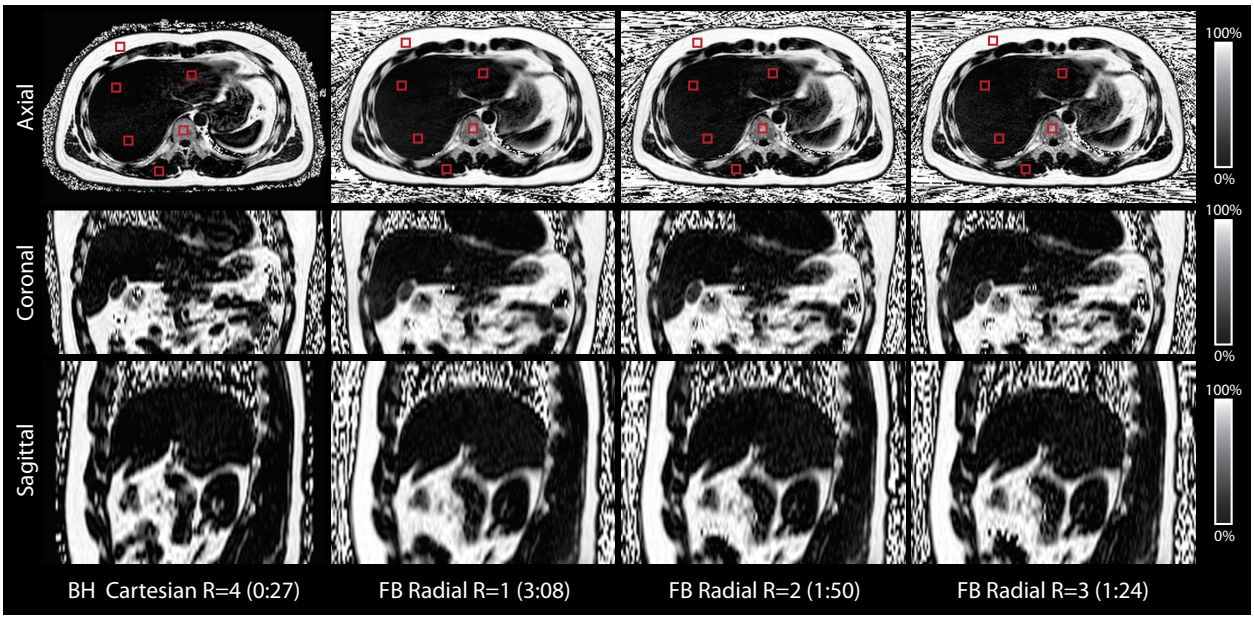

Figure 3-8 Representative in vivo pelvis PDFF maps for Cartesian R = 1, Cartesian R = 4 and radial R = 1 for a representative subject in axial and coronal orientations. The red squares indicate ROIs in the bone marrow, prostate, muscle, and subcutaneous fat for this subject.

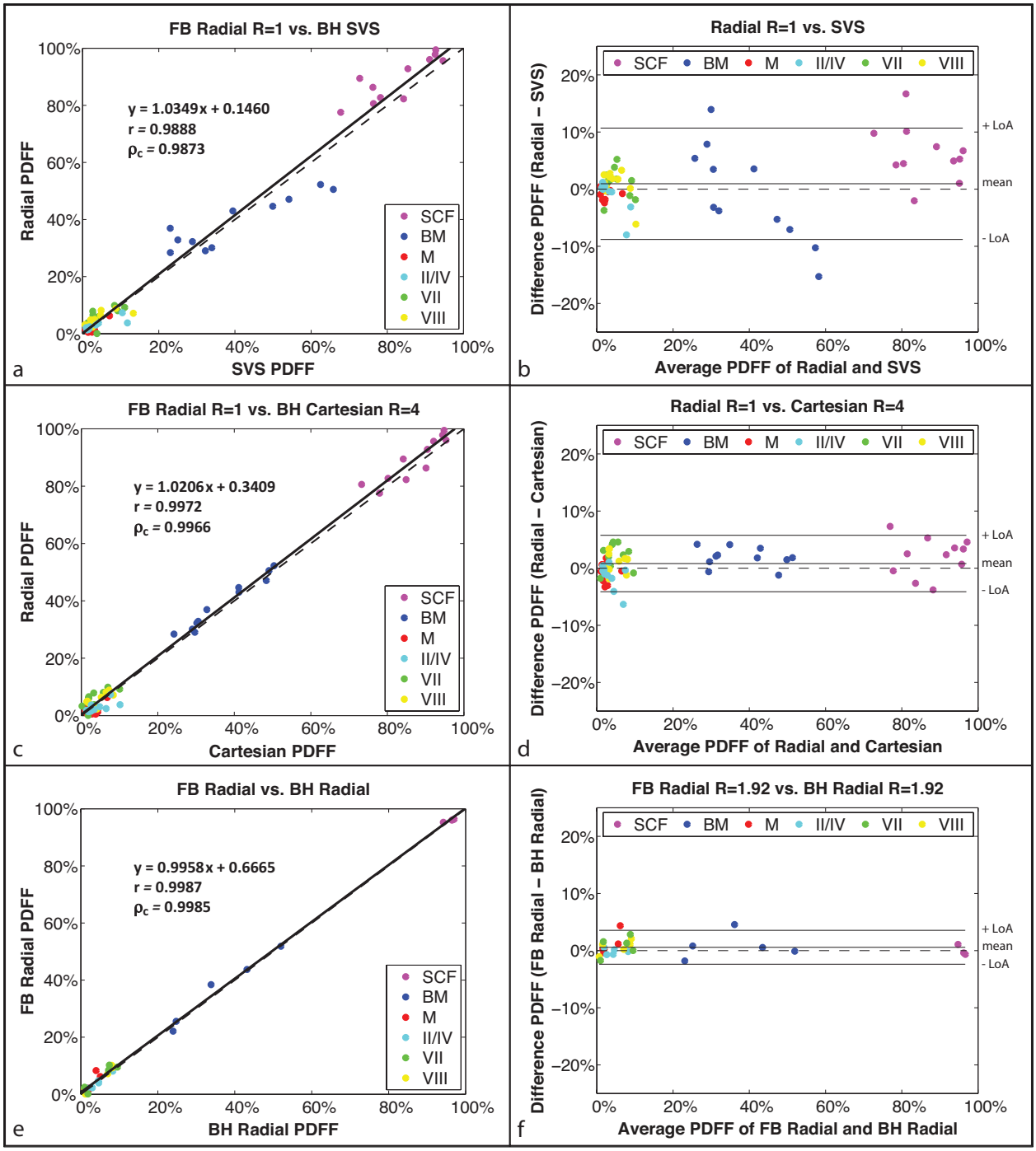

Figure 3-9 In vivo liver study (a,c,e) linear correlation plots and (b,d,f) Bland-Altman plots for PDFF of ROIs in the subcutaneous fat (SCF), bone marrow (BM), muscle (M), and Couinaud-Bismuth segments II/IV, VII, and VIII. The comparison of (a-b) FB radial R = 1 versus SVS had mean difference (MD) = 0.95% and LoA = MD ± 9.74%, (c-d) FB radial R = 1 versus Cartesian R = 4 had MD = 0.82% and LoA = MD ± 4.9%, and (e-f) FB radial R = 1.92 versus BH radial R = 1.92 had MD = 0.58% and LoA = MD ± 2.97%. The correlation coefficients r and ρ_c were significant in all cases with P < 0.001. The dashed lines represent y = x in the linear correlation plots and y = 0 in the Bland-Altman plots.

Table 3-5 Bland-Altman and linear correlation analysis results for the in vivo liver experiments. The mean difference (MD), limits of agreement (LoA), equation for the linear regression with slope (m) and intercept (b), Pearson's correlation coefficient (r) and Lin's concordance coefficient (ρ_c) for each comparison are reported. All coefficients r and ρ_c are significant with P < 0.001.

In Vivo Liver		LoA (MD ± 1.96SD)	Regression (y = mx + b)	r	ρ_c
FB Radial R = 1 vs.	**BH Cartesian R = 4**	0.8182% ± 4.9324%	y = 1.0206x + 0.3409	0.9972	0.9966
	BH SVS	0.9474% ± 9.7406%	y = 1.0349x + 0.1460	0.9888	0.9873
FB Radial R = 2 vs.	**BH Cartesian R = 4**	0.8364% ± 5.3767%	y = 1.0211x + 0.3487	0.9966	0.9960
	BH SVS	0.9656% ± 9.7243%	y = 1.0360x + 0.1382	0.9889	0.9873
FB Radial R = 3 vs.	**BH Cartesian R = 4**	0.6224% ± 5.6548%	y = 1.0190x + 0.1841	0.9962	0.9958
	BH SVS	0.7517% ± 10.5172%	y = 1.0320x + 0.0158	0.9867	0.9854
FB Radial R = 1.92 vs.	**BH Radial R = 1.92**	0.5839% ± 2.9721%	y = 0.9958x + 0.6665	0.9987	0.9985

The results show a significant linear correlation with r = 0.9888 and ρ_c = 0.9873 between FB radial R = 1 and BH SVS (Figure 3-8a) and with r = 0.9972 and ρ_c = 0.9966 between FB radial R = 1 and BH Cartesian R = 4 (Figure 3-8c). The Bland-Altman plots show a |mean difference| < 0.9% for FB radial R = 1,2,3 versus BH Cartesian R = 4 and a |mean difference| < 1% for FB radial R = 1,2,3 versus BH SVS. These results demonstrate that even with motion, accurate fat quantification can be achieved in the liver and abdomen using a FB radial (R = 1,2,3) technique.

In the subset of n = 5 (4 male) healthy subjects with and without gradient error correction

in FB radial reconstruction, PDFF maps with gradient error correction successfully suppressed artifacts and demonstrated substantially higher quality (score = 4 ± 0) than without gradient error correction (score = 1.6 ± 0.55). Representative results are shown in Figure 3-10 In vivo liver FB radial PDFF maps reconstructed with and without gradient error calibration and correction. Apparent k-space sample shifts were on average 0.8 samples. Gradient correction substantially improves the quality of the PDFF maps.

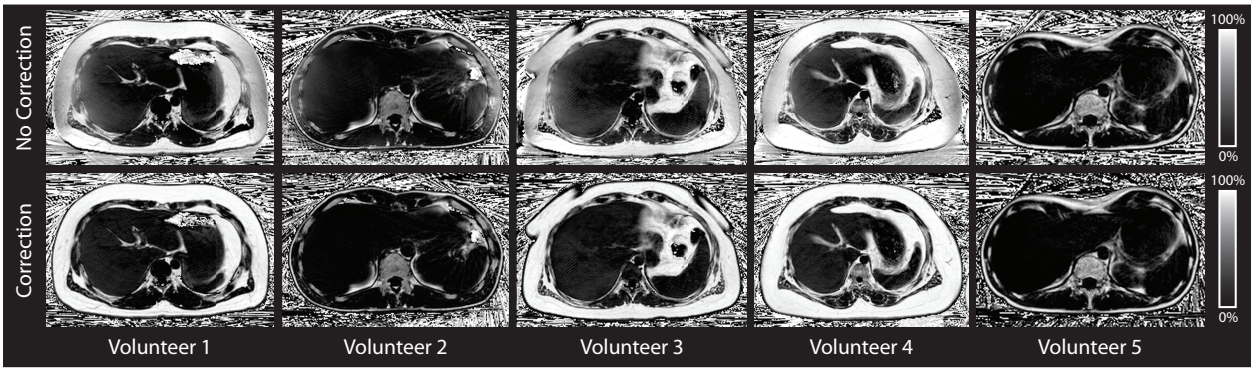

Figure 3-10 In vivo liver FB radial PDFF maps reconstructed with and without gradient error calibration and correction. Apparent k-space sample shifts were on average 0.8 samples. Gradient correction substantially improves the quality of the PDFF maps.

In the subset of n = 5 (4 male) healthy subjects with both FB radial and BH radial acquisitions, the PDFF maps showed similar quality (Figure 3-11). The linear correlation analysis between the FB radial PDFF and BH radial PDFF showed a significant linear correlation with r = 0.9987, ρ_c = 0.9985, mean difference = 0.58% and LoA = MD ± 2.97% (Figure 3-9e-f).

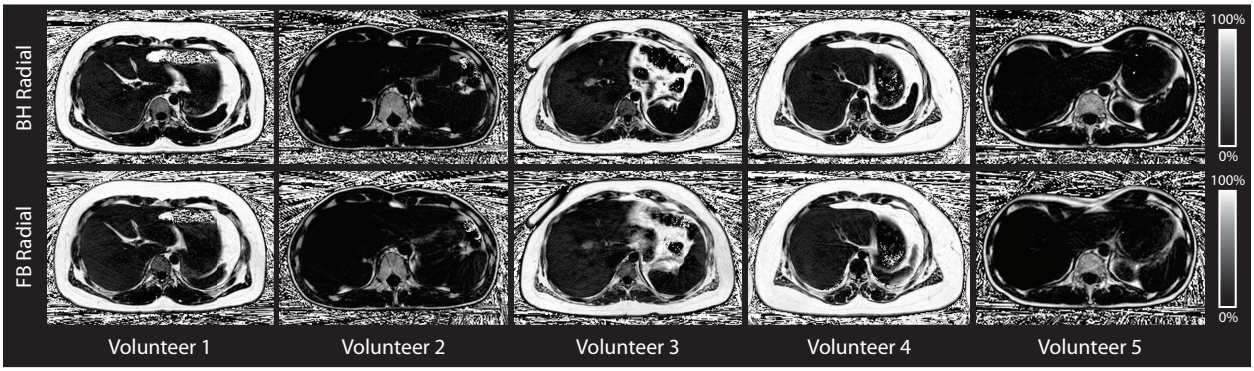

Figure 3-11 In vivo liver FB radial R = 1.92 and BH radial R = 1.92 PDFF maps. The PDFF maps are very similar with only slight differences in liver positioning due to breath holding.

3.4 Discussion

Our results demonstrate that accurate fat quantification can be performed during free-breathing for the entire 3D liver volume using a bipolar multiecho 3D stack-of-radial technique within a fast 1-2 minute scan. PDFF calculated from FB radial scans, with and without acceleration (R = 1,2,3), had significant linear correlations and < 1% mean differences compared to both conventional BH Cartesian and reference standard BH SVS techniques in the liver and abdomen. BH Cartesian CSE-MRI methods have been previously established for fat quantification, and this is the first study to propose a FB radial technique and evaluate its accuracy with respect to established BH techniques.

In the phantom experiments where there was no motion and the medium was relatively homogeneous, the mean apparent k-space sample shifts due to logical G_x and logical G_y were small (0.02); however, there were still differences among channels (range of k-space sample shifts of 0.42 and 0.56 samples for gradient G_x and G_y, respectively) and among echoes (range of k-space sample shifts of 0.16 and 0.18 samples for gradient G_x and G_y, respectively) (Table 3-2). In the in vivo liver experiments where there was motion and inhomogeneous tissue types, gradient calibration showed larger differences among channels (range of k-space sample shifts of

0.90 and 0.71 samples for gradient G_x and G_y, respectively) and among echoes (range of k-space sample shifts of 0.93 and 0.77 samples for gradient G_x and G_y, respectively) (Table 3-2). These observed differences support the need to calibrate independently for each echo and channel. Possible factors that caused the observed differences in apparent k-space sample shifts between different echoes and channels could include eddy current effects, local off-resonance effects, concomitant gradients, gradient cross terms, the existence of a non-linear gradient field, non-linear gradient amplifier amplification and limited gradient amplifier frequency response[138]. Some of these effects can vary depending on the patient[128]. For example, local off-resonance in a near a particular coil element would cause phase variation in the MRI image, which would manifest as an observed apparent k-space sample shift. Since in vivo liver images have more inhomogeneous tissue types and motion, this will induce greater off-resonance and could explain the larger channel variation. In addition, eddy current effects may be different for different echoes and this may cause differences in the phase and observed apparent k-space sample shifts. Investigating the potential causes of channel and echo variation will be a topic of future work.

For all experiments, when comparing Cartesian PDFF to radial PDFF, imaging parameters were matched as much as possible, including TE, bandwidth, spatial coverage, resolution, and the signal model. Note that echo times for the radial technique were chosen to match the Cartesian technique; however, they may not be the optimal echo times for maximizing the effective number of signal averages[90]. The inline scanner reconstruction method for Cartesian data uses a mixed fitting algorithm while radial data is reconstructed offline using complex fitting. It has been shown that CSE-MRI PDFF maps reconstructed from the same dataset with mixed fitting and complex fitting are highly concordant with each other and achieve significant correlation and agreement with SVS PDFF[42,44]. In addition, many studies have shown that PDFF

from both complex[36–38,41,87,88,121] and mixed fitting methods[56,93,139] achieve a significant correlation to SVS or known fat fraction phantoms. In this study, all ROIs were drawn by the same individual to correspond to the SVS ROIs, thereby limiting intra- and inter-observer variability. Future work will look at the effect of intra- or inter-observer variability for PDFF quantification.

For NAFLD diagnosis and monitoring, the accuracy of PDFF measurements for low-PDFF regions is important since the reference guideline for defining fatty liver is having liver PDFF > 5.6%[16,116] and clinically relevant liver PDFF usually ranges from 0%-30%[57,140–143]. For low-PDFF regions (< 5%), in vivo pelvis experiments showed |mean difference| < 0.21% when comparing PDFF between radial R = 1 and Cartesian R = 1,4. Additionally, in vivo liver experiments in healthy subjects showed a significant correlation with mean difference < 0.9% between FB radial R = 1,2,3 and BH Cartesian R = 4. These results provide promising evidence that the proposed FB radial technique can achieve accurate fat quantification in the liver for diagnosis of NAFLD.

For the in vivo liver experiments, the BH Cartesian R = 4 PDFF maps had some minor motion aliasing artifacts depending on the BH ability. Also, in the pelvis and liver, due to Cartesian R = 4 acceleration, there was increased noise compared to Cartesian R = 1 and radial R = 1. The Cartesian aliasing artifacts and increased noise with acceleration can potentially lead to errors in PDFF for low-fat regions, which could be exacerbated for patients who have more problems holding their breath compared to healthy subjects. The proposed FB radial approach may be more favorable to overcome these challenges.

Our study had several limitations. The prototype SVS inline reconstruction on the scanner does not fully account for the complexities in the fat spectrum: the fat peak in the a priori

7-peak fat spectral model near the water resonance is counted towards the integrated water signal, and not towards the fat signal. This resulted in differences in the PDFF measurements. To account for this, the SVS PDFF was corrected prior to comparison with radial and Cartesian CSE-MRI to reduce differences. However, the correction may not have removed all sources of differences in the fat models. In addition, SVS is subject to errors due to partial-volume effects and motion, which were not corrected. A second limitation is that inter-scan motion hinders PDFF comparisons between techniques due to changes in tissue ROI position. For example, variability in liver positions between BH and FB scans result in inter-scan liver positional changes. To account for this, all ROIs were placed in corresponding anatomical locations on the Cartesian and radial PDFF maps. A third limitation is that the scan time for the radial acquisition is increased by 31 seconds due to the addition of calibration spokes. In this study 20 calibration spokes were averaged to increase SNR for calibration; however an optimal number of calibration spokes to decrease the calibration scan time has not been determined. Finally, only healthy subjects were included in this study for preliminary evaluation. NAFLD patients have higher hepatic fat content compared to healthy subjects and may have more variable breathing patterns. Therefore, the proposed FB radial technique needs to be further evaluated in patient populations for fat quantification.

In this work, we leveraged the inherent robustness of radial trajectories to motion and no data rejection or binning was done prior to reconstruction. Since the radial acquisition was performed throughout free breathing and without motion gating, image data reflected an average of all respiratory motion states, which may result in slight blurring in the radial PDFF maps; however, this did not affect PDFF quantification. In addition, experiments comparing PDFF between FB radial and BH radial demonstrate that fat quantification using the FB radial

technique exhibits robustness to motion. Recent research has proposed using a 3D stack-of-radial trajectory with motion correction techniques for additional robustness to motion and removal of motion artifacts[98]. It may be advantageous to combine similar motion correction strategies for radial fat quantification. This work has shown that although the radial R = 2 and R = 3 PDFF maps may have increased noise and streaking compared to the radial R = 1 PDFF maps, the fat-water separation quality and PDFF accuracy is maintained. Further work includes combining this technique with non-Cartesian parallel imaging to improve undersampled source image quality by decreasing streaking artifacts, further decreasing scan time, and improving SNR for fat quantification.

3.5 Conclusion

We have demonstrated that rapid one- to two-minute 3D fat quantification of the entire liver can be performed using a new free-breathing bipolar multiecho stack-of-radial technique. This technique demonstrates agreement to the conventional BH Cartesian CSE-MRI technique and reference standard BH single-voxel MR spectroscopy, and may improve patient compliance and fat quantification for management of NAFLD.

This work has been published as:

Armstrong T, Dregely I, Stemmer A, Han F, Natsuaki Y, Sung K, Wu HH. Free-breathing liver fat quantification using a multiecho 3D stack-of-radial technique. Magnetic Resonance in Medicine 2018; 79(1):370-382. doi: 10.1002/mrm.26693

4 Evaluation of a Free-Breathing Radial MRI Technique for Hepatic fat Quantification in Children

4.1 Introduction

In the United States, 12.7 million children are obese[144] and 38% of obese children have NAFLD[145]. Liver biopsy is the gold standard for diagnosing and staging NAFLD in children[10,11]. However, biopsies are invasive, limited by sampling bias, require anesthesia, and can be associated with complications. Biopsies are also technically challenging[12,13], particularly in obese children. Complicating matters, inter-observer agreement among pathologists for NAFLD scoring can be variable[13,146,147]. For these reasons, there is a need for a non-invasive technique to accurately measure hepatic fat in children.

Magnetic resonance spectroscopy (MRS) is regarded as the non-invasive reference standard for fat quantification in children[14,15] and accurately quantifies hepatic steatosis[16–18]. However, MRS only measures fat content in a single spatial location (i.e., voxel) and is limited by spatial sampling bias[14,15]. CSE-MRI methods have mainly been investigated in adults with a few studies in children[45–48]. In adults, CSE-MRI PDFF accurately detects and quantifies hepatic steatosis when compared to MR spectroscopy[44] and liver biopsy[72,95].

Conventional MRI techniques, including CSE-MRI methods[43,44,55,56], typically employ Cartesian trajectories for MR image acquisition[43,58,59]. Cartesian trajectories require a breath-hold (see **section 2.6**). However, breath-holding is limited or not feasible in many patients (adults and children)[43,58,59]. Even when children are able to suspend respiration, inconsistency and reduced breath-hold capacity compromise diagnostic information. While respiratory gating and self-navigation strategies for Cartesian MRI sequences can be used to mitigate motion artifacts[64,100], these strategies require longer and potentially variable scan times, and image quality may still suffer[43]. For these reasons, children may be sedated for abdominal MRI scans. However, sedation can have negative side effects and complications, particularly in children[59,148]. As a result, there is a need for new free-breathing MRI techniques that overcome the challenges of traditional breath-held MRI and avoid the need for sedation.

Non-Cartesian trajectories provide an alternative for MR imaging in children that eliminates the need for a breath-hold and sedation. Non-Cartesian 3D stack-of-radial trajectories (also known as stack-of-stars) have dispersed motion artifacts in the radial encoding direction (in-plane) that do not obscure the anatomy, making radial trajectories more robust to breathing motion (see **section 2.7**)[43,58,59,61,62,149]. As a result, radial MRI scans can be acquired while free-breathing, allowing for greater liver coverage, higher spatial resolution, and/or increased SNR.

Recently, a new free-breathing multiecho 3D stack-of-radial MRI technique (FB radial) with gradient error calibration and correction was developed for PDFF quantification in adults[149]. This technique acquires MRI data continuously during a free-breathing scan, reconstructs images, and calculates PDFF maps. The hepatic PDFF measurements generated by FB radial PDFF demonstrated a high degree of agreement to standard breath-held single-voxel MR spectroscopy (BH SVS) and breath-held Cartesian (BH Cartesian) CSE-MRI techniques[149]. However, to date, there is no research on free-breathing hepatic fat quantification in children. Accordingly, this study's purpose is to compare the image quality, accuracy, and repeatability of this FB radial technique[149] to conventional BH Cartesian and BH SVS techniques for hepatic fat quantification in children.

4.2 Methods

4.2.1 Pediatric Study Population

This study was approved by our local institutional review board. Parents/legal guardians provided informed consent and children provided assent. Healthy children and children with NAFLD, ages 7-17 years, were enrolled. Exclusion criteria included known liver disease (excluding NAFLD for children with NAFLD), infections, diseases, or congenital anomalies known to affect the liver, contra-indications to MRI, and inability to comply with BH instructions.

4.2.2 Pediatric Liver MR Experiments

MRI experiments were performed on a 3 T scanner (MAGNETOM Skyra or Prisma, Siemens, Erlangen, Germany) using a spine array coil and body matrix array. Sequences acquired during the scan included a commercially available BH 3D Cartesian CSE-MRI[56] with

controlled aliasing in parallel imaging results in higher acceleration (CAIPIRINHA)[134] reconstruction (qDixon, the LiverLab package, software version VE11, Siemens, Erlangen, Germany), a commercially available BH single-voxel MR spectroscopy (SVS)[129] (HISTO, the LiverLab package, software version VE11, Siemens, Erlangen, Germany), and FB radial[149] sequences. Each sequence was repeated for each subject in random order within each scan session to evaluate repeatability. Except for the acceleration factor and the number of slices, the same imaging parameters were used for BH Cartesian and FB radial to enable a fair comparison between techniques (Table 4-1). The SVS voxel size was 25mm × 25mm × 25mm with a total acquisition time of 15 seconds. SVS imaging parameters included echo times of 12ms, 24ms, 36ms, 48ms, and 72ms, a repetition time of 3000ms, a mixing time of 10ms, a vector size of 1024, and a bandwidth of 1200Hz/pixel. Additional MRI scans were repeated if motion artifacts resulted in non-diagnostic images. The BH SVS region of interest (ROI) was positioned to avoid regions with image artifacts on BH Cartesian, large blood vessels, and bile ducts.

Table 4-1 Representative sequence parameters for in vivo pediatric liver experiments. A slice-oversampling factor of 18-25% was used for the acquisitions. Imaging parameters for free-breathing (FB) radial and breath-hold (BH) Cartesian were matched as much as possible for each subject. The number of slices was adjusted depending on scan time and the subjects' BH ability. TE, echo time; TR, repetition time.

Imaging Parameters	BH Cartesian	FB Radial
TE (ms)	1.23, 2.46, 3.69, 4.92, 6.15, 7.38	1.23, 2.46, 3.69, 4.92, 6.15, 7.38
ΔTE (ms)	1.23	1.23
TR (ms)	8.85	8.85
Matrix (N_x x N_y)	160-288 x 160-288	160-288 x 160-288
Field of View (mm_x x mm_y)	280-500 x 280-500	280-500 x 280-500
Resolution (mm_x x mm_y)	1.67-1.94 x 1.67-1.94	1.67-1.94 x 1.67-1.94
Slice Thickness (mm)	5	5
Number of Slices	20-40	36-52
Radial Spokes	N/A	252-453
Flip Angle (degrees)	5	5
Bandwidth (Hz/pixel)	1080-1160	1080-1160
Acceleration Factor	4	1
Scan Time (min:s)	0:16-0:25	2:09*-4:43*

***The FB radial gradient calibration scan time (31-45s) is included.**

◆Based on Nyquist criteria to collect fully-sampled data with $N_x \times \pi/2$ spokes.

4.2.3 MR Image Reconstruction and PDFF Calculation

BH Cartesian acquisitions were reconstructed[56] and PDFF maps were determined by a prototype scanner software (Work-In-Progress package 963, software version VE11, Siemens, Erlangen, Germany). The BH Cartesian PDFF maps were calculated using a 7-peak fat model[96] and single effective R_2^* per voxel[56]; BH SVS PDFF was calculated by the scanner software using T_2 correction[129]. FB radial datasets (fully-sampled based on Nyquist criteria) were reconstructed, without discarding data or employing parallel imaging reconstruction techniques. FB radial

PDFF maps were calculated offline (see **section 3.2.3**)[149] in MATLAB R2016b (MathWorks, Natwick, MA, United States) using the same signal model used for BH Cartesian[96], complex fitting with a graph cut algorithm[34,35,132], and magnitude discrimination[41].

4.2.4 Image Analysis

All reconstructed images and PDFF maps were converted to DICOM for analysis in OsiriX. Image quality was evaluated by an experienced pediatric radiologist (S.G., >10 years of experience) masked to the trajectory (Cartesian or radial) and subject, by scoring the first echo time images (TE = 1.23ms) and PDFF maps in axial and coronal orientations. Images were scored on a scale of 1-4 for motion artifacts, other imaging artifacts, and image blurring. Motion artifacts included coherent aliasing artifacts on BH Cartesian images and radial streaking on FB radial images. Other artifacts included CAIPIRINHA reconstruction artifacts on BH Cartesian images and any additional non-motion-related artifacts on BH Cartesian and FB radial images. Motion blurring referred to blurring of blood vessels, abdominal wall, or liver dome on BH Cartesian and FB radial images. The criteria for a score of 1 was non-diagnostic images with significant artifacts that confound PDFF (i.e. bad image quality); 2 indicated diagnostic images with artifacts that confound PDFF; 3 indicated diagnostic images with artifacts that did not confound PDFF; 4 indicated no artifacts (i.e. good image quality). The percentage of images that fell into each score category was determined. To characterize liver coverage, the number of slices that contained the liver using the BH Cartesian scan (Nsl_C) and the FB radial scan (Nsl_R) was counted. FB radial scans were always prescribed to cover the entire liver. The liver slice coverage (Lsl) was then calculated as the percentage of liver slices covered using BH Cartesian relative to FB radial (i.e. $Lsl = Nsl_C/Nsl_R \times 100\%$) and reported as mean ± standard deviation (SD). To evaluate quantitative hepatic PDFF accuracy, one ROI was drawn on each of the BH

Cartesian and FB radial PDFF maps in an anatomical location corresponding to the BH SVS ROI that was placed during the MR scan, and PDFF was recorded as mean ± SD.

4.2.5 Statistical Analysis

Age was described between healthy subjects and NAFLD subjects and the median values and interquartile range (IQR) was compared using a nonparametric two group Mann-Whitney U[150,151] test due to the limited sample size. Paired differences in image quality scores between BH Cartesian (i.e. conventional reference) and FB radial, were assessed using McNemar-Bowker tests for dependent categorical data to compare the distribution of scores by cohort (healthy cohort and NAFLD cohort) and artifact category (motion artifacts, other artifacts, and motion blurring)[152].

Linear regression and Bland-Altman analysis[112] was performed to assess differences between FB radial and BH techniques (see **section 2.9**). Repeatability analysis[113,114] was performed using back-to-back scans during a single scan session for each technique (see **section 2.10**). Statistical analyses were performed in STATA and MATLAB. A P-value < 0.05 was considered significant.

4.3 Results

4.3.1 Pediatric Study Population

Ten healthy subjects and ten NAFLD subjects were enrolled. Of these subjects, all ten healthy subjects (six male, median age (± IQR), 10.9 (± 3.3) years) and nine NAFLD subjects (seven male, age, 15.2 (± 3.2) years) completed the study. The median age between the two groups was significantly different ($P < 0.05$). One NAFLD subject did not complete the study because the MRI field of view (FOV) was not adequate to cover his/her body habitus. All of the

NAFLD subjects were confirmed by BH SVS or BH Cartesian to have hepatic PDFF > 5.6%[16,116], consistent with a diagnosis of NAFLD.

4.3.2 Image Quality

If the BH Cartesian images showed significant aliasing artifacts due to motion or if the BH liver position changed such that the images from the BH Cartesian scan did not adequately cover the liver volume, BH Cartesian scan(s) were repeated. For some subjects, motion-induced aliasing or other artifacts were still observed on BH Cartesian images even when repeated. The number of repeated BH Cartesian scans ranged from 0-2 for all subjects. Specifically, the mean number of repeated BH Cartesian scans performed was 0.40 ± 0.70 in healthy subjects and 0.89 ± 0.93 in NAFLD subjects. In contrast, the FB radial was only repeated once for one healthy subject.

The FB radial technique demonstrated robustness to motion with good image quality and quantitative PDFF maps. Representative images of BH Cartesian and FB radial acquisitions with motion artifact image quality scores ranging from 1-4 are shown in Figure 4-1. Figure 4-2 shows an example of BH Cartesian and FB radial images and PDFF maps from a representative subject where major and minor motion occurred during a BH Cartesian scan.

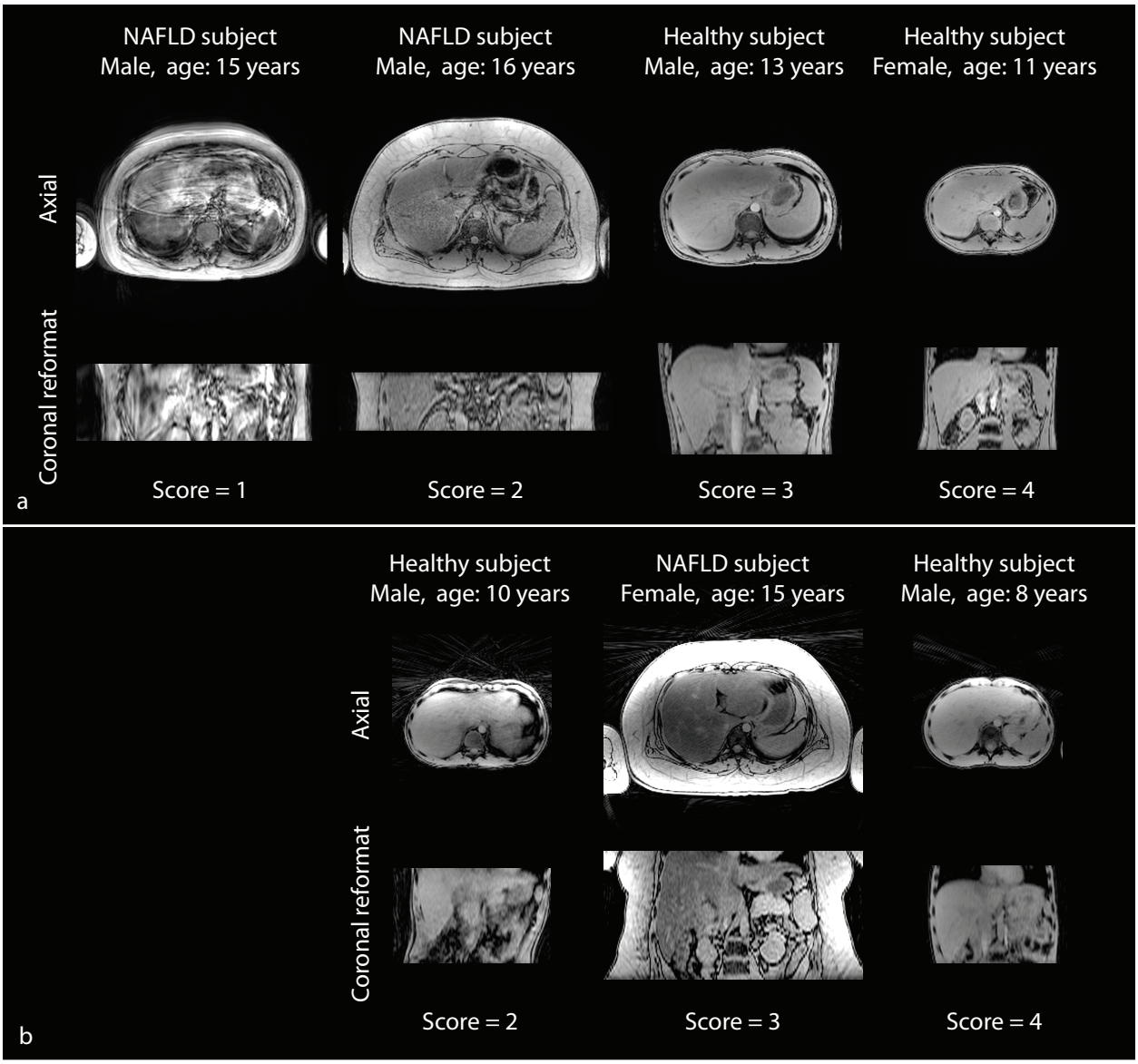

Figure 4-1 Representative images in the axial and coronal reformat orientations at an echo time of 1.23ms with motion artifacts scores of 1-4 for (a) breath-hold (BH) Cartesian and 2-4 for (b) free-breathing (FB) radial acquisitions. If BH Cartesian exhibited severe motion artifacts leading to non-diagnostic images (score of 1), additional scans were repeated during the scan session. FB radial did not have a representative image with an image quality score of 1. See the Image Analysis section of the Methods for the description of the image quality scores.

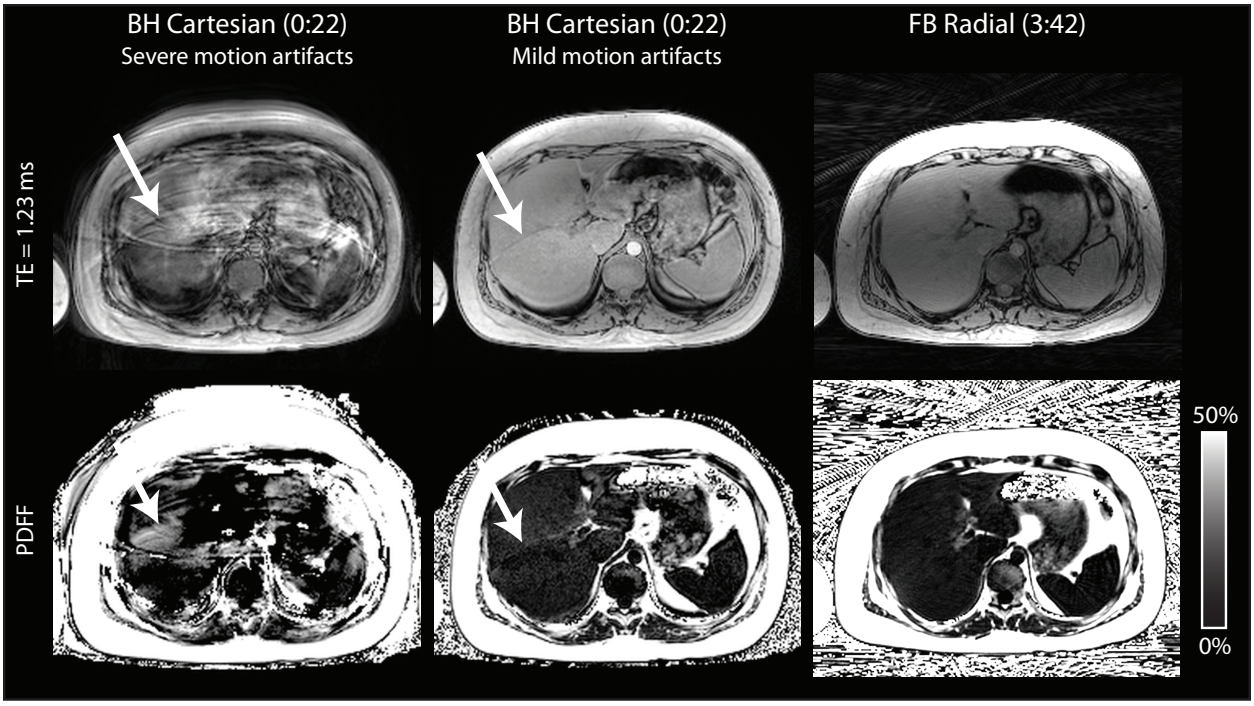

Figure 4-2 Images and proton-density fat fraction (PDFF) maps for the free-breathing (FB) radial and breath-hold (BH) Cartesian scans for a representative subject (male, age: 15 years) in axial orientation. Due to severe motion artifacts (non-diagnostic image quality) in the BH Cartesian scan (motion artifact score = 1), it was repeated. However, mild motion artifacts (motion artifact score = 3) were still present in the repeated scan. Arrows indicate artifacts that affect hepatic fat quantification. The FB radial scan did not exhibit coherent motion artifacts in the liver (motion artifact score = 3). The scan time for each technique is reported as minutes:seconds.

Axial, reformatted coronal, and reformatted sagittal PDFF maps from FB radial and BH Cartesian techniques for a representative healthy subject and NAFLD subject are shown in Figure 4-3 and Figure 4-4, respectively. The PDFF maps from FB radial and BH Cartesian are similar, but have slight differences in liver position due to the BH. Additionally, in some subjects, hepatic PDFF heterogeneity was observed using both BH Cartesian and FB radial techniques (Figure 4-5).

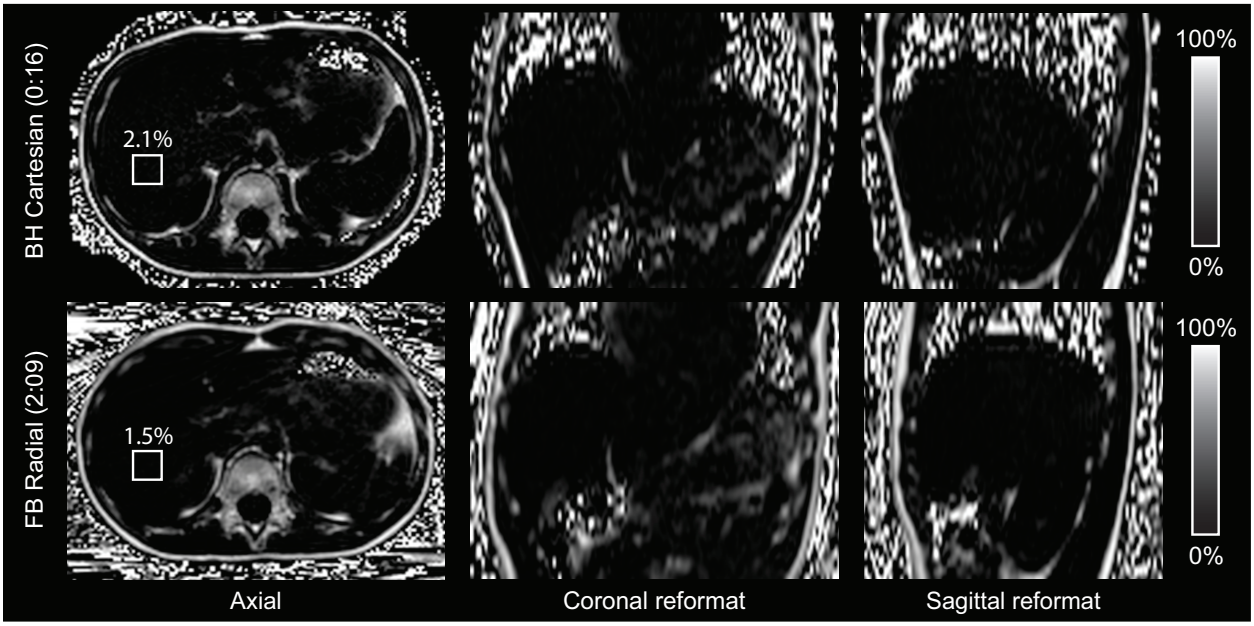

Figure 4-3 Proton-density fat fraction (PDFF) maps for breath-hold (BH) Cartesian and free-breathing (FB) radial scans for a representative healthy subject (male, age: 9 years) in axial, coronal, and sagittal orientations. The liver slice coverage was 100% using the BH Cartesian technique for this subject. Representative regions of interest (ellipses) and mean PDFF values are shown in the axial orientation. FB radial and BH Cartesian have slight differences in liver position due to breath-holding. The scan time for each technique is reported as minutes:seconds.

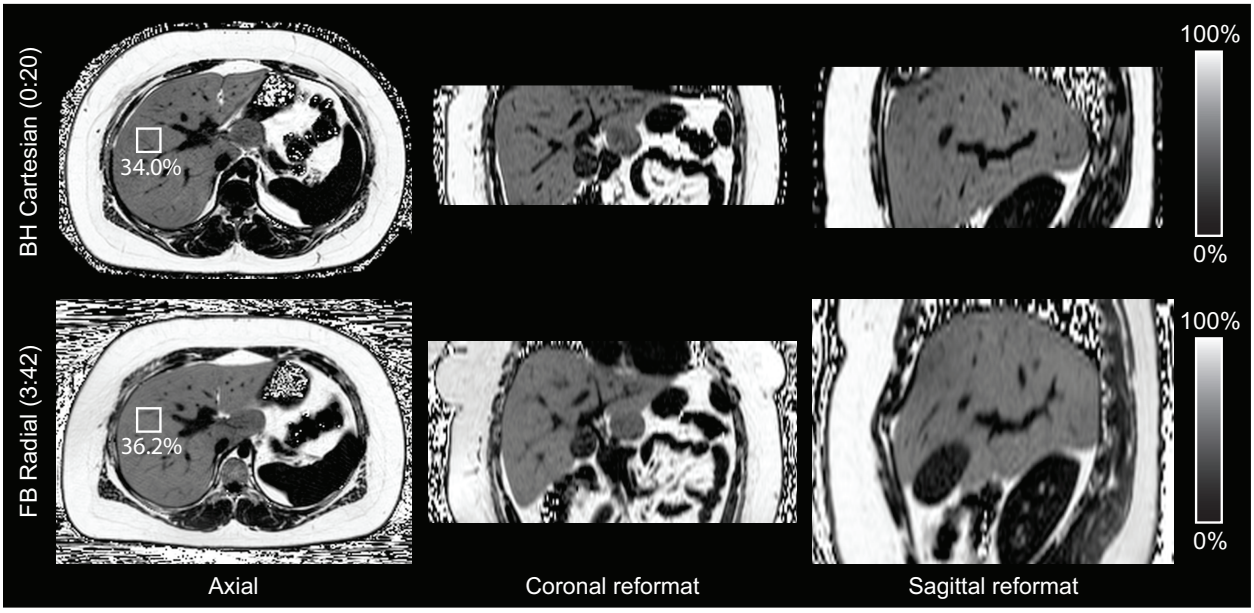

Figure 4-4 Proton-density fat fraction (PDFF) maps for breath-hold (BH) Cartesian and free-breathing (FB) radial scans for a representative non-alcoholic fatty liver disease (NAFLD) subject (female, age: 14 years) in axial, coronal, and sagittal orientations. The liver slice coverage was 68% using the BH Cartesian technique for this subject. Representative regions of interest (box) and mean PDFF values are shown in the axial orientation. FB radial and BH Cartesian have slight differences in liver position due to breath-holding. The scan time for each technique is reported as minutes:seconds.

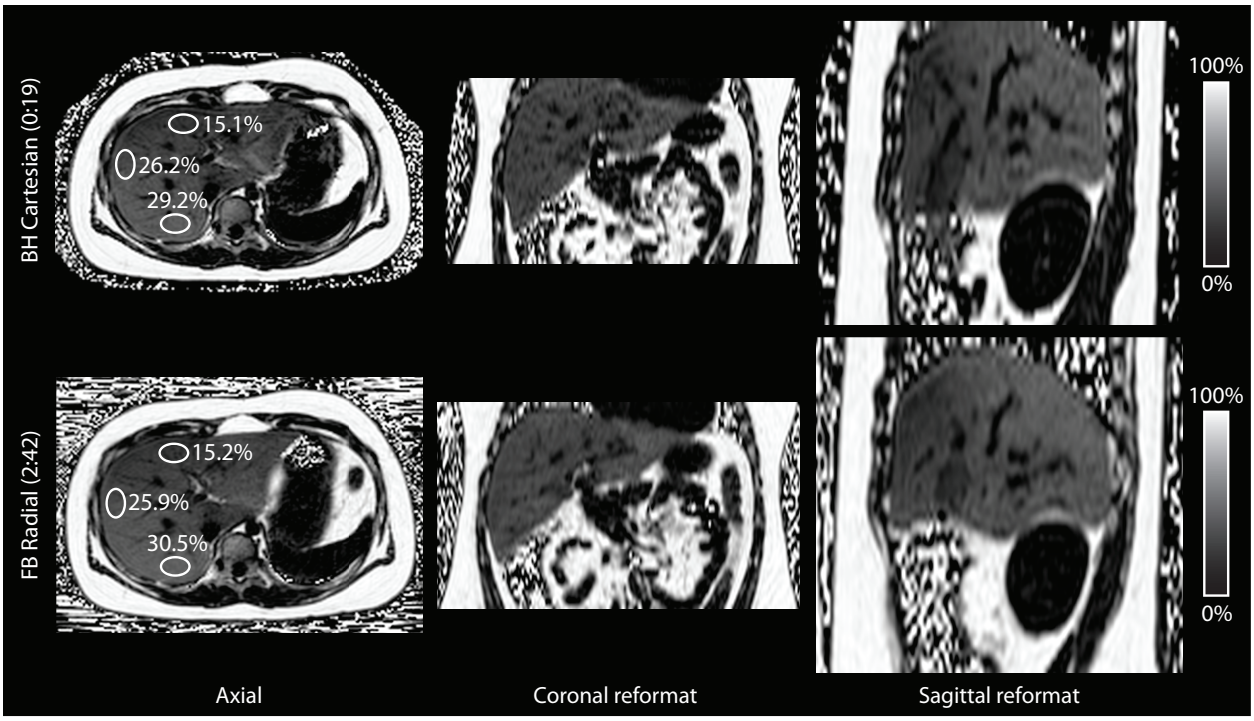

Figure 4-5 Proton-density fat fraction (PDFF) maps for breath-hold (BH) Cartesian and free-breathing (FB) radial scans for a representative non-alcoholic fatty liver disease (NAFLD) subject (male, age: 10 years) with hepatic PDFF heterogeneity. The liver slice coverage was 97% using the BH Cartesian technique for this subject. Representative regions of interest (box) and mean PDFF values are shown in three liver segments. FB radial and BH Cartesian have slight differences in liver position due to breath-holding. The scan time for each technique is reported as minutes:seconds.

In healthy subjects, the BH Cartesian scan achieved full liver slice coverage with the resolution used in this study. However, in most NAFLD subjects, full liver slice coverage was not achieved using the BH Cartesian technique. In NAFLD subjects, the liver slice coverage was 100% ± 0% for FB radial while it was 74% ± 17% for BH Cartesian. To maintain similar resolution between all subjects, many NAFLD subjects required a larger matrix size than healthy subjects due to a larger FOV. Furthermore, some NAFLD subjects had limited BH ability and the volumetric coverage needed to be reduced further to decrease the BH time. Table 4-2 shows that for NAFLD subjects, FB radial had a significantly higher proportion of good motion artifact and other artifact image quality scores compared to BH Cartesian ($P < 0.05$). In both NAFLD and healthy subjects, the proportion of image blurring scores was not significantly different

between FB radial and BH Cartesian.

Table 4-2 Radiologist image quality scores for the breath-hold (BH) Cartesian and free-breathing (FB) radial first echo time images and proton density fat fraction (PDFF) maps for motion artifacts, other artifacts, and image blurring for the healthy and NAFLD pediatric subjects. Images were scored on a scale of 1-4 where a score of 1 indicates bad image quality and 4 indicates good image quality.

	Healthy Subjects (n = 10)		NAFLD Subjects (n = 9)	
Motion Artifacts	**BH Cartesian***	**FB Radial***	**BH Cartesian***	**FB Radial***
1 (bad)	0%	0%	0%	0%
2	0%	5%	56%	11%
3	40%	80%	28%	83%
4 (good)	60%	15%	17%	6%
Other Artifacts	**BH Cartesian**	**FB Radial**	**BH Cartesian***	**FB Radial***
1 (bad)	0%	0%	0%	0%
2	0%	0%	61%	0%
3	70%	85%	33%	89%
4 (good)	30%	15%	6%	11%
Image Blurring	**BH Cartesian**	**FB Radial**	**BH Cartesian**	**FB Radial**
1 (bad)	0%	0%	0%	0%
2	0%	0%	0%	0%
3	60%	85%	50%	44%
4 (good)	40%	15%	50%	56%

***Statistically significant differences ($P < 0.05$) in the distribution of image quality scores between BH Cartesian and FB radial techniques.**

4.3.3 Hepatic PDFF Quantification Accuracy

To avoid PDFF errors due to coherent Cartesian aliasing artifacts, all ROIs measured on the BH SVS, FB radial images, and BH Cartesian images were positioned away from these

Cartesian MRI artifacts for quantitative analysis. The results showed a linear relationship between BH Cartesian PDFF, BH SVS PDFF and the proposed FB radial PDFF. All comparisons had a significant r and $\rho_c > 0.99$ ($P < 0.001$) and MD < 0.7%. The linear correlation and Bland-Altman plots are shown in Figure 4-6. The comparison between the proposed FB radial versus BH Cartesian showed a slope of 1.03 for the linear regression and correlation coefficients r and ρ_c were 0.996 and 0.994, respectively. For the proposed FB radial versus BH SVS, the slope of the linear regression was 0.97 and the correlation coefficients r and ρ_c were 0.997 and 0.995, respectively. The conventional BH Cartesian versus the reference BH SVS comparison showed a slope of the linear regression of 0.94 and the correlation coefficients r and ρ_c were 0.997 and 0.995, respectively. The MD between FB radial and BH Cartesian was 0.65% ± 2.56%, the MD between FB radial and BH SVS was 0.64% ± 2.31%, and the MD between the conventional BH Cartesian and reference BH SVS was 0.23% ± 2.56%. FB radial, BH Cartesian, and BH SVS also demonstrated repeatability with MD_{within} = 0.25%, -0.09%, and -0.30%, respectively; SD_{within} = 0.55%, 0.32%, and 1.35%, respectively; CR = 1.53%, 0.89%, and 3.74%, respectively. A summary of the repeatability analysis is shown in Table 4-3.

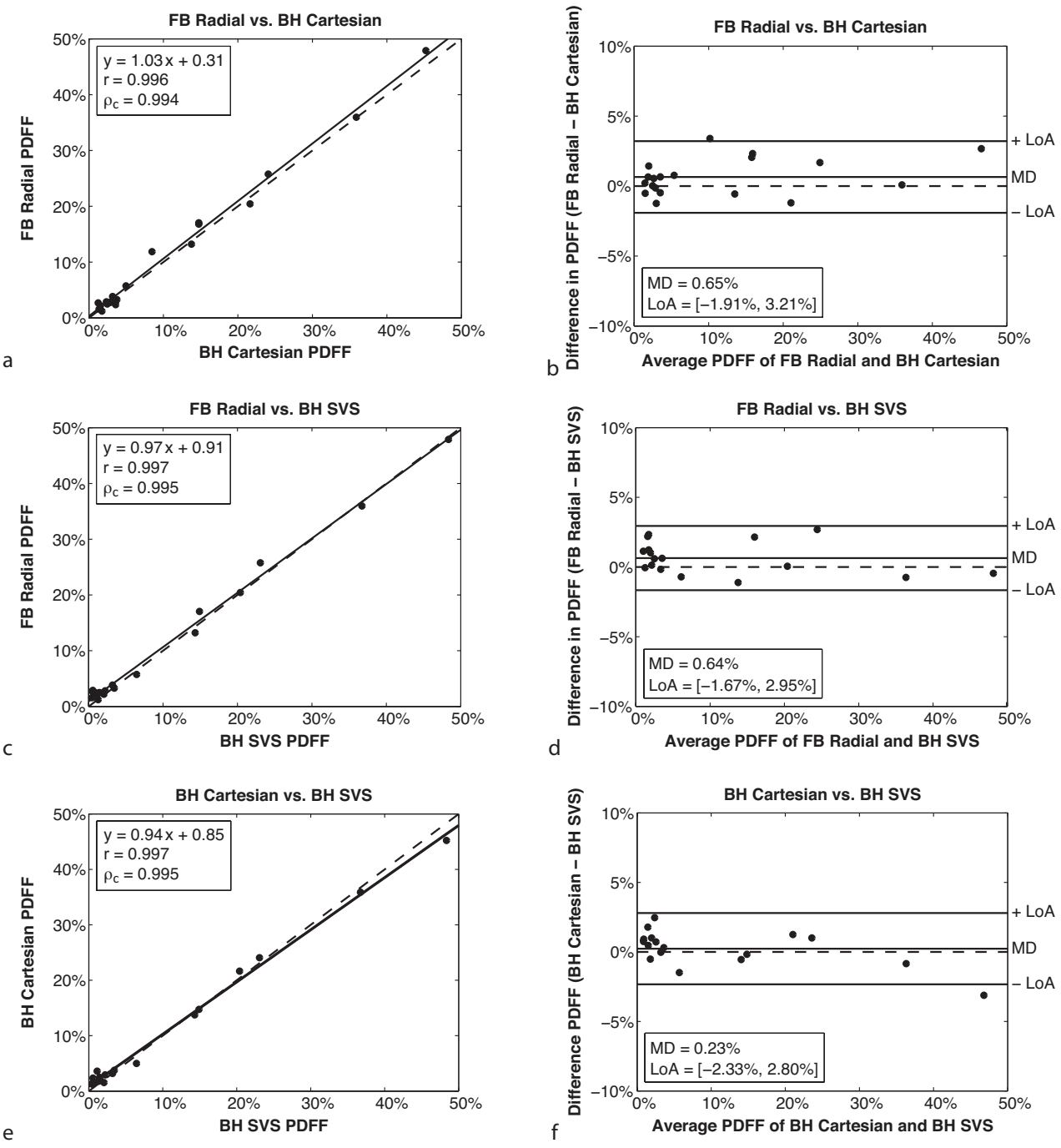

Figure 4-6 Liver study (a,c,e) linear correlation plots and (b,d,f) Bland-Altman plots for proton-density fat fraction (PDFF) of each region of interest (ROI) in the liver corresponding to single-voxel magnetic resonance spectroscopy (SVS) ROIs. The comparison of (a-b) free-breathing (FB) radial versus breath-hold (BH) Cartesian had mean difference (MD) = 0.65% ± 2.56% (c-d) FB radial versus BH SVS had MD = 0.64% ± 2.31%, (e-f) BH Cartesian versus BH SVS had MD = 0.23% ± 2.56%. The correlation coefficients r and ρ_c were significant in all cases with P < 0.001. The dashed lines represent y = x in the linear correlation plots and y = 0 in the Bland-Altman plots.

Table 4-3 The analysis of repeatability results. The mean difference (MD_{within}), within-subject standard deviation (SD_{within}), and the coefficient of repeatability (CR) are reported between repeated scans for the breath-hold (BH) single-voxel magnetic resonance spectroscopy (SVS), BH Cartesian and free-breathing (FB) radial techniques.

Technique	MD_{within} (%)	SD_{within} (%)	$CR = 1.96 \times \sqrt{2} \times SD_{within}$ (%)
FB Radial	0.2521	0.5520	1.5300
BH Cartesian	-0.0911	0.3210	0.8897
BH SVS	-0.2969	1.3496	3.7408

4.4 Discussion

This is the first study to evaluate the accuracy and repeatability of 3D hepatic PDFF quantification using a FB radial MRI technique with respect to established BH techniques in a pediatric population. This study provides evidence that accurate and repeatable FB hepatic fat quantification can be performed in children for the entire 3D liver volume using a multiecho 3D stack-of-radial technique. Hepatic PDFF calculated from FB radial scans had significant linear correlation, significant concordance, and low mean differences < 0.7% compared to the conventional BH Cartesian and the reference standard BH SVS techniques. FB radial, BH Cartesian and BH SVS demonstrated repeatability with MD_{within} < 0.3%. FB radial and BH Cartesian demonstrated repeatability with CR < 2%. BH SVS had a larger CR of 3.74% likely due to variation in the BH position and actual voxel position between BH SVS scans. While the mean PDFF differences between FB radial and BH techniques were very small, they may reflect differences due to BH position, SVS partial volume effects, and the effect of motion on the images. However, in NAFLD subjects, FB radial demonstrated a significantly higher proportion

of good image quality scores compared with BH Cartesian. We speculate that NAFLD subjects may have had more difficulty performing a breath-hold than their healthy peers because they were overweight. The median (± IQR) body mass index in the NAFLD cohort was 33.2 (± 7.1) kg/m^2. In contrast, the body mass index in the healthy cohort was normal at 17.4 (± 2.0) kg/m^2. Therefore, compared to the conventional BH Cartesian technique, FB radial may provide improved image quality and hepatic PDFF quantification for the evaluation of steatosis in this target population.

There have been a few studies evaluating BH Cartesian CSE-MRI techniques for hepatic PDFF quantification in children[45–48]. Two studies used dual-echo and triple-echo methods for PDFF quantification[45,48]. However, dual-echo and triple-echo approaches do not correct for confounding factors (such as T_2* bias) and, as result, hepatic PDFF quantification may be inaccurate[39]. Since the signal model includes many parameters, at least four echoes are recommended to account for confounding factors such as T_2* bias and the multi-peak spectrum of fat (e.g. not correcting for T_2* will cause an underestimated hepatic fat fraction)[39,121]. Other studies utilized a six-echo technique with magnitude-based fitting for PDFF estimation in the liver and found agreement between BH Cartesian PDFF and BH SVS PDFF[46], correlation between BH Cartesian PDFF and histopathology[47], and associations between BH Cartesian PDFF and clinical characteristics[48]. These studies employed a 2D BH Cartesian MRI technique[45–48], which may have limited spatial coverage or resolution and motion artifacts.

In this study, variation in the distribution of image quality scores between BH Cartesian and FB radial was dependent upon the artifact category and subject population. Blurring was observed in BH Cartesian and FB radial images with no statistically significant differences in the distribution of scores for both healthy subjects and NAFLD subjects, and this did not affect

PDFF quantification. In the motion artifact category, BH Cartesian images have coherent aliasing artifacts that may confound hepatic PDFF while FB radial images have radial streaking artifacts that interfere less with hepatic PDFF. In NAFLD subjects, the percentage of bad image quality scores for motion artifacts was higher for BH Cartesian than for FB radial. We believe this is because children with NAFLD may have difficulty performing a BH due to impaired lung function secondary to their overweight/obesity status. Additionally, in NAFLD subjects, BH Cartesian scans showed a higher percentage of bad image quality scores for other artifacts. One of the main sources of these artifacts is related to under-sampling and CAIPIRINHA reconstruction errors. This is most likely due to the fact that the center of the FOV's coil sensitivity is reduced by a large body size. In order to improve Cartesian image quality for NAFLD subjects, less undersampling may be required, which would increase scan time, reduce volumetric coverage, and/or reduce spatial resolution. On the other hand, FB radial does not necessarily require parallel imaging or have BH scan time limitations. Therefore, image quality can be improved by allowing for longer FB acquisition times for NAFLD subjects.

In this study, BH Cartesian required four-fold undersampling to reduce the scan time to within a BH. For this reason, volumetric coverage was limited. As a result, for children with hepatomegaly, full liver slice coverage with the desired spatial resolution may not be achievable within a BH. FB radial can achieve greater volumetric coverage and/or spatial resolution compared to BH Cartesian, thereby improving 3D spatial characterization of hepatic PDFF and liver disease. This may be important for cases where hepatic PDFF is heterogeneous, as depicted in Figure 4-5. Other studies have reported heterogeneous hepatic PDFF in adults[153–155] and children[156], and recent evidence suggests heterogeneity in reduction of hepatic fat following bariatric surgery[157]. However, additional studies are required for a full understanding of the

spatial distribution of PDFF in patients with NAFLD. In addition, full liver coverage achieved by FB MRI may have additional clinical applications including the evaluation of hepatic masses or other diseases. Traditionally, complex hepatic diseases require sedation or general anesthesia for MRI in order ensure full liver coverage and adequate resolution. FB MRI technology eliminates this requirement, and at the same time can yield diagnostically useful information. Each FB radial acquisition in this study was performed with the same image resolution for children with either a small or large body habitus, and the number of slices was chosen to cover the entire liver volume. For these reasons, fully-sampled FB radial acquisitions were approximately 3-5 minutes depending upon the subject's size (Table 4-1). The FB radial scan time could be shortened if less slices are acquired or a lower resolution is used. On the other hand, higher resolutions may improve diagnostic information when performing MRI scans, but this may require longer scan times or reduced liver slice coverage. While the radial trajectory was fully-sampled in this study, radial undersampling can be performed in combination with non-Cartesian parallel imaging reconstruction[158]. Previous work in adults showed similar PDFF quantification results using an undersampled FB radial technique, potentially reducing the scan time to less than one and a half minutes[149,159].

In addition to the constraints of BH Cartesian with respect to liver coverage and spatial resolution, patient motion leads to artifacts and reduces image quality. Previous studies have developed respiratory gating and self-navigation strategies for hepatic fat quantification using Cartesian MRI sequences to reduce motion artifacts in adults[64,100]. To our knowledge, these strategies have not been evaluated for hepatic fat quantification in children. In adults, these strategies have shown similar image quality and fat quantification accuracy compared to BH techniques[64,100]. However, these strategies require longer scan times for image acquisition and

are well suited for patients with regular respiratory patterns, but may not be appropriate for children who require shorter scan times and have heavy or irregular breathing[43,64]. In fact, respiratory gating and self-navigation strategies may benefit from the incorporation of non-Cartesian trajectories, such as 3D stack-of-radial, to accommodate patients with heavy or irregular breathing. Although self-navigation using FB radial was not evaluated in the current study, the 3D stack-of-radial trajectory allows for self-navigation and improved image quality in the presence of motion[98,160].

The signal model used in this study includes fitting for R_2^*, which can be used to assess hepatic iron content[57,161–163]. Severe hepatic iron overload may hinder PDFF quantification due to rapid signal decay prior to acquiring the first echo time[57]. Recent work includes ultra-short echo time sequences for R_2^* mapping in patients with severe iron overload[164–166]. In this study, there were no subjects with severe iron overload. Therefore, hepatic PDFF quantification was not confounded by high R_2^* values.

Our study has limitations. First, partial-volume effects and motion can confound BH SVS, which were not corrected. Second, inter-sequence motion and non-rigid changes in liver tissue during a BH and while FB, may hinder PDFF comparisons between techniques. To address this limitation, ROIs were placed in corresponding anatomical locations on BH Cartesian and FB radial PDFF maps. Third, the scan time for the radial acquisition is increased by 31-45 seconds due to the addition of a calibration scan for radial MRI and the number of radial readouts needed for calibration was not optimized to reduce scan time. Finally, the sample size is small and this study was performed at a single site. However, the results of this study indicate that FB radial is not only comparable to conventional BH MR techniques, but also has some additional advantages for hepatic fat quantification in children.

4.5 Conclusion

In this study of healthy children and children with NAFLD, FB hepatic fat quantification using a new 3D stack-of-radial MRI technique was accurate and repeatable. FB radial demonstrated significantly less image artifacts than BH Cartesian in NAFLD subjects. These results show that FB radial may potentially improve pediatric patient compliance and 3D spatially resolved characterization of hepatic steatosis. Moreover, in this study, FB radial eliminated the need for breath-holding and did not require sedation for fat quantification. FB radial represents a promising tool that could help clinicians diagnose and manage children with NAFLD.

This work has been published as:

Armstrong T, Ly KV, Murthy S, Ghahremani S, Kim GHJ, Calkins KL, Wu HH. Free-breathing quantification of hepatic fat in healthy children and children with nonalcoholic fatty liver disease using a multi-echo 3-D stack-of-radial MRI technique. Pediatric Radiology 2018; 48(7):941-953. doi: 10.1007/s00247-018-4127-7

5 FREE-BREATHING RADIAL MRI QUANTIFICATION OF BODY COMPOSITION AND HEPATIC FAT IN INFANTS

5.1 Introduction

The pediatric obesity epidemic highlights the need to better understand the amount, distribution, and content of adiposity in children, beginning at an early age[19–21]. Two types of fat, white adipose tissue (WAT) and brown adipose tissue (BAT), are of interest because WAT stores triglycerides and BAT metabolizes fat to produce heat[167]. In the abdomen, WAT is categorized as either visceral adipose tissue (VAT), located inside the abdominal cavity, or subcutaneous adipose tissue (SAT), located outside the abdominal cavity[167]. Brown adipose tissue (BAT) is generally located in the axillary, cervical, perirenal, and periadrenal regions[167]. Tissue fat content is related to the proportion of different types of fat; higher fat content may

indicate "WAT-like" tissue and lower fat content may be associated with "BAT-like" tissue[50,51,168].

The hepatic manifestation of metabolic syndrome, non-alcoholic fatty liver disease, is characterized by hepatic steatosis, abnormally high hepatic fat content. In older children and young adults, abnormal hepatic fat content is associated with future metabolic syndrome[2,77,169]; however, additional longitudinal studies are needed to determine its predictive value in infants. There have been studies observing increased hepatic fat in infants born to obese mothers with and without gestational diabetes, which are risk factors for future metabolic syndrome[170,171].

Magnetic resonance spectroscopy (MRS) and magnetic resonance imaging (MRI) are non-invasive techniques that can be utilized to quantify body composition and hepatic fat content in early infancy[2,19,49–53,71,167,169–175]. MRI and MRS are well suited for children since they do not involve ionizing radiation[19,71]. MRS is regarded as the non-invasive reference standard for quantifying hepatic fat content in children and adults[14,15,176]. However, MRS techniques have limitations due to partial volume effects, spatial sampling bias, and motion. MRS techniques only measure fat content in a specified voxel and do not provide information about fat distribution. MRI has excellent soft tissue contrast and can obtain high-resolution 3D images[19,71]. Intensity-based MRI techniques can provide spatially resolved information about fat distribution and volume[53,170–173], but do not provide information about fat content. Chemical-shift-encoded MRI (CSE-MRI) techniques can provide spatially resolved information about fat distribution, volume, and content[51,53] by quantifying proton-density fat fraction (PDFF), a standardized MRI biomarker[70]. In general, conventional MRI scans are performed using Cartesian sampling[49–53,168,170–175], which is limited by sensitivity to motion-induced coherent aliasing artifacts that can obstruct the anatomy of interest, degrade image quality, and hinder quantification (see **section**

2.6). Therefore, scans using Cartesian trajectories are typically performed while breath-holding. However, infants cannot hold their breath, often breathe heavily and irregularly, and may become anxious and cry during the MRI exam. This leads to increased motion artifacts[177–180]. For these reasons, sedation or anesthesia is prescribed, which introduces additional risks and costs[177–180]. As a result, there are a limited number of MRI studies investigating VAT, SAT, BAT, and hepatic fat in infants[49–52,170–175].

Compared to Cartesian MRI, non-Cartesian MRI based on 3D stack-of-radial sampling may provide greater robustness to motion, due to the dispersed distribution of motion artifacts[63,149] (see **section 2.7**). The 3D stack-of-radial trajectory allows for considerably less obtrusive motion artifacts that do not obscure the anatomy of interest, allowing for the MRI scan to be performed during free-breathing (FB)[149,181]. In older children, when compared to conventional breath-held Cartesian MRI, a recently developed non-sedated FB 3D stack-of-radial MRI technique (FB radial) produced high quality images and accurate, repeatable hepatic fat content quantification with increased volumetric coverage[181]. This FB radial MRI technique may be a promising method to quantify body composition and ectopic fat content in infants who are incapable of breath-holding. Hence, this study's purpose was to 1) compare the image quality of FB radial MRI technique[149] to conventional Cartesian MRI and 2) evaluate the feasibility of using the FB radial MRI technique[149] for body composition and hepatic fat quantification in infants.

5.2 Methods

5.2.1 Infant Study Population

This study was approved by our institutional review board. Parents/legal guardians

provided informed consent. Healthy infants aged 1-12 months were eligible for participation. Exclusion criteria included known liver diseases, infections that affect the liver (i.e., Toxoplasmosis, Rubella, Cytomegalovirus, Human Immunodeficiency Virus, or Herpes Simplex Virus), major congenital anomalies or diseases that involve the liver, inborn errors of metabolism, and contraindications for MRI.

5.2.2 Infant Preparation and MRI Experiments

Preparation and scanning procedures were adapted from previous recommendations[177–180]. Preparation time for the MRI scan began when the infant entered the MRI suite and included feeding, swaddling, and rocking the infant until he/she became sleepy. Earplugs and earmuffs (MiniMuffs, Natus Medical Incorporated, Pleasanton, CA) were placed on the infant's ears for hearing protection. Next, infants were placed on a vacuum immobilizer on the MRI table (Med-Vac, CFI Medical, Fenton, MI, United States), and the clips on the immobilizer were fastened (Figure 5-1a). A head array coil was placed on the infant at this time (Figure 5-1b). Finally, the anterior portion of the head coil was attached. If the infant cried, the anterior portion of the head coil was removed. After all of the coils were positioned, the MRI table and the infant were advanced into the MRI bore and the total preparation time was recorded. A diagram of the infant preparation procedures is shown in Figure 5-1.

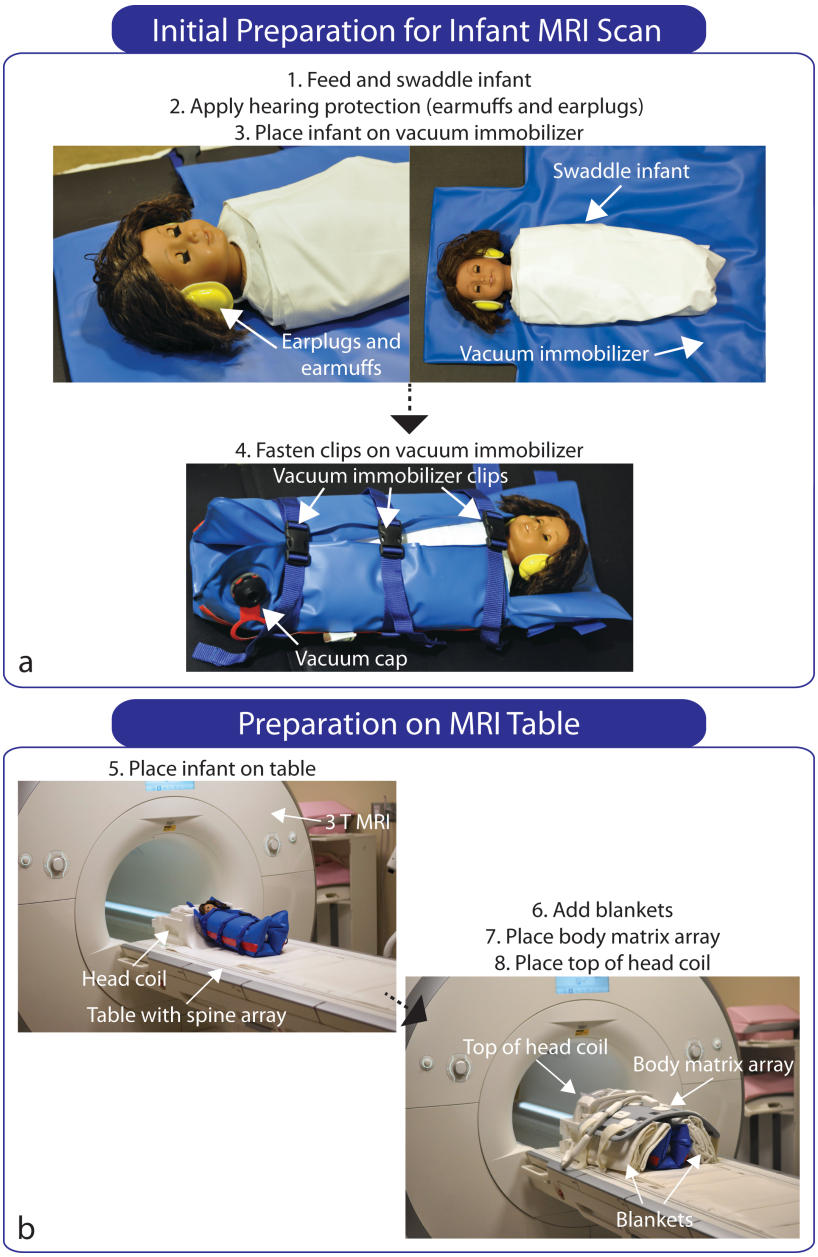

Figure 5-1 Infant MRI procedures. (a) Initial preparation for the infant scan. (b) Preparation on the MRI table.

After advancing the table and infant into the bore, the start time for the scan was recorded. If the infant cried during the first MRI scan and did not stop crying or the parent(s)/legal guardian(s) requested to stop the scan, the infant was removed from the scanner and comforted in the immobilizer. If the infant settled down, the infant was placed on the MRI table again and set-up procedures on the MRI table (Figure 5-1b) were repeated. The total scan

time was calculated after completing the MRI scan protocol.

The infant MRI experiments were performed on a 3 T scanner (MAGNETOM Skyra or Prisma, Siemens Healthineers, Erlangen, Germany) using a 20-channel head array coil, 32-channel spine array coil and 18-channel body matrix array. A FB RF-spoiled bipolar multiecho gradient-echo 3D stack-of-radial sequence with golden angle ordering[63] and gradient error and eddy current correction[149] (FB radial) (see **sections 3.2.1** and **3.2.2)** was used to acquire abdominal and head and chest scans. The 3D slabs for the head and chest scan were prescribed to overlap slightly with the abdominal scan for each infant to cover the body contiguously. FB radial abdominal scans were repeated to assess intra-session repeatability (scan 1 and scan 2). A commercially available RF-spoiled bipolar multiecho gradient 3D Cartesian sequence[56] with four-fold undersampling and controlled aliasing in parallel imaging results in higher acceleration (CAIPIRINHA)[134] reconstruction (qDixon, The Liver Lab, software version VE11, Siemens Healthineers, Erlangen, Germany) was acquired. All scans were performed without breath-holding or sedation. Imaging parameters for the FB radial and Cartesian scans are reported in Table 5-1.

Table 5-1 Imaging parameters for infant abdominal and head and chest MRI scans. All acquisitions used 20% - 25% slice oversampling. Cartesian scans were acquired without breath-holding. FB radial abdominal scans were acquired twice to assess repeatability.

Imaging Parameters	Cartesian: Abdomen	FB Radial: Abdomen	FB Radial: Head & Chest
TE (ms)	1.23, 2.46, 3.69, 4.92, 6.15, 7.38	1.23, 2.46, 3.69, 4.92, 6.15, 7.38	1.23, 2.46, 3.69, 4.92, 6.15, 7.38
ΔTE (ms)	1.23	1.23	1.23
TR (ms)	8.85	8.85	8.85
Matrix ($N_x \times N_y$)	96-128 × 96-128	96-128 × 96-128	128-160 × 128-160
Field of View ($mm_x \times mm_y$)	150-200 × 150-200	150-200 × 150-200	200-250 × 200-250
Resolution ($mm_x \times mm_y$)	1.56 × 1.56	1.56 × 1.56	1.56 × 1.56
Number of Slices	40	40-44	60-80
Slice Thickness (mm)	3	3	3
Bandwidth (Hz/pixel)	1150-1155	1150-1155	1150-1155
Flip Angle (degrees)	5	5	5
Radial Spokes	N/A	151◆-202◆	202◆-252◆
Acceleration Factor	4	1	1
Scan Time (min:s)	0:11-0:14	1:38*-2:10*	3:20**-4:43**

◆The number of spokes was adjusted to acquire fully-sampled data based on Nyquist sampling criteria (i.e. Number of Radial Spokes = $N_x \times \pi/2$). FB, free-breathing; TE, echo time; TR, repetition time.

***Includes gradient calibration acquisition time of 34-37s.**

****Includes gradient calibration acquisition time of 51s-68s.**

5.2.3 Image Reconstruction and PDFF Calculation

FB radial images and PDFF maps were generated offline in MATLAB version R2017b (MathWorks, Natwick, MA, United States). FB radial images were reconstructed fully-sampled (according to the Nyquist criteria) using gradient and eddy current correction[149] (see **sections 3.2.1** and **3.2.2**), linear density compensation, gridding, and adaptive coil combination. PDFF

maps were determined by fitting the multiple echo time images to the gradient-echo signal model with multiple fat peaks[96] to solve for the field map, single effective R_2*, water-only, and fat-only maps with complex fitting using a graph cut algorithm[34,35,132] (see **section 3.2.3**). Magnitude discrimination was used to minimize noise bias to calculate PDFF maps from the water- and fat-only images[41]. Cartesian MR images and PDFF maps were calculated on the scanner using a prototype reconstruction method with the same signal model (prototype version 963, qDixon, The Liver Lab, Software version VE11, Siemens Healthineers, Erlangen, Germany).

5.2.4 Image Quality Analysis

All reconstructed images and PDFF maps were converted to DICOM for analysis in OsiriX software version 6.0 (Pixmeo Sarl, Bernex, Switzerland). Image quality was evaluated by an experienced pediatric radiologist (S.G., > 10 years of experience) who was blinded to the trajectory (Cartesian or radial) on a scale of 1-3 for motion artifacts. The criteria for a score of 1 was non-diagnostic images with significant artifacts in the liver (i.e. bad image quality); 2 indicated minor motion artifacts in the liver; 3 indicated no motion artifacts in the liver (i.e. good image quality). The percentage of images that fell into each score category was determined.

5.2.5 Body Composition Analysis

Fat composition was defined as VAT, SAT, and BAT volumes (cm^3). Fat content was defined as the PDFF (0-100%). Body composition was measured and analyzed in Horos software version 3 (The Horos Project, horosproject.org). The VAT, SAT, and BAT were segmented using the 2D region growing segmentation and brush tools on the FB radial PDFF maps (all slices in the 3D volume). VAT was defined as adipose tissue in the intra-abdominal area[53,71]. SAT was defined as adipose tissue above the muscle fascia and below the skin in the abdomen[71].

VAT and SAT were subjectively delineated on all abdominal axial slices avoiding blood vessels, bones, intramuscular fat, and organs[53,71]. BAT was analyzed on three consecutive reformatted coronal slices of the supraclavicular region[49,50,174]. Areas of BAT were defined as any accumulation of adiposity in the supraclavicular area found in the lower neck and the axillary regions[49,50,174]. The number of slices and time to contour all the slices to determine VAT, SAT, and BAT for each subject was recorded and was reported as median ± SD. All of the segmented areas of VAT, SAT, and BAT were summed per pixel count to compute the volume and the mean PDFF. All body composition measurements were performed by the same study coordinator (K.L.) for consistency. All slices and segmentations were reviewed and validated by a pediatric radiologist (S.G., > 10 years of experience).

5.2.6 Hepatic Fat Quantification

Hepatic fat was measured on a single 15 × 15 × 15 mm^3 cubic region of interest encompassing five 3 mm slices on FB radial PDFF maps. These regions of interest were placed to avoid large blood vessels and bile ducts and in anatomically corresponding regions in the liver to reduce variations in position due to motion.

5.2.7 Statistical Analysis

Descriptive statistics were reported as median ± interquartile range and range (minimum, maximum) or percentage (number). Differences in the distribution of image quality scores between FB radial scan 1, FB radial scan 2, and Cartesian scans of the abdomen were compared using McNemar-Bowker statistical tests for dependent categorical variables in STATA software version 12 (StataCorp LLC, College Station, TX, United States). A P-value < 0.05 was considered significant. Repeatability of FB radial hepatic PDFF was assessed in MATLAB by

calculating the mean difference (MD), absolute mean difference (MD_{abs}), within-subject standard deviation (SD_{within}), and coefficient of repeatability (CR)[113,114] between repeated scans (scan 1 and scan 2) (see **section 2.10)**. FB radial VAT, SAT, BAT (volume and PDFF), and hepatic PDFF, were calculated for all subjects and reported as median ± interquartile range among subjects.

5.3 Results

5.3.1 Infant Study Population

10 infants were enrolled in the study, and 9 infants completed the entire study (90% completion rate). One infant completed only one FB radial abdominal MRI scan because of crying. Characteristics for the study population are reported in Table 5-2. For 10 infants, the median ± interquartile range and range (minimum, maximum) preparation time was 32 ± 7 min (15 min, 81 min) and scan time was 24 ± 11 min (15 min, 34 min), respectively (Table 5-3). Excluding the infant with the incomplete scan, the scan time was 24 ± 11 min (20 min, 34 min). Of the 10 subjects, 4 subjects were scanned without the anterior head coil attached.

Table 5-2 Subject Characteristics. All information are reported as median ± interquartile range and range (minimum, maximum) or percentage (number).

Characteristic	Infant Subjects (N = 10)
Age (months)	3.2 ± 3.4, (2.3, 6.9)
Sex - Male	50% (5)
Hispanic Ethnicity	30% (3)
Race - **White** **Asian** **More Than One Race**	 70% (7) 10% (1) 20% (2)
Weight (kg)	7.0 ± 1.6 (3.7, 9.9)
Height (cm)	59.6 ± 7.9 (49.5, 69.9)

Table 5-3 Subject characteristics and procedure times reported as median ± interquartile range and range (minimum, maximum) for 10 infants.

Subject	Preparation Time (min)	Scan Time (min)
1	26	20
2	15	21
3	34	24
4	33	24
5	30	33
6	30	27
7	47[a]	20
8	27[a]	32
9	35	15[b]
10	81	34
Median	31.5 ± 7.0	24.0 ± 10.5[c]
Range	(15, 81)	(15[b], 34)[c]

[a]**Preparation of subject 8 was done during the scan of subject 7.**

[b]**Incomplete scan.**

[c]**The scan time excluding subject 9 with the incomplete scan was 24.0 ± 11.0 (20, 34).**

5.3.2 Infant Image Quality

Representative axial and coronal reformat images of the liver with image quality scores ranging from 1-3 are shown in Figure 5-2. FB radial abdominal images demonstrated higher image quality scores than Cartesian abdominal images (P = 0.011). Compared to FB radial scan 1, FB radial scan 2 showed a higher proportion of image quality scores of 3 (89% vs. 30%, P = 0.025). A summary of the proportion of FB radial (scan 1 and scan 2) and Cartesian images receiving each score is shown in Table 5-4. 100% of Cartesian abdominal images received non-diagnostic image quality scores of 1 due to severe motion aliasing artifacts. In contrast, 0% of FB radial (scan 1 and scan 2) abdominal images received image quality scores of 1. FB radial had minor motion artifacts that affected the liver less (image quality score of 2) or no motion artifacts that affected the liver (image quality score of 3).

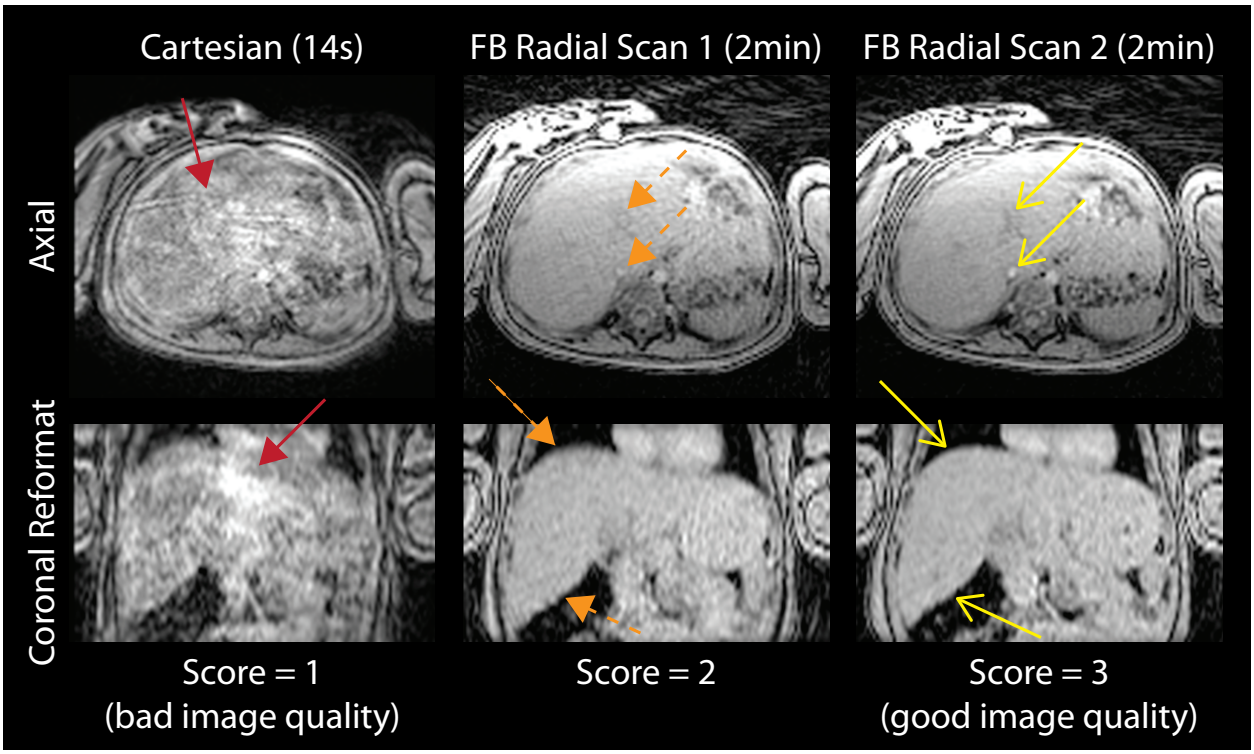

Figure 5-2 Representative Cartesian and free-breathing (FB) radial infant abdominal MR images from subject 3. This infant was female and 6.4 months of age. These examples have image quality scores of 1-3. 1 represents non-diagnostic images (i.e. bad image quality), 2 represents diagnostic images with minor motion artifacts in the liver, and 3 represents diagnostic images with no motion artifacts in the liver. Red filled-in arrowheads point to severe motion artifacts; orange filled-in arrowheads with dashed lines point to small structures with minor motion blurring on FB radial resulting in a image quality score of 2; yellow open arrowheads point to small structures that appear sharp resulting in an image quality score of 3.

Table 5-4 Summary of the image quality scores. Infant free-breathing (FB) abdominal MR images were scored for motion artifacts by an experienced radiologist using axial and coronal reformatted source images at the first echo time (TE = 1.23ms). FB radial scans (scan 1 and scan 2) were scored separately.

Score	FB Radial Scan 1*# (N = 10)	FB Radial Scan 2*# (N = 9)	Cartesian* (N = 9)
1 (bad)	0.0%	0.0%	100.0%
2	70.0%	11.1%	0.0%
3 (good)	30.0%	88.9%	0.0%

***Statistically significant differences (P = 0.011) in the distribution of image quality scores between Cartesian and FB radial scan 1 and scan 2.**

#Statistically significant differences (P = 0.025) in the distribution of image quality scores between FB radial scan 1 and scan 2.

5.3.3 Body Composition Analysis and Hepatic PDFF Quantification

VAT, SAT and BAT (volume and PDFF) and hepatic PDFF for all infants are listed in Table 5-5. The median ± SD (min, max) number of slices used to contour SAT and VAT was 40 ± 3.2 (32, 44) and in all subjects 3 slices were used to contour BAT. The median ± SD (min, max) time to contour VAT, SAT and BAT was 92 ± 37 min (42, 146) min, 20 ± 6 min (10, 30) min, and 38 ± 11 min (32, 70) min, respectively. PDFF maps from the infant with the lowest VAT, VAT-PDFF, SAT, SAT-PDFF, BAT and BAT-PDFF are shown in Figure 5-3. This was a 2.5 month old preterm infant born with intrauterine growth restriction. The hepatic PDFF for this infant (3.8%) was close to the median hepatic PDFF (3.4%). In contrast, PDFF maps from the infant with the highest hepatic PDFF are shown in Figure 5-4. This 3.2 month-old infant had a family history notable for non-alcoholic fatty liver disease. Hepatic PDFF quantification using FB radial abdominal scans demonstrated repeatability with MD = 0.22%, MD_{abs} = 0.55%, SD = 0.66%, and CR = 1.84%.

Table 5-5 Infant hepatic fat and body composition measurements. The FB radial visceral adipose tissue (VAT) volume (cm^3), VAT proton-density fat fraction (PDFF) (%), subcutaneous adipose tissue (SAT) volume (cm^3), SAT-PDFF (%), brown adipose tissue (BAT) volume (cm^3), BAT-PDFF (%), and hepatic PDFF (%), calculated as the average of FB radial scan 1 and scan 2, measurements for the 10 infant subjects. Median ± interquartile range among subjects are reported. N/A, not available.

Subject	VAT (cm^3)	VAT-PDFF (%)	SAT (cm^3)	SAT-PDFF (%)	BAT (cm^3)	BAT-PDFF (%)	Hepatic PDFF (%) (Scan 1, Scan 2)
1	36.0	39.9	385.9	89.6	1.0	26.1	4.0 (3.7, 4.3)
2	63.5	39.7	254.4	86.3	2.2	36.4	6.0 (5.9, 6.1)
3	48.2	43.9	324.6	88.2	2.4	44.2	2.4 (2.4, 2.3)
4	53.4	43.9	278.5	87.8	1.0	25.7	2.2 (2.7, 1.6)
5	61.6	40.5	256.8	85.1	1.5	22.0	2.8 (2.4, 3.3)
6	50.6	44.8	162.0	79.6	1.4	28.2	2.9 (2.4, 3.4)
7	17.0	34.2	148.4	77.8	0.7	17.3	3.8 (3.9, 3.7)
8	28.3	46.5	177.3	83.6	1.0	22.0	4.3 (4.0, 4.6)
9	69.8	37.7	469.6	90.2	N/A	N/A	3.5 (3.5, N/A)
10	53.8	44.7	358.2	93.0	1.8	37.7	3.3 (3.2, 3.4)
Median	52.0 ± 20.7	42.2 ± 4.7	267.7 ± 153.2	87.1 ± 5.3	1.4 ± 0.7	26.1 ± 14.4	3.4 ± 1.1
Range	(17.0, 69.8)	(34.2, 46.5)	(162.0, 469.6)	(77.8, 93.0)	(0.7, 2.4)	(17.3, 44.2)	(2.2, 6.0)

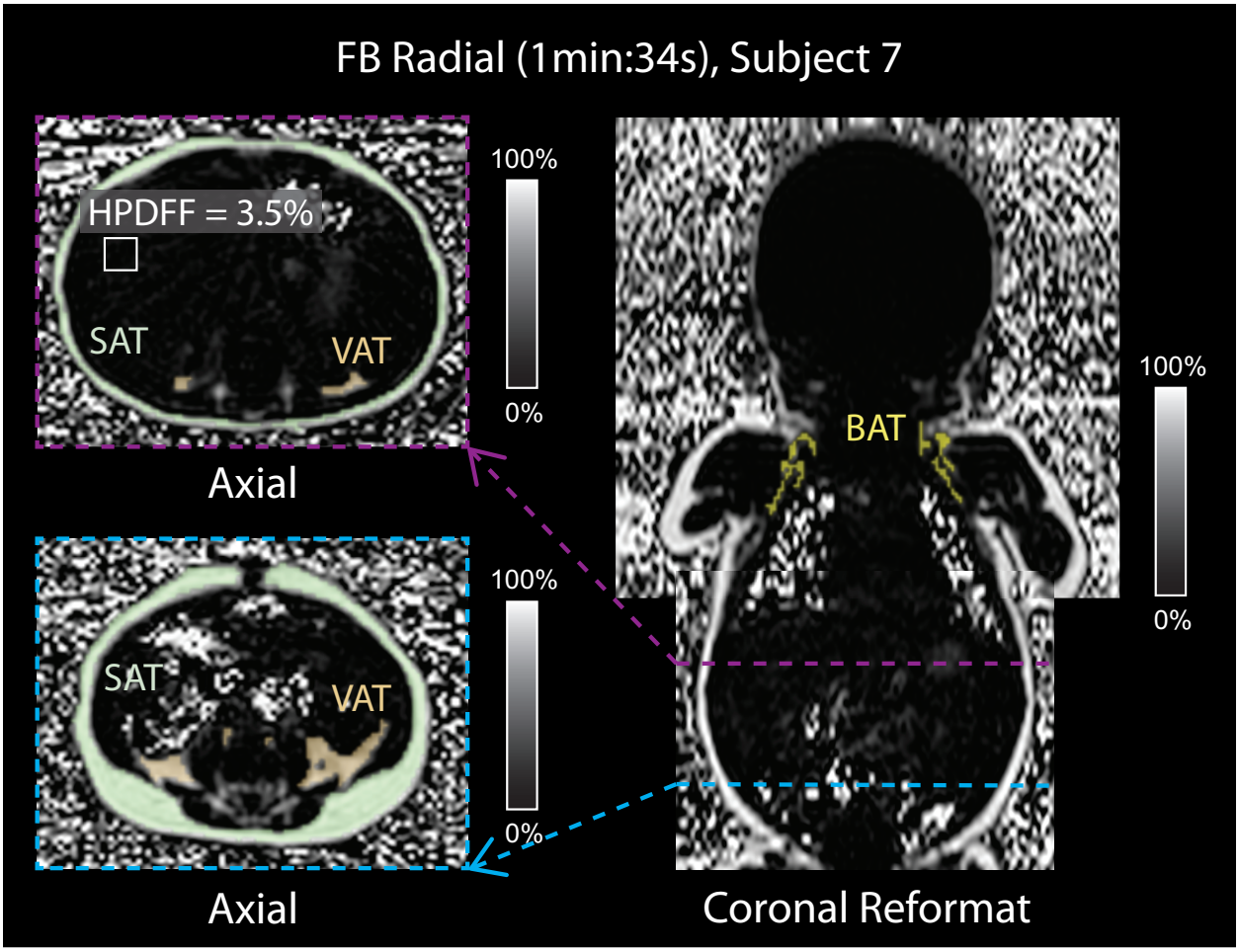

Figure 5-3 Representative infant abdominal and head and chest proton-density fat fraction (PDFF) maps (range: 0-100%) from subject 7. Abdominal images are shown in axial, and coronal reformat orientations and head and chest PDFF map in the coronal reformatted orientation from the subject with the lowest visceral adipose tissue (VAT) volume, VAT-PDFF, subcutaneous adipose tissue (SAT) volume, SAT-PDFF, brown adipose tissue (BAT) volume, and BAT-PDFF. The coronal reformat image was combined from the slabs from the abdomen scan and the head and chest scan. Hepatic PDFF (HPDFF) in the liver is shown in a representative region of interest. VAT and SAT fat compartments are contoured on axial abdominal images. The BAT fat compartment is contoured on head and chest coronal reformatted images. This male infant was 2.5 months of age and born preterm with intrauterine growth restriction. For this subject, VAT = 17.0 cm^3, VAT-PDFF = 34.2%, SAT = 148.4 cm^3, SAT-PDFF = 77.8%, BAT = 0.7 cm^3, and BAT-PDFF = 17.3%.

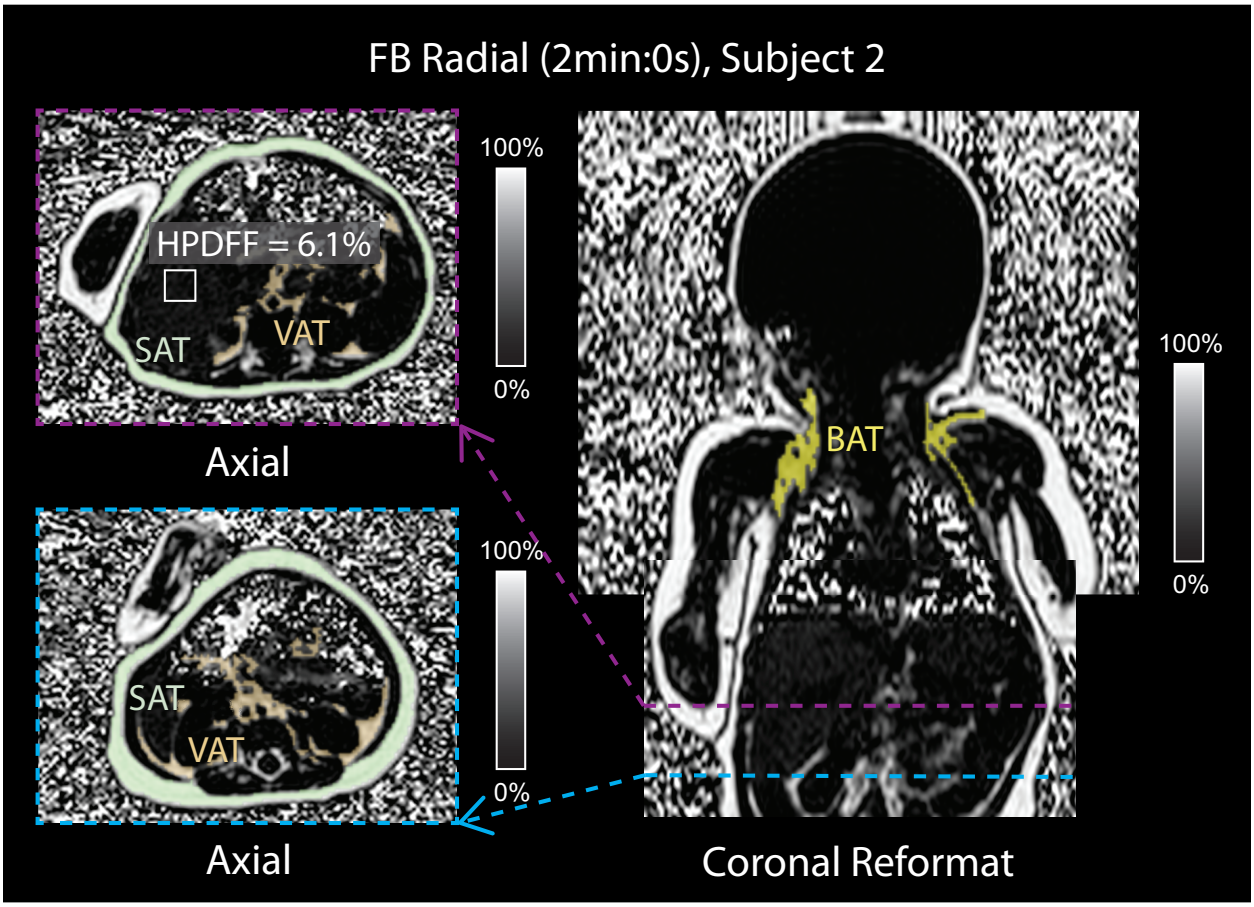

Figure 5-4 Representative infant abdominal and head and chest proton-density fat fraction (PDFF) maps (range: 0-100%) from subject 2. Abdominal images are shown in axial, and coronal reformat orientations and head and chest PDFF map in the coronal reformatted orientation from the subject with the highest hepatic PDFF (HPDFF), second highest visceral adipose tissue (VAT) volume, second highest brown adipose tissue (BAT) volume, and third highest BAT-PDFF. The coronal reformat image was combined from the slabs from the abdomen scan and the head and chest scan. HPDFF in the liver is shown in a representative region of interest. VAT and subcutaneous adipose tissue (SAT) fat compartments are contoured on axial abdominal images. The BAT fat compartment is contoured on head and chest coronal reformatted images. This male infant was 3.2 months of age, born full term, and had a family history of non-alcoholic fatty liver disease. For this subject, VAT = 63.5 cm^3, VAT-PDFF = 39.7%, SAT = 254.4 cm^3, SAT-PDFF = 86.3%, BAT = 2.2 cm^3, BAT-PDFF = 36.4%.

5.4 Discussion

In this study, quantification of body composition and hepatic fat in infants was feasible using non-sedated FB radial MRI. Moreover, FB radial had higher image quality in the liver compared to Cartesian MRI. FB radial quantification of hepatic PDFF also demonstrated repeatability with CR < 2%.

For all subjects in our study population, the preparation time was approximately 30 min and scan time was approximately 25 min. The scan times in this study included the acquisition of two FB radial abdominal scans, a FB radial head and chest scan, and an additional Cartesian abdominal scan. For the infant with an incomplete MRI, only one single FB radial abdominal scan was acquired and the scan time was 15 min. In this study, all of the FB radial abdominal and head and chest scans were acquired with oversampling to ensure enough data was collected during the MRI exam. Therefore, the scan time reported in this study was longer than if the data was acquired prospectively as fully-sampled. If only a single fully-sampled FB radial abdominal scan is acquired, the scan time for the MRI exam potentially could be reduced to 15 minutes. FB radial imaging did not require sedation or anesthesia thereby eliminating additional cost and time and potential complications. Considering the image quality and scan time, FB radial MRI could be a practical research and clinical tool in infants.

Among 10 infants, the median (± interquartile range) hepatic PDFF was 3.4% ± 1.1%. One infant's hepatic PDFF was > 5.6%, and his/her VAT and BAT volumes and BAT-PDFF were among the highest compared to other infants. This infant's family history was notable for non-alcoholic fatty liver disease and maternal history of insulin resistance. Infants of diabetic mothers are at increased risk for metabolic syndrome[182,183]. Previous studies reported significant differences in hepatic PDFF between infants born to mothers with gestational diabetes versus infants born to mothers without gestational diabetes, and hepatic PDFF positively correlated with maternal body mass index[170,171]. The results using our new FB radial technique are consistent with previously reported hepatic PDFF values in infants[170,171]. We speculate that hepatic PDFF in infants may be an early indicator for later metabolic syndrome.

The characterization of WAT, especially VAT and BAT are important for improving the understanding and management of metabolic syndrome, a collection of symptoms that include insulin resistance, dyslipidemia, hypertension, and non-alcoholic fatty liver disease[50,51,167,168,170,172,174]. Excessive WAT in infancy is linked to later onset of metabolic syndrome[167,170,172]. Beyond the newborn period, larger volumes of BAT in infants, children, and young adults is associated with a decreased risk of metabolic syndrome[167,174]. Furthermore, it has been speculated that lower BAT fat content (PDFF) in infants and children may be associated with decreased risk for metabolic syndrome later in life[50,51,168]. In our study, an infant who was born preterm with intrauterine growth restriction had the lowest VAT, SAT, and BAT (volume and PDFF) compared to the other infants. Combined with VAT, SAT, and BAT fat compartment volume and PDFF, measuring lean body mass may provide complementary information to assess the risk of future metabolic syndrome. Increased insulin production and decreased insulin sensitivity and lean body mass has been observed for infants born preterm, small or large for gestational age, or with intrauterine growth restriction, which can increase the risk of future metabolic syndrome[184–187]. When these metabolic perturbations are combined with rapid weight gain in early childhood, these infants are at increased risk for later childhood or adult-onset metabolic syndrome[187–189]. Additional work is needed to decipher the relationship between maternal, fetal, and neonatal body composition (volume and content) and hepatic PDFF with the onset and well-known risk factors for metabolic syndrome.

There have been previous studies investigating body composition in fetus cadavers, the gold standard for body composition[19,190]. However, these methods are time consuming and complex, and data on infants and children are limited[19]. Recent studies have utilized MRI to investigate body composition in fetuses[191,192] and infants[2,49–53,71,169–175]. These studies typically

used turbo spin echo or spin echo T_1-weighted imaging for body composition analysis. Although T_1-weighted, T_2-weighted, and T_2*-weighted imaging provide anatomical images for contouring fat compartments based on signal intensity differences, these techniques do not provide quantitative PDFF maps. Therefore, they may have limitations for measuring fat volume and cannot quantify fat content.

Previous studies in newborns with a mean age < 2 weeks observed abdominal VAT ranging from 11 cm^3 to 44 cm^3, and SAT ranging from 50 cm^3 to 159 cm^3 [170,172,173]. Compared to our results, VAT and SAT volumes observed in these newborn studies were lower than the volumes observed in our study (median VAT = 52.0 cm^3, median SAT = 267.7 cm^3), most likely reflecting age differences. Other studies in infants with a mean age of approximately 2 months reported total body VAT and SAT measurements. Hence, VAT and SAT volumes observed in these studies were higher than the values we obtained because these volumes were measured from total body fat rather than abdominal fat alone[193].

Two-echo and six-echo Cartesian CSE-MRI techniques have been used to quantify fat content[49–53]. Two-echo techniques do not correct for confounding factors, such as the multi-peak spectrum of fat, and may underestimate PDFF[193]. On the other hand, six-echo techniques correct for confounding factors, including the multi-peak spectrum of fat[193]. BAT-PDFF and SAT-PDFF reported in our study were similar to studies in infants with a mean age of 1-2 months[49–51]. Of these studies, two studies used a two-echo CSE-MRI technique[49,50] and did not correct for confounding factors which may underestimate PDFF[193]. Our study, along with another study[51], used a six-echo CSE-MRI technique which corrects for confounding factors. Determining fat content for body composition by accurate quantification of PDFF may be clinically relevant. Evidence suggests that a lower BAT-PDFF during infancy is associated with a lower risk of

metabolic syndrome[51,168]. Lower PDFF may be associated with increased metabolism of fat to produce heat, a process known as non-shivering thermogenesis that is important for the prevention of hypothermia[50,51,167,168]. Fat with a higher PDFF may function more like WAT, while fat with a lower PDFF may function more like BAT[50,51,168]. Our PDFF results corroborate these statements; in our study median VAT-PDFF was higher than median BAT-PDFF (42.2% versus 26.1%).

Compared to FB radial scan 1, FB radial scan 2 showed a higher proportion of image quality scores of 3 (89% vs. 30%, P = 0.025). These differences may be due to more motion, irregular breathing, or heavy breathing during FB radial scan 1 compared to scan 2. FB radial was typically performed first during the MRI exam. At the beginning of the scan, we observed that infants were often startled and cried. We believe this is most likely secondary to the noises generated by the MRI. Soon after, infants usually stopped crying, fell asleep, and moved less as the exam progressed. Hence, during FB radial scan 2, infants may have fallen into a deeper sleep and moved less compared to FB radial scan 1. In this study, no self-navigation, respiratory gating, or motion compensation was performed. FB radial may be used to generate a self-navigation signal, which may be incorporated in future work to further improve image quality[98,99,194].

The practicality of MRI for infant scanning should be considered. First, MRI is expensive compared to other imaging modalities. This may limit access to infant MRI for research purposes or specific clinical scenarios. Second, MRI is loud due to rapidly changing gradients[195]. To reduce noise and avoid hearing damage during the MRI exam, earplugs and earmuffs are required. Third, MRI can produce heating, characterized in terms of the specific absorption rate, in the subject[195]. To reduce the specific absorption rate, a low flip angle of 5 degrees was used

for the FB radial and Cartesian acquisitions to produce a low whole body specific absorption rate of 0.08-0.10 W/kg and B_{1+rms} of 0.6 μT.

This study has limitations. First, the sample size was small and the range of hepatic PDFF in this population was narrow. Larger sample sizes with a wider range of hepatic PDFF and longitudinal studies are needed to elucidate associations between hepatic PDFF, VAT, SAT, and BAT (volume and PDFF) with risk factors for later metabolic syndrome. Second, we did not compare our hepatic fat results to the gold standard, liver biopsy or breath-held Cartesian scan. Performing a liver biopsy for research purposes in healthy infants would be unethical. Breath-held MRI scans were not possible in this study because infants cannot voluntarily perform a breath-hold and sedation was not used. However, we assessed the repeatability of FB radial for hepatic fat quantification and our technique demonstrated repeatability with CR < 2%. Third, repeatability was not analyzed for abdominal body composition due to the lengthy analysis time. Head and chest scans were not repeated due to scan time considerations. However, all of our measurements were consistently performed by one coordinator and verified by a radiologist. Fourth, preparation for infant MRI can be time consuming and requires staff training and parental education. We demonstrated that with training the median preparation time and scan time for an infant MRI exam was approximately 32 and 24 minutes, respectively. Finally, this study required the infant to be asleep and/or calm during the MRI exam. If the infant began to cry during the MRI exam, the exam may be incomplete. While our new FB radial technique is robust to breathing motion, additional corrections may be needed for severe motion. To improve the motion robustness of our FB radial technique, motion tracking using a self-navigation signal may be used to characterize and compensate for severe motion[98,99,194].

5.5 Conclusion

In conclusion, non-sedated free-breathing quantification of infant body composition and hepatic fat is feasible using a FB radial MRI technique within a median scan time of 24 minutes and may be reduced to within 15 minutes if only a single FB radial abdominal scan is required. FB radial demonstrated improved image quality compared to conventional Cartesian MRI and quantified hepatic PDFF with repeatability of MD < 0.25% and CR < 2%. The new FB radial technique may help unravel the early origins of metabolic diseases by providing accurate and detailed information about body composition and hepatic fat in infants.

This work is under review:

Armstrong T, Ly KV, Ghahremani S, Calkins KL, Wu HH. Free-breathing 3D quantification of infant body composition and hepatic fat using a stack-of-radial MRI technique. Pediatric Radiology. *(Under Review)*

6 FREE-BREATHING RADIAL MRI QUANTIFICATION OF PLACENTAL R_2*

6.1 Introduction

Preeclampsia, intrauterine growth restriction (IUGR), and placenta abruption are obstetrical conditions that account for 53% of all medically indicated preterm births less than 35 weeks in the United States[22,23,26,27]. Collectively, these outcomes are referred to as ischemic placental disease (IPD) and are associated with abnormal placental vascular development, resulting in malperfusion and hypoxia[22–26]. Since preterm deliveries due to IPD contribute to higher rates of infant and maternal morbidity and mortality[23], development of accurate methods to predict or detect IPD early in pregnancy would be of great importance to enable prevention strategies and improve outcomes[26].

There are non-invasive methods for assessing placental complications, such as uterine artery (UA) Doppler[26]; however, UA Doppler has low sensitivity for the detection of IPD[26,28],

particularly during early gestation and for low risk pregnancies[26,29]. Furthermore, UA Doppler has inter-operator dependencies resulting in inter-operator bias[26].

A promising non-invasive alternative for detecting IPD conditions is magnetic resonance imaging (MRI). MRI can be used to characterize oxygenation in the placenta through quantification of the transverse relaxation rate ($R_2^* = 1/T_2^*$)[30–33]. R_2^* is known to increase due to local field inhomogeneities caused by deoxyhemoglobin, the form of hemoglobin without oxygen. Thus, R_2^* is higher (or T_2^* is lower) in hypoxic tissues than in normoxic tissues[30–33]. Despite the potential of MRI as a diagnostic tool to detect IPD via R_2^* mapping, there is limited understanding of the range of placental R_2^* across gestational age (GA), within the structure of the placenta, and among normal and abnormal pregnancies.

Previous investigations of R_2^* mapping in the placenta have been performed typically at later GAs from 20-40 weeks using a two-dimensional breath-hold (BH) Cartesian R_2^* mapping technique[30–32]; with only one very recent study including earlier GAs of 16-40 weeks[33]. If IPD is detected at later GA, intervention may not be possible or may have limited effectiveness[26]. In addition, most investigations of R_2^* or T_2^* mapping in the placenta were performed using 1.5 T MRI[30–33]. Some of these studies showed a significant decrease in nominal placental T_2^* as GA increased[30,31,33] but in one study quantifying R_2^*, this trend was not significant[32]. Compared to 1.5 T, 3 T MRI may provide higher sensitivity to changes in R_2^* for detecting IPD. However, to date, there have been limited studies reporting placental R_2^* at 3 T[67]. Therefore, additional studies are needed to determine the range of placental R_2^* for normal and abnormal pregnancies due to IPD at 3 T.

There is evidence of differences in the proportion of abnormal outcomes between anterior and posterior placenta implantation positions. Previous research has shown a higher prevalence

of IUGR and placental abruption for anterior placentas compared to posterior placentas[196]. For this reason, R_2* characteristics for normal and abnormal pregnancies may differ depending on placenta implantation position. Currently, there is no research reporting the normal or abnormal R_2* separately for anterior versus posterior placentas.

Together with expanding the knowledge of placental R_2*, further work is needed to overcome the technical challenges involved in R_2* mapping in the placenta. In particular, MRI of the placenta can be complicated by both maternal and fetal motion[32,33,197,198] and the irregular position and shape of the placenta among subjects. A major limitation of previous studies is that they used conventional MRI R_2* mapping techniques based on 2D Cartesian sampling, which is sensitive to motion-induced coherent aliasing artifacts (see **section 2.6**). To reduce motion artifacts, scans are acquired during a BH to obtain a single slice[30–33]. However, in pregnant patients, involuntary motion can occur during the scan, such as uterine contractions and fetal motion[32,33,197,198]. In addition, a BH may not be possible for all patients, such as sick or mentally impaired patients. Even for patients that can perform a BH, requiring a BH may reduce patient comfort during the scan. Due to the limited acquisition time available during a BH (typically 10-20 sec), the spatial coverage, spatial resolution, and image signal to noise ratio (SNR) may be reduced. Finally, placentas can have a range of implantation locations and geometry. Therefore, a free-breathing 3D technique may allow for improved detection of hypoxia throughout the placenta.

Non-Cartesian trajectories, such as 3D stack-of-radial trajectories, have inherent robustness to motion[61,62,149], potentially allowing for free-breathing (FB) R_2* mapping throughout the entire placenta[67] (see **section 2.7**). There have been a few studies performing R_2* mapping using stack-of-radial trajectories in the liver[165,166,199–201]. Improved image quality using

a FB stack-of-radial technique was previously observed for hepatic R_2* mapping compared to conventional BH Cartesian techniques in a population who could not perform a breath-hold[166]. One challenge to utilizing non-Cartesian stack-of-radial sampling is its sensitivity to gradient errors[60]. To overcome this, a FB 3D stack-of-radial technique with gradient error calibration and correction was recently developed for abdominal imaging[149].

In this study we propose to evaluate the accuracy and repeatability of a FB radial technique for quantitative R_2* mapping of the placenta in healthy pregnant subjects and abnormal pregnancies due to IPD at early gestation and report R_2* mapping findings at 3T MRI.

6.2 Methods

6.2.1 In Vivo Placenta Study Population

In this IRB-approved study, thirty-three pregnant subjects were recruited and informed consent was obtained. Inclusion criteria were: 18 years of age or older, planning to deliver at a hospital at our institution, carrying a viable pregnancy, not carrying a multifetal gestation pregnancy, absence of known fetal chromosomal or structural abnormalities, no contraindications to MRI, ability to provide consent, and availability for MRI scans during early gestation at two time points: 1. between 14-18 weeks and 2. between 19-24 weeks gestational age (GA). A summary of the study population's clinical characteristics is shown in Table 6-1. A premature or preterm delivery was defined as a liveborn or stillborn infant for any cause between 20 to 37 weeks' gestation[202]. Pregnancies were classified as abnormal due to IPD if a subject displayed at least one of three IPD conditions (preeclampsia, placental abruption, or IUGR) at delivery (i.e., IPD subjects). Preeclampsia was defined as systolic blood pressure of 140 mm Hg or higher, or diastolic pressure of 90 mm Hg or higher on two occasions at least 4 hours apart

after 20 weeks of gestation in a woman with a previously normal blood pressure and proteinuria of 300 mg or more in 24 hours[203]. In the absence of proteinuria, preeclampsia was defined as new onset hypertension with new onset of thrombocytopenia, renal insufficiency (serum creatinine greater than 1.1 mg/dL), impaired liver function (elevated liver transaminases to twice normal concentration), pulmonary edema, or cerebral or visual symptoms[203]. Placental abruption was defined as separation of the placenta from the inner wall of the uterus prior to delivery[204]. IUGR infants were defined at delivery as birth weight of less than the 10th percentile as expected for corresponding GA. All other subjects were analyzed as subjects with normal pregnancies (i.e., normal subjects). The normal subjects were also divided into subjects with anterior placental implantation positions (i.e., anterior placenta) and posterior placental implantation positions (i.e., posterior placenta) for separate analysis.

Table 6-1 Summary of the characteristics for the subjects with normal pregnancies and the subjects with abnormal pregnancies due to ischemic placental disease (IPD).

Maternal Characteristics	Normal Subjects (N = 30)	IPD Subjects (N = 3)
Age at 14-18 Week MRI (Years)	34.31 ± 3.96	33.34 ± 6.05
Body Mass Index (BMI) (kg/m^2)	23.94 ± 4.13	21.73 ± 2.53
BMI Status:		
Underweight	2 (6.7%)	0 (0.0%)
Normal Weight	18 (60.0%)	3 (100.0%)
Overweight	7 (23.3%)	0 (0.0%)
Obese	3 (10.0%)	0 (0.0%)
GA at Delivery (Weeks)	39.43 ± 1.08	39.33 ± 1.44
Delivery Outcome:		
Term	30 (100.0%)	3 (100.0%)
Premature	0 (0.0%)	0 (0.0%)
Delivery Type:		
C-Section	8 (26.7%)	1 (33.3%)
Vaginal Spontaneous	20 (66.7%)	2 (66.7%)
Vaginal Extractor Vacuum	2 (6.7%)	0 (0.0%)
Weight Gain During Pregnancy (lbs)[1]	31.64 ± 12.51	25.57 ± 4.19
Infant Characteristics	**Normal Subjects (N = 30)**	**IPD Subjects (N = 3)**
Sex (Male)	17 (56.7%)	2 (66.7%)
Weight (g)	3521.53 ± 384.64	2901.67 ± 502.75
Weight Percentile	50.0% ± 20.8%	16.7% ± 15.9%
Weight Percentile Range	20% − >97%	7% − 35%
Number of Infants With Birth Weight Percentile <10th for GA	0 (0.0%)	2 (66.7%)
Length (cm)[1]	51.89 ± 2.27	46.97 ± 5.21
Length Percentile[1]	62.8% ± 26.7%	31.5% ± 40.3%
Length Percentile Range[1]	7% − >97%	<3% − 60%
Placenta Characteristics	**Normal Subjects (N = 27)[2]**	**IPD Subjects (N = 3)**
Weight (g)[3]	465.15 ± 81.26	376.73 ± 46.14
Longest Diameter (cm)	21.65 ± 3.64	20.33 ± 1.53
Umbilical Cord Length (cm)	42.99 ± 13.39	22.17 ± 7.29

[1]One normal subject did not have characteristic(s) due to delivery in another location.

[2]One normal subject did not have characteristic(s) due to delivery in another location.

[3]Three normal subjects did not have characteristic(s) due to delivery in another location or elected to keep placenta.

[4]One normal subject had incomplete placental weight due to missing part of placenta.

After delivery, thirty subjects were classified as normal subjects while three subjects were classified as abnormal subjects with IPD. One IPD subject was diagnosed with preeclampsia with severe features and two IPD subjects presented with IUGR. Baseline R_2* characteristics were calculated separately for normal subjects (all, anterior placenta, posterior placenta) and IPD subjects. Of the normal subjects, fifteen subjects had anteriorly implanted placentas while fifteen had posteriorly implanted placentas. All of the IPD subjects had anteriorly implanted placentas.

6.2.2 R_2 Mapping using 3D Stack-of-Radial MRI*

We used a previously developed multiecho gradient echo sequence based on the golden-angle-ordered 3D stack-of-radial trajectory (FB radial)[63,149] to obtain images and R_2* maps. Gradient calibration and correction was performed[149] (see **sections 3.2.1** and **3.2.2**). To reduce the scan time to approximately three minutes, all FB radial scans were acquired with two-fold undersampling, as determined by the Nyquist criteria (i.e., number of spokes for fully-sampled data = number of readout points × $\pi/2$). Previous work determined that the R_2* range in the placenta at 3 T was approximately 5 – 25 s^{-1} [67]; therefore, twelve echo times with 1.23 ms echo spacing were utilized to improve fitting for this range. For the following phantom and in vivo experiments (see **subsections: R_2* Phantom Study** and **In Vivo Placenta MRI Experiments)**, all images were acquired on a 3 T MRI scanner (Skyra or Prisma MAGNETOM, Siemens Healthineers, Erlangen, Germany) using a body matrix array and spine array coils.

6.2.3 3D Stack-of-Radial Reconstruction and R_2 Mapping*

Radial MRI reconstruction and signal model fitting were performed offline in MATLAB R2016b (MathWorks, Natwick, MA, United States) using gradient correction[149], 3D gridding, a

linear density compensation function, and adaptive coil combination[131]. R_2* was calculated using a graph cut algorithm[34,35,132] by fitting the multiple echo time images to a gradient echo signal model[36,149,205] with a seven-peak fat spectrum[96] and a single effective R_2* per voxel[34] (see **section 3.2.3)**. Cartesian multiecho images were reconstructed offline in MATLAB and R_2* mapping was performed using the same signal model and fitting algorithm that were used for the radial images. T_2 HASTE images were reconstructed by the scanner software.

6.2.4 R_2 Phantom Experiments*

A R_2* phantom with ten 50mL test tubes containing an agar gel and ferumoxytol (Feraheme, AMAG Pharmaceuticals Inc., Waltham, MA, United States) was constructed to evaluate R_2* mapping accuracy. The solution was composed of 43 mM (1.2565 g) sodium chloride, 0.043 mM (43.267 μL) gadopentetate dimeglumine (Magnevist, Bayer in Radiology, Warrendale, PA, United States), and 4 g of 3-4% high gel strength agar (Sigma-Aldrich, St. Louis, MO, United States) dissolved in 500 mL of deionized water. Varying volumes of ferumoxytol were added to each test tube to provide a R_2* range of 5 – 70 s^{-1}, emcompassing values previously observed in the placenta at 3 T[67].

The phantom was scanned in the axial orientation using the proposed radial MRI sequence and a commercially-available standard multiecho gradient echo 3D Cartesian MRI sequence (qDixon, the Liver Lab, Siemens, Erlangen, Germany) to evaluate radial R_2* mapping accuracy. A twelve-echo protocol was used for both sequences with imaging parameters matched as much as possible to enable a fair comparison (Table 6-2). The radial sequence was repeated back-to-back in the same session to assess repeatability (scan 1 and scan 2). A region of interest (ROI) was drawn in each test tube to compare R_2* mapping results between radial and Cartesian sequences.

Table 6-2 Representative sequence parameters for the in vivo placenta MRI experiments. The acquisitions were obtained in the axial orientation. A slice oversampling factor of 9.1% was used for all radial acquisitions.

Imaging Parameters	T_2 HASTE	Radial
Number of Echoes (TE)	1	12
First TE (ms)	92	1.23
ΔTE (ms)	N/A	1.23
Last TE (ms)	N/A	14.76
Echo Train Length	70	N/A
TR (ms)	3000	15.90
Matrix ($N_x \times N_y$)	272 × 512	224 × 224
Field of View ($mm_x \times mm_y$)	265 × 500	380 × 380
Resolution ($mm_x \times mm_y$)	0.974 × 0.976	1.696 × 1.696
Slice Thickness (mm)	5	4
Number of Slices	45	44
Number of Radial Spokes	N/A	176◆
Flip Angle (degrees)	150	5
Bandwidth (Hz/pixel)	390	1175
Scan Time (min:s)	2:06	3:16

◆Radial acquisitions were two-fold undersampled based on the Nyquist criteria (i.e. Number of Radial Spokes = $N_x \times \pi/2 \times 1/2$).

6.2.5 In Vivo Placenta MRI Experiments

In vivo placenta scans were acquired feet-first supine in each subject with one MRI exam during the time frame of 14-18 weeks GA and then another MRI exam during the time frame of 19-23 weeks GA. Each MRI exam consisted of the axial FB radial sequence[149] and a commercially-available axial T_2 HASTE[206] sequence. Each FB radial scan was acquired with two-fold undersampling and was repeated back-to-back in the same session to evaluate repeatability (scan 1 and scan 2). Representative imaging parameters for FB radial (3D) and T_2

HASTE scans (2D multi-slice) are shown in Table 6-2.

6.2.6 In Vivo Placenta Image Analysis

T_2 HASTE and FB radial images were converted to DICOM to be viewed and analyzed in OsiriX 6.0 (Pixmeo Sarl, Bernex, Switzerland). Axial T_2 HASTE images were registered to FB radial images using Advanced Normalization Tools (ANTs) software[207–209]. The ANTs registration was performed using 3D non-rigid registration with a mutual information metric used for template matching. Due to low placenta contrast on FB radial images, ROIs were delineated to contour the placenta on registered T_2 HASTE images for all slices. These ROIs were then applied to FB radial images and R_2* maps. An experienced abdominal radiologist (R.M., with 10 years of experience) and an experienced maternal fetal medicine specialist (C.J., with 20 years of experience), both masked to the pregnancy outcome, confirmed the ROI placement on the images and made adjustments if required. The confirmed ROIs were then used to measure the R_2* values over the entire placental volume for analysis. A diagram illustrating the registration and image analysis steps is shown in Figure 6-1.

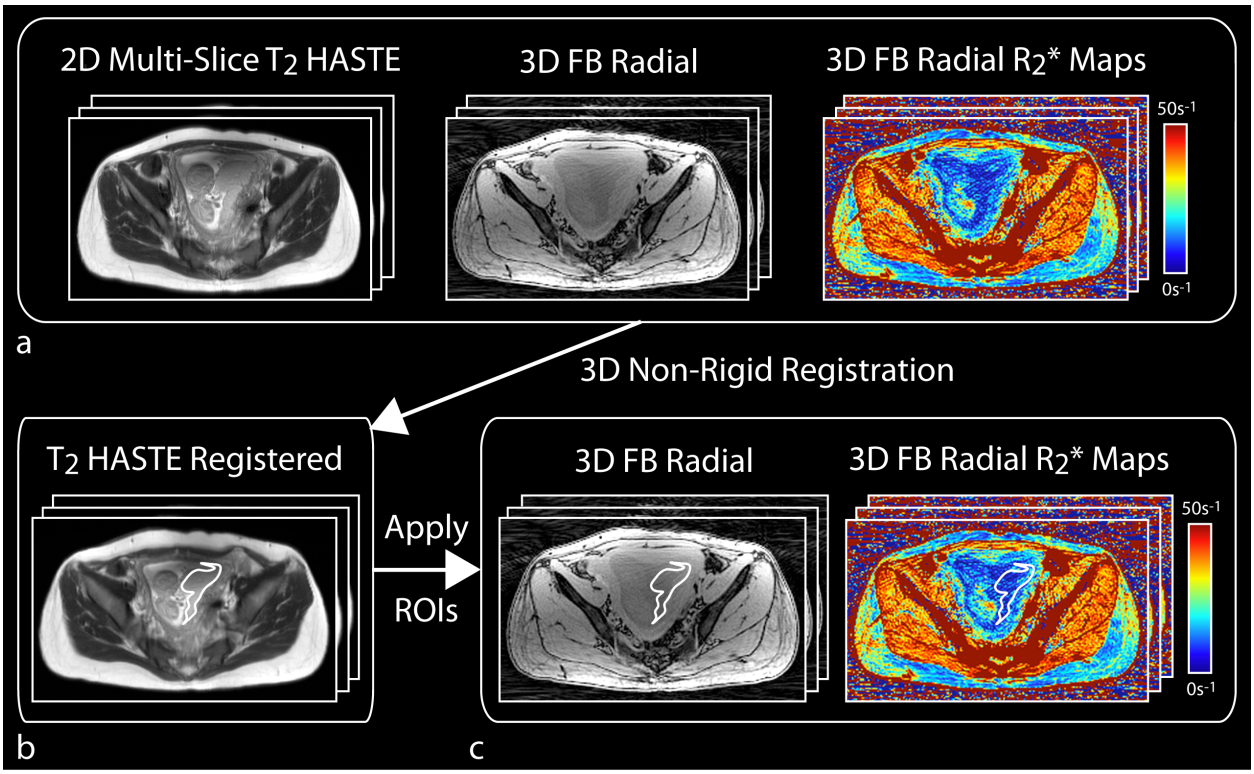

Figure 6-1 In vivo placenta MRI registration and analysis flowchart. (a) Axial 2D multi-slice T_2 HASTE images were registered using 3D non-rigid registration to the axial 3D FB radial dataset. (b) The registered T_2 HASTE images were used to aid in drawing regions of interest (ROIs) to contour the full placenta volume. (c) ROIs were then applied to the 3D FB radial images and R_2* maps, and were confirmed by an experienced radiologist and an experienced maternal fetal medicine specialist. The mean placental R_2* values were measured in the confirmed ROIs.

6.2.7 Statistical Analysis

A P-value (P) < 0.05 was considered significant for all statistical analyses. For the phantom experiments, linear correlation and Bland-Altman analysis[112] were performed between radial R_2* and Cartesian R_2* (see **section 2.9**). All correlation coefficients were tested for statistical significance. To assess repeatability for the radial technique repeatability analysis was performed between scan 1 and scan 2[113,210] (see **section 2.10)**.

Only normal subjects were used to determine baseline R_2* characteristics. The mean and range of R_2* were reported. To assess inter-subject temporal variation, slope of the mean R_2* as a function of GA (ΔR_2*), was calculated. To assess intra-subject spatial variation of R_2*, the

coefficient of variation (CV), calculated as the standard deviation divided by the mean, was determined for each GA range. With the exception of the range of placental R_2*, all baseline R_2* characteristics were reported as mean ± standard deviation.

Previous research has shown a significantly higher prevalence of IUGR and placental abruption for anterior placentas compared to posterior placentas[196]. Therefore, baseline R_2* characteristics were reported for all subjects analyzed together and then separately for two groups (anterior placentas versus posterior placentas). Statistical tests were performed to evaluate differences in mean R_2* between 14-18 weeks GA and 19-23 weeks GA, or between anterior and posterior placentas, using non-parametric Wilcoxon Signed-Rank and Wilcoxon Rank-Sum tests for dependent and independent 2-sample data, respectively. The baseline inter-subject R_2* standard deviation was tested for significance difference using Pittman's test for equality of variances and a 2-sample F-test for dependent and independent data, respectively.

For each individual IPD subject, the mean R_2*, ΔR_2*, and CV were reported. Using these values, the corresponding Z-score ($\hat{Z}$) with respect to the normal subjects was calculated as the estimate ($\overline{X}$) minus the population mean (μ) divided by the population standard deviation (σ) (i.e. $\hat{Z} = \frac{\overline{X}-\mu}{\sigma}$), similar to previous work[30].

6.3 Results

6.3.1 Accuracy and Repeatability of FB Radial R_2 Mapping*

Results from the phantom study found that R_2* measured by Cartesian and radial sequences (scan 1 and scan 2) were consistent (Figure 6-2a-b). Linear correlation analysis demonstrated a significant correlation between radial R_2* (scan 1) and Cartesian R_2* (r = 0.996,

$P < 0.001$; $\rho_c = 0.996$, $P < 0.001$), and between radial R_2* (scan 2) and Cartesian R_2* ($r = 0.998$, $P < 0.001$; $\rho_c = 0.998$, $P < 0.001$) (Figure 6-2c). Bland-Altman analysis showed a MD = -0.19 s^{-1} and LoA = [-3.93 s^{-1}, 3.56 s^{-1}] between radial R_2* (scan 1) and Cartesian R_2*, and a MD = 0.03 s^{-1} and LoA = [-2.79 s^{-1}, 2.86 s^{-1}] between radial R_2* (scan 2) and Cartesian R_2* (Figure 6-2d). The proposed radial technique demonstrated R_2* mapping repeatability between scan 1 and scan 2 with MD_{within} = 0.23 s^{-1}, MD_{abs} = 0.90 s^{-1}, SD_{within} = 1.41 s^{-1} and CR = 3.90 s^{-1}.

In normal subjects, placental R_2* measured by FB radial scan 1 and scan 2 demonstrated stronger repeatability for 14-18 weeks GA (MD_{within} = 0.32 s^{-1}, MD_{abs} = 0.84 s^{-1}, SD_{within} = 1.05 s^{-1} and CR = 2.92 s^{-1}) than for 19-23 weeks GA (MD_{within} = 0.98 s^{-1}, MD_{abs} = 1.73 s^{-1}, SD_{within} = 2.97 s^{-1} and CR = 8.24 s^{-1}). This was due to two outliers from scans in subjects with posterior placentas during 19-23 weeks GA (see **Discussion**). A summary of the in vivo placental R_2* mapping repeatability results is shown in Table 6-3.

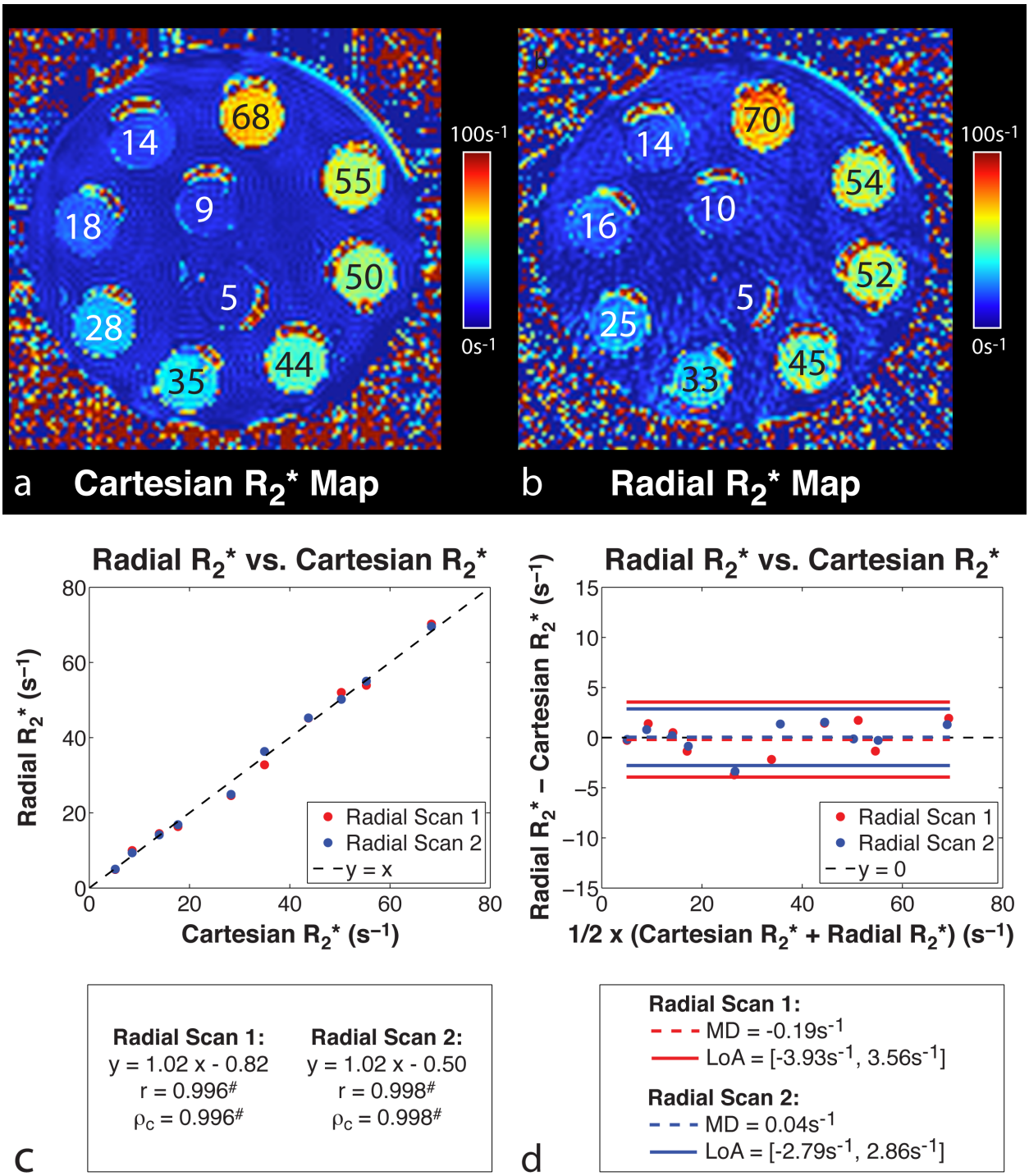

Figure 6-2 R_2* maps of the ferumoxytol phantom acquired using the (a) Cartesian and (b) radial MRI sequences at 3 T in the axial orientation. Test tubes are labeled with their corresponding R_2* values in s^{-1}. R_2* phantom (c) linear correlation and (d) Bland-Altman analysis results for radial R_2* (scan 1) vs. Cartesian R_2*, and radial R_2* (scan 2) vs. Cartesian R_2* at 3 T. #Statistically significant with $P < 0.001$.

Table 6-3 Representative sequence parameters for the in vivo placenta MRI experiments. The acquisitions were obtained in the axial orientation. A slice oversampling factor of 9.1% was used for all radial acquisitions.

	GA (Weeks)	MD_{within} (s^{-1})	MD_{abs} (s^{-1})	SD_{within} (s^{-1})	CR (s^{-1})
All Subjects (N = 30)	**14-18**	0.32	0.84	1.05	2.92
	19-23	0.98	1.73	2.97	8.24
Anterior (N = 15)	**14-18**	0.48	1.05	1.21	3.37
	19-23	0.24	1.23	1.66	4.60
Posterior (N = 15)	**14-18**	0.15	0.63	0.87	2.42
	19-23	1.73	2.23	3.79	10.50

◆**Radial acquisitions were two-fold undersampled based on the Nyquist criteria (i.e. Number of Radial Spokes = $N_x \times \pi/2 \times 1/2$).**

6.3.2 In Vivo Placenta Study: Baseline R_2 Characteristics*

In vivo placental R_2* maps were successfully obtained from normal subjects (example in Figure 6-3) and IPD subjects (example in Figure 6-4) with the FB radial technique during early gestation at 3 T. FB radial achieved full volumetric coverage of the placenta in approximately three minutes for all subjects at both time points, except for one normal subject at the second GA time point. This subject had a placenta that extended for more than 176 mm along the superior-inferior direction. Using the same parameters for FB radial as all other subjects (Table 6-2), 90% of the placenta volume was covered in this subject. Intra-subject spatial heterogeneity of R_2* in the placenta volume was seen on the axial, coronal, and sagittal R_2* maps. For all normal subjects, the inter-subject mean and range of placental R_2* values at 3 T for 14-18 weeks GA was 12.94 s^{-1} ± 2.66 s^{-1} and 7.91 s^{-1} – 20.29 s^{-1}, respectively; and 13.19 s^{-1} ± 1.87 s^{-1} and 9.64 s^{-1} – 16.88 s^{-1} for 19-23 weeks GA (Table 6-4). The mean R_2* for all subjects at 14-18 weeks and 19-13 weeks GA was not significantly different (P = 0.530). The inter-subject standard deviation (SD) of 1.87 s^{-1} was smaller for 19-23 weeks, compared to SD of 2.66 s^{-1} for 14-18 weeks,

however this difference was not significant (P = 0.070). The mean R_2^* for anterior and posterior placentas for 14-18 weeks was 12.93 s^{-1} ± 2.06 s^{-1} and 12.94 s^{-1} ± 3.22 s^{-1} (P = 0.507), both of which were similar to the mean R_2* across all subjects. The mean R_2* for anterior and posterior placentas for 19-23 weeks GA was slightly higher for anterior placentas (13.64 s^{-1} ± 1.67 s^{-1}) compared to posterior placentas (12.73 s^{-1} ± 2.01 s^{-1}), but this was not significant (P = 0.171). A summary of the baseline mean R_2* and R_2* range results are shown in Table 6-4.

The FB radial technique was able to utilize full-volume placental R_2* maps to calculate the spatial R_2* variation (CV) and temporal R_2* variation (ΔR_2*). The mean R_2* and CV were plotted as a function of the GA for all pregnant subjects (Figure 6-5). For temporal R_2* variation in normal subjects, ΔR_2* was 0.102 ± 0.728, showing a large inter-subject standard deviation. The ΔR_2* for anterior (0.191 ± 0.723) and posterior (0.013 ± 0.747) placentas were not significantly different (P = 0.125). For spatial R_2* variation in normal subjects, the CV was significantly higher for 14-18 weeks GA compared to 19-23 weeks GA with values of 0.632 ± 0.121 and 0.577 ± 0.128, respectively (P = 0.043). For anterior placentas, CV was significantly different between 14-18 weeks GA (0.587 ± 0.108) and 19-23 weeks GA (0.488 ± 0.076) (P = 0.010). For posterior placentas, CV was not significantly different between 14-18 weeks GA and 19-23 weeks GA (P = 0.804). For 14-18 weeks GA, CV was not significantly different between anterior and posterior placentas (P = 0.097). On the other hand, for 19-23 weeks, CV was significantly lower for anterior placentas (0.488 ± 0.076) compared to posterior placentas (0.666 ± 0.106) (P < 0.001). A summary of the baseline ΔR_2* and CV results is shown in Table 6-4.

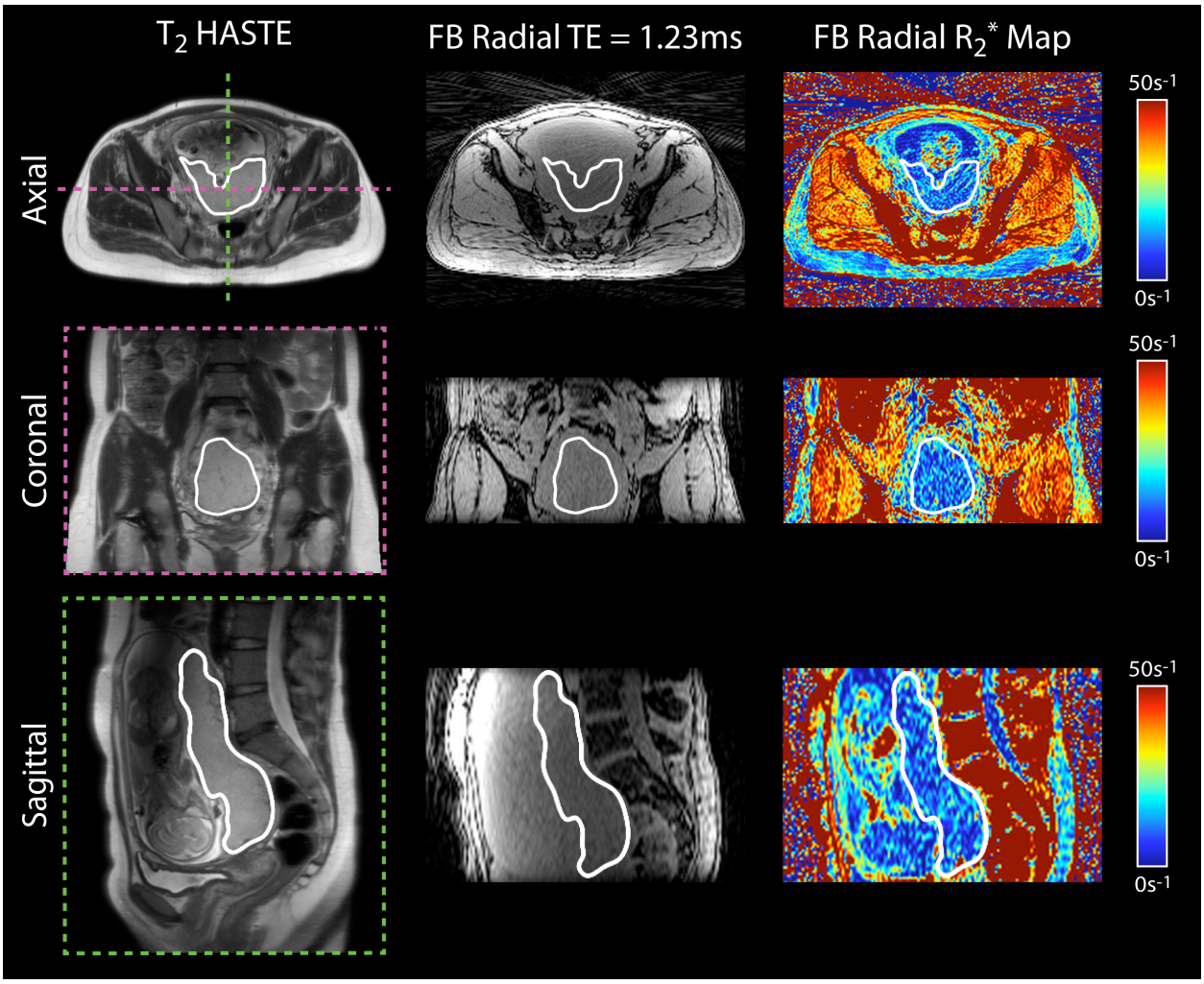

Figure 6-3 Representative in vivo placenta images and R_2* maps of a subject with normal pregnancy at 16+2 weeks gestational age acquired using free-breathing radial MRI at 3 T. Axial, coronal and sagittal views are shown. The placenta is delineated by a white contour.

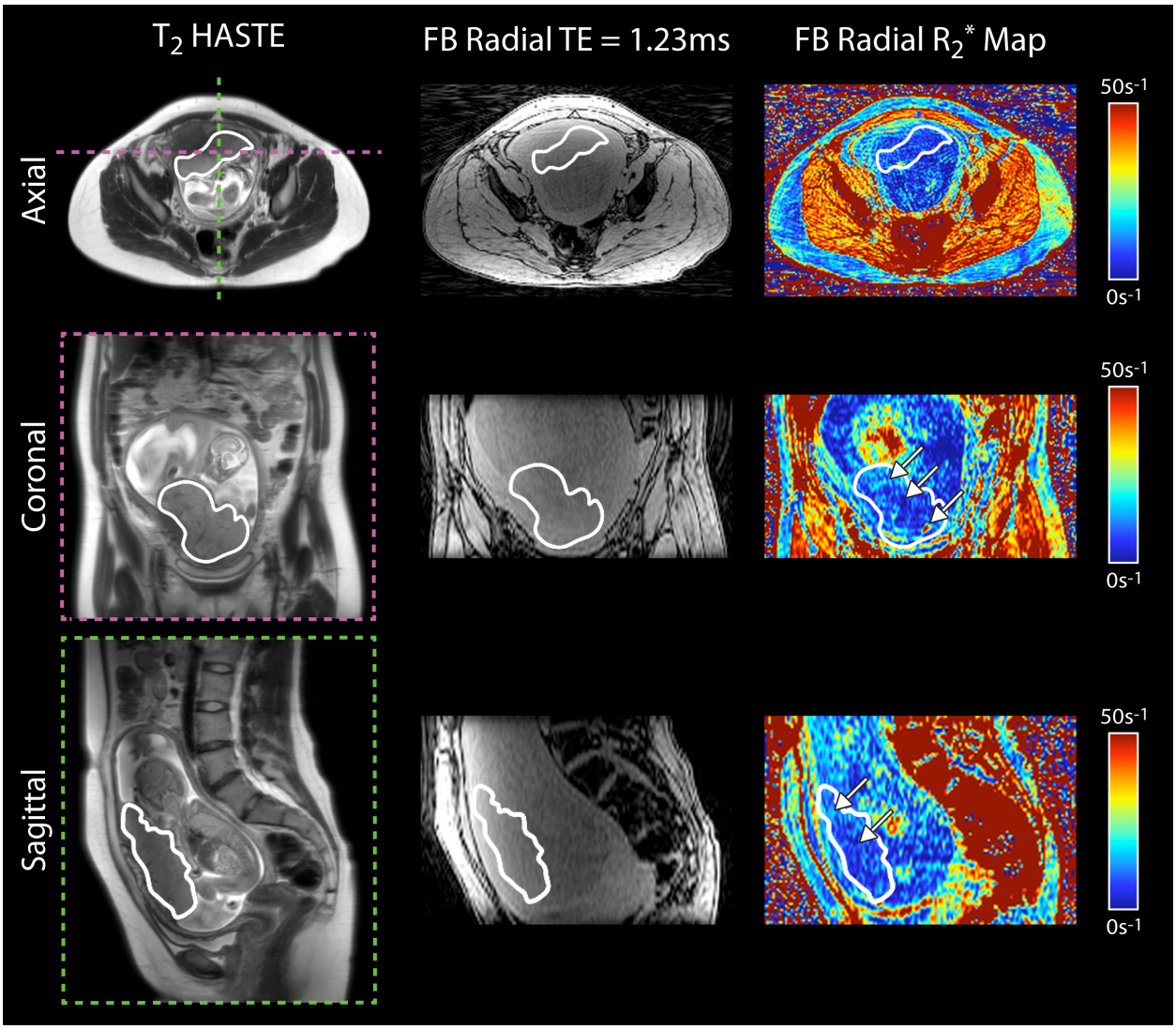

Figure 6-4 Representative in vivo placenta images and R_2* maps of a subject with preeclampsia at 19+1 weeks gestational age acquired using free-breathing radial MRI at 3 T. Axial, coronal and sagittal views are shown. The placenta is delineated by a white contour. White arrows on the R_2* maps point to spatial variation. In this subject, there were regions of higher R_2* along the periphery and regions of lower R_2* in the center of the placenta.

Table 6-4 Placental R_2* measurements in normal subjects using free-breathing radial MRI at 3 T. Mean R_2* (± standard deviation), R_2* range, and mean (± standard deviation) coefficient of variation (CV) are reported for 14-18 weeks and 19-23 weeks GA. Mean (± standard deviation) change in R_2* across gestational age (GA) (ΔR_2*) is reported. Analysis was performed for all subjects (N = 30), and again for the subjects separated into anterior (N = 15) versus posterior (N = 15) placenta implantation positions.

	GA (Weeks)	R_2* (s^{-1})	R_2* Range (s^{-1})
All Subjects (N = 30)	**14-18**	12.93 ± 2.66	7.91 – 20.29
	19-23	13.19 ± 1.87	9.64 – 16.88
Anterior (N = 15)	**14-18**	12.93 ± 2.06	8.91 – 17.33
	19-23	13.64 ± 1.67	10.80 – 16.88
Posterior (N = 15)	**14-18**	12.94 ± 3.22	7.91 – 20.29
	19-23	12.73 ± 2.01	9.64 – 16.16
	GA (Weeks)	**CV (Arbitrary Units)**	**ΔR_2* (s^{-1}/Week)**
All Subjects (N = 30)	**14-18**	0.632 ± 0.121◆	0.102 ± 0.728
	19-23	0.577 ± 0.128◆	
Anterior (N = 15)	**14-18**	0.587 ± 0.108◆	0.191 ± 0.723
	19-23	0.488 ± 0.076◆#	
Posterior (N = 15)	**14-18**	0.677 ± 0.120	0.013 ± 0.747
	19-23	0.666 ± 0.106#	

◆Statistically significant differences with P < 0.05 between 14-18 weeks and 19-23 weeks GA.

#Statistically significant differences with P < 0.001 between anterior and posterior placentas.

6.3.3 In Vivo Placenta Study: IPD Subjects

In three IPD subjects, we measured mean R_2*, ΔR_2*, and CV using FB radial during early gestation at 3 T MRI (Table 6-5). For the two IPD subjects with IUGR, mean R_2*, ΔR_2*, and CV were similar to baseline values determined in normal subjects. For the IPD subject with preeclampsia, mean R_2* was substantially lower than normal subjects with anterior placentas during 14-18 weeks GA ($\hat{Z}$ = -2,17) and during 19-23 weeks GA ($\hat{Z}$ = -2.62), respectively. Representative axial, coronal reformatted, and sagittal reformatted images of this subject with

preeclampsia are shown in Figure 6-4. Variations in R_2* between the center and the periphery of the placenta along the superior-inferior direction and hot spots with elevated R_2* were observed.

Table 6-5 Placental R_2* measurements in subjects with ischemic placental disease (IPD) using free-breathing radial MRI at 3 T. The type of IPD, placenta implantation position (anterior or posterior), mean (± standard deviation) R_2^*, and mean (± standard deviation) coefficient of variation (CV) for 14-18 weeks and 19-23 weeks gestational age (GA) are reported. Mean (± standard deviation) change in R_2* across gestational age (GA) (ΔR_2*) is reported. The Z-score ($\hat{Z}$) of each value was determined using the population mean from all normal anterior placentas (data from Table 6-4).

Subject	IPD Type, Placenta Implantation Position	GA (Weeks)	R_2* (s^{-1}) $\hat{Z}$	CV (Arbitrary Units) $\hat{Z}$	ΔR_2* (s^{-1}/Week) $\hat{Z}$
1	Preeclampsia, Anterior	14-18	**R_2* = 8.46**◆ $\hat{Z}$ = -2.17	**CV = 0.68** $\hat{Z}$ = 0.84	**ΔR_2* = 0.21** $\hat{Z}$ = 0.02
		19-23	**R_2* = 9.23**◆ $\hat{Z}$ = -2.62	**CV = 0.60** $\hat{Z}$ = 1.44	
2	IUGR, Anterior	14-18	**R_2* = 12.73** $\hat{Z}$ = -0.10	**CV = 0.55** $\hat{Z}$ = 0.34	**ΔR_2* = 0.27** $\hat{Z}$ = 0.11
		19-23	**R_2* = 14.12** $\hat{Z}$ = 0.29	**CV = 0.38** $\hat{Z}$ = -1.46	
3	IUGR, Anterior	14-18	**R_2* = 11.83** $\hat{Z}$ = -0.54	**CV = 0.70** $\hat{Z}$ = 1.02	**ΔR_2* = 0.27** $\hat{Z}$ = 0.11
		19-23	**R_2* = 13.01** $\hat{Z}$ = 0.38	**CV = 0.50** $\hat{Z}$ = 0.17	

◆ **The Z-score ($\hat{Z}$) > 1.96 or $\hat{Z}$ < -1.96 determined from each IPD subject compared to the population mean from all normal anterior placentas.**

6.4 Discussion

In this study, FB 3D stack-of-radial R_2* mapping was performed for the full placental volume in pregnant subjects during early gestation and at 3 T. FB radial demonstrated accurate and repeatable R_2* mapping in a phantom, and repeatable R_2* mapping in subjects with normal pregnancies. The R_2* findings were reported for normal subjects and subjects with IPD at 3 T. In thirty normal subjects, the baseline mean R_2*, ΔR_2*, and CV for 14-18 weeks GA and 19-23

weeks GA were measured and differences in CV were observed between anterior and posterior placentas. Additionally, mean R_2*, ΔR_2*, and CV were successfully obtained in a pilot group of three IPD subjects. Substantial differences in mean R_2* were observed between one IPD subject with preeclampsia and normal subjects. The proposed FB radial technique supports the investigation of placental hypoxia during early gestation by quantifying R_2* throughout the entire placental volume. These 3D R_2* maps can be used to investigate spatial variations in R_2* and temporal changes in R_2* as a function of GA.

With regards to mean R_2* and ΔR_2* at both GA time points, significant differences between anterior and posterior placentas were not observed. Significant differences in the spatial CV of R_2* were observed between 14-18 weeks GA and 19-23 weeks GA, for all subjects and specifically for anterior placentas. For 19-23 weeks GA, significant differences in CV were observed between anterior and posterior placentas. These observations may be due to biological differences in the vasculature between anterior and posterior placentas. However, another factor to consider is that all subjects were scanned feet-first supine in this study, which might also contribute to these observed differences between anterior and posterior placentas. Further work beyond this study may be required to investigate potential differences between anterior and posterior placentas.

This study investigated earlier GA, while previous studies investigated later GA and a wider GA range[30–33]. In some previous studies, a negative correlation between placental T_2* and GA was observed[30,33] and in one study no significant change in R_2* as a function of GA was observed[32]. However, the R_2* behavior at early gestation and 3 T has not been established. Earlier GA may have larger inter-subject R_2* variation compared to later GA due to variations in structural changes in the placenta during early gestation. Therefore, it is not clear that a linear

relationship should hold between R_2* and GA during early gestation. Future work includes performing more MRI exams per subject with a larger range of GA to study the behavior of R_2* as a function of GA.

MRI R_2* (or T_2*) mapping may have the potential for detecting IPD. One previous study found significantly higher placental T_2* for normal pregnancies versus IUGR pregnancies[33]. Another study showed an improvement in the receiver operating characteristic curve using T_2* mapping for the detection of IUGR, compared to the uterine artery pulsatility index[31]. Based on these studies, we expected a higher R_2* to be associated with hypoxia, but in one preeclampsia subject whom we studied, a lower mean placental R_2* compared to normal subjects was observed. Using the FB radial technique to inspect the 3D R_2* maps of the full placental volume, we observed R_2* spatial variation across the placenta with lower R_2* in the center of the placenta and hot spots of higher R_2* along the periphery. Due to the limited knowledge of the behavior of placental R_2* at early gestation in normal and IPD pregnancies, further investigation with additional IPD subjects is needed to determine the relationship between R_2* characteristics and IPD.

Repeatability analysis of FB radial R_2* mapping at 3 T showed better repeatability for all subjects at 14-18 weeks GA (CR $\approx$ 3 s^{-1}) compared to 19-23 weeks GA (CR $\approx$ 8 s^{-1}). In the 19-23 weeks GA range, better repeatability was observed for anterior (CR $\approx$ 5 s^{-1}) compared to posterior placentas (CR $\approx$ 11 s^{-1}). This was due to two severe outliers, defined as being larger than the 3rd quartile by at least 3 $\times$ the interquartile range of the mean differences[211], that were from posterior placentas at 19-23 weeks GA. For these outliers, FB radial scan 1 and scan 2 showed R_2* differences of approximately 7 s^{-1} and 13 s^{-1}. Using the FB radial self-navigation signal[197], we found that these two outliers experienced substantial motion during FB radial scan

2 of 9 mm due to uterine contractions and 23 mm due to bulk patient motion, respectively. These levels of motion were substantially higher than in the other subjects (mean motion = 1.15 ± 1.42 mm, range of motion = 0-8 mm). Since these outliers only occurred during scan 2 and these scans could not be repeated due to scan time constraints, only scan 1 was used to determine mean R_2*, ΔR_2*, and CV. Therefore, these outliers did not affect the baseline R_2* findings, but they did affect the repeatability results. With these outliers removed, repeatability for all subjects and posterior placentas at 19-23 weeks GA was MD_{within} = 0.34 s^{-1}, MD_{abs} = 1.14 s^{-1}, SD_{within} = 1.52 s^{-1} and CR = 4.20 s^{-1}; and MD_{within} = 0.46 s^{-1}, MD_{abs} = 1.05 s^{-1}, SD_{within} = 1.39 s^{-1} and CR = 3.85 s^{-1}, respectively. To overcome these high levels of motion and improve R_2* mapping, FB radial can be extended to compensate for motion using self-navigation information[98,100,197]. This will be a topic of future work.

MRI has not been associated with any negative effects on maternal and fetal health, but the benefits versus risks should be carefully considered before referring pregnant women to MRI. As a general guideline, MRI is typically only performed in medically indicated cases where the benefits outweigh the risks of MRI. The main safety considerations for fetal imaging are the loud noise and biological effects due to time-varying magnetic fields and the specific absorption rate that can cause heating in the subject due to the radiofrequency fields[212]. Studies in pregnant women and infants have shown no significant biological effects or adverse events after undergoing MRI[212,213]. To reduce the safety risk due to noise in our study, the total MRI acquisition time was limited to 30 minutes. Furthermore, the FB radial technique used a low flip angle of 5 degrees to limit the specific absorption rate to the subject. For our FB radial technique, the whole body specific absorption rate was 0.08 W/kg and the B_{1+rms} was 0.4 μT.

Our study demonstrates the potential of FB radial 3D R_2* mapping in the placenta, but

there are limitations to consider. First, there was reduced placenta contrast on T_1-weighted gradient-echo images compared to T_2-weighted images. Therefore, registration was performed prior to contouring the placenta; however, there may be some errors in the registration. To correct for these errors, ROIs were placed on FB radial images and R_2* maps and then were adjusted by an experienced radiologist and an experienced maternal fetal medicine specialist, masked to the pregnancy outcomes. Second, for the in vivo placenta MRI experiments, a reference BH Cartesian scan was not performed for comparison. Due to scan time and comfort considerations for the pregnant subjects, performing a reference BH Cartesian scan was not practical. Therefore, we performed phantom experiments to evaluate the accuracy of FB radial R_2* mapping with respect to the reference Cartesian method. Third, there are some susceptibility and streaking artifacts on FB radial images and R_2* maps. Susceptibility artifacts can cause increased R_2* in small portions of the placenta if the placenta is oriented near air within the pelvis. To overcome this limitation, ROIs were drawn or adjusted to avoid susceptibility artifacts and this was also confirmed by the experienced radiologist and experienced maternal fetal medicine specialist. Susceptibility artifacts may be mitigated by including quantitative susceptibility mapping and using this to correct for these artifacts[214]. FB radial images and R_2* maps may be affected by radial streaking artifacts due to undersampling. In this study, FB radial images were undersampled to reduce the scan time to approximately three minutes. Acquiring fully sampled data or employing non-Cartesian parallel imaging reconstruction techniques, such as ESPIRiT[158], may improve the image quality and mitigate streaking artifacts. Fourth, this was a single-site study with only 30 normal pregnant subjects and 3 IPD subjects. However, our new FB radial technique already demonstrates highly repeatable R_2* mapping at 3 T during early gestation. More subjects will be included in the future to improve our understanding of R_2*

characteristics during normal pregnancies. Finally, there were only 3 subjects in our pilot IPD cohort. More IPD subjects will need to be included in future work to investigate the R_2* characteristics for specific IPD conditions and enable statistical analyses for group comparisons. Of these 3 subjects, 2 had IUGR, defined at delivery as birth weight less than 10th percentile for GA. However, the widely used definition of IUGR used by the American College of Obstetrics and Gynecology (ACOG)[215] is defined as estimated fetal weight less than 10th percentile for GA[215]. This is because IUGR is truly characterized by reduced growth restriction and clinical features of malnutrition in utero, regardless of birth weight[216,217]. In our study, IUGR was determined at delivery instead of in utero. Therefore, our criteria includes infants that were in fact born small for gestational age, but may not necessarily be truly IUGR[215–217]. Thus, using this criterion, IUGR could be over diagnosed and missed. Despite the limitations of this definition, ultrasound has low sensitivity[26,28,29]. For this reason, we selected this definition of IUGR. In addition, only 2 IUGR subjects were identified; therefore, we did not conclude differences between IUGR subjects and normal pregnant subjects. In future work with more IUGR subjects, the IUGR definition may be modified to determine differences between IUGR and normal pregnant subjects.

6.5 Conclusion

In conclusion, we have proposed and evaluated a new FB radial technique for 3D R_2* mapping in the full placental volume in 3 minutes. This technique demonstrated accurate and repeatable R_2* mapping in a R_2* phantom, and repeatable R_2* mapping in normal pregnant subjects. Using FB radial, we measured placental R_2* during early gestation at 3 T. The baseline mean R_2* (±SD) was 12.9 s^{-1} ± 2.7 s^{-1} for 14-18 weeks GA and 13.2 s^{-1} ± 1.9 s^{-1} for 19-23 weeks GA in normal pregnancies. In addition, for all subjects and specifically for anterior placentas, a

significantly higher CV was observed for 14-18 weeks GA compared to 19-23 weeks GA. At 19-23 weeks GA, a lower CV was observed for anterior placentas compared to posterior placentas. Compared to normal subjects, one IPD subject had substantially lower mean placental R_2* and different R_2* spatial characteristics at 14-18 weeks and 19-23 weeks GA. FB radial can be used to quantify R_2* in the placenta of pregnant subjects and may be an important tool to further study and improve early detection and management of abnormal pregnancies due to IPD.

This work has been published as:

Armstrong T, Liu D, Martin T, Masamed R, Janzen Carla, Wong C, Chanlaw T, Devaskar SU, Sung K, and Wu HH. 3D R_2* mapping of the placenta during early gestation using free-breathing multiecho stack-of-radial MRI at 3 T. Journal of Magnetic Resonance Imaging 2018; Early View. doi: 10.1002/jmri.26203

7 SUMMARY AND FUTURE STUDIES

In summary, we have developed a FB radial MRI technique for fat and R_2* quantification in the abdomen and pelvis. This technique has demonstrated accurate and repeatable fat and R_2* quantification in populations consisting of healthy subjects and patients. FB radial demonstrated improved image quality in children and infants, which are populations that may have reduced or no breath-hold ability, respectively. Due to its robustness to motion, FB radial has the potential to be translated to other patient populations that are not capable of breath holding, such as sick, elderly, and mentally impaired patients. This technique may be involved in many future applications in the abdomen and pelvis such as body composition analysis, hepatic fat quantification, and placental R_2* mapping. The FB radial technique also allows for higher-resolution, greater spatial coverage, or higher SNR, as there is no breath-hold scan time limitation. Further optimization and evaluation of FB radial fat quantification for these clinical applications will be the topic of future research. Future directions for FB radial include motion compensation, concomitant gradient correction, liver R_2* quantification, magnetic resonance

elastography (MRE) and additional patient studies.

7.1 Motion Compensation Techniques

To further improve the motion robustness of 3D stack-of-radial trajectories, recent work has developed and investigated 3D stack-of-radial trajectories with golden angle rotation along k_z which may improve motion robustness when the time to acquire k_z lines is longer than the time scale of the motion[218]. This trajectory may be applied in future work.

FB radial data acquired with golden-angle ordering has the additional advantage that the data can be used to generate a self-navigation signal which we have investigated in previous work[160,194]. Golden-angle ordering allows for adequate sampling of k-space and the reconstruction of an arbitrary number of radial views when data has been discarded[63]. Using the self-navigation signal, a motion state can be identified and data can be discarded (hard-gating) or weighted (soft-gating) to potentially provide improved image quality in the liver. FB radial data can also be combined with k-space weighted image contrast (KWIC)[219] reconstruction to generate images with a smaller temporal frame rate and create image-based motion tracking. The information from the image-based motion tracking can also be used for gating to potentially provide improved image quality in the liver.

Another motion compensation strategy is to perform acceleration to reduce the acquisition time. In Chapter 3, acceleration was performed in healthy subjects without advanced reconstructions techniques and has shown quantitative accuracy compared to BH techniques; however, images and PDFF maps had increased radial streaking due to undersampling. Undersampled data resulting from acceleration or self-navigation may be combined with advanced reconstruction techniques such as ESPIRiT[158] or compressed sensing[99,220] to mitigate

streaking artifacts due to undersampling. This will be a topic of future work.

7.2 Concomitant Gradient Correction

Concomitant gradient effects can potentially confound CSE-MRI and the quantification of PDFF. There are two main considerations related to the effects of concomitant gradients for our FB radial fat quantification technique[221,222]. The first is the effect of concomitant gradients on radial data acquisition, which could cause blurring in the radial images[221]. However, since our sequence design has a short readout window for each radial spoke and we typically have an axial slab with a maximum z position of ± 10cm from isocenter, the extra phase due to concomitant gradients did not cause noticeable blurring in slices toward the edge of the axial slab. The second is the effect of concomitant gradients on CSE-MRI and PDFF. Since we utilize a single bipolar echo train in each TR and the complex fitting algorithm accounts for the field inhomogeneity slice by slice, the extra frequency/phase effects due to concomitant gradients were incorporated as a component of the apparent B_0 field off resonance term in the signal model and does not create errors in the PDFF calculation[222]. Future work can investigate a correction for the effects of concomitant gradients in our FB radial technique.

7.3 Liver R_2* Mapping for Liver Iron Quantification

This work focused on fat quantification using the proposed FB radial technique and did not investigate R_2^* quantification for characterization of iron content in the liver[223]. In adults, concomitant NAFLD and iron overload[57] may occur. Notably, the proposed FB radial technique already employs the same fat and R_2^* signal model in Equation 2-4 which is used by the BH Cartesian technique and has previously been evaluated in concomitant NAFLD and iron overload patients[57]. R_2* determined by MRI is related to the liver iron concentration and can be used to

quantify liver iron[57]. Future work entails combining fat and R_2* quantification in adult patients for the evaluation of hepatic fat and iron content. For iron overload patients, a shorter initial echo time and shorter echo spacing may be required. Further work can investigate using asymmetric echo sequence for a shorter initial echo time and echo spacing and an interleaved TR[224] sequence for shorter echo spacing.

R_2^* mapping can be affected by confounding factors such as macroscopic background gradients induced by large susceptibility differences[205,225]. Compared to Cartesian trajectories, radial trajectories have greater sensitivities to off-resonance effects such as B_0 inhomogeneity and macroscopic gradients[60]. In radial trajectories, the center of k-space is acquired during each readout and off-resonance throughout the scan can lead to misalignments of the center of k-space causing additional signal decay (see **section 2.8**)[60]. Macroscopic background gradients can cause additional off-resonance and intravoxel dephasing, particularly near areas with rapid susceptibility changes, such as near air-tissue interfaces[205,225]. This leads to a severe R_2^* overestimation near the liver dome where there are rapid susceptibility changes near the liver-lung interface. The signal model including background gradients at pixel location $\mathrm{q} = (\mathrm{x}, \mathrm{y}, \mathrm{z})$ is[205]

Equation 7-1

$$S_q(TE_n) = \left(W_q + F_q \cdot c(TE_n)\right) \cdot e^{-R_{2,q}^* TE_n} \cdot e^{i2\pi\varphi_{q(z_0)} TE_n} \times \int a(z) \cdot e^{i2\pi(\varphi_{q(z)} - \varphi_{q(z_0)})TE_n} \cdot SRF(z - z_0)dz$$

where $c(TE_n)$ accounts for the multi-peak spectral model for fat (i.e. $c(TE_n) = \sum_{j=1}^{M} a_j \cdot e^{i2\pi f_j TE_n}$), $a(z) = W(z) + F(z)$ indicates the overall signal amplitude, and $SRF(z - z_0)$ indicates the spatial response function of a voxel centered at z_0[205]. Developing and evaluating a

correction for effects due to background gradients will be a topic of investigation in future work.

7.4 Magnetic Resonance Elastography

Magnetic resonance elastography (MRE) is a novel tool to quantify liver stiffness for the diagnosis and staging of fibrosis and cirrhosis. Conventional MRE techniques use Cartesian trajectories and typically employ 2D multislice acquisitions with only a few slices[226–229]. These acquisitions are performed using a single-breath-hold or multi-breath-hold[226–229] which limits the signal-to-noise ratio, liver coverage, and spatial resolution. A FB radial technique may allow for the acquisition of higher signal-to-noise ratio, larger volumetric coverage and higher spatial resolutions in the liver. This may improve the diagnosis and staging of fibrosis in the liver. Future work can include developing a novel FB radial technique for MRE. This technique may be useful in pediatric populations who have greater difficulty following operator instructions or have limited breath-hold ability.

7.5 Future Patient Studies

In Chapters 4 and 5 only ten healthy children, nine children with NAFLD, and ten infants were scanned in these studies. In future work, additional children will be required to determine significant correlations between clinical characteristics and hepatic PDFF. More infants will be required to determine significant differences in hepatic fat or body composition measurements for infants at-risk for future metabolic syndrome.

For placenta R_2* mapping, only thirty subjects and three IPD subjects were used to determine baseline R_2* characteristics. Due to the limited knowledge of the behavior of placental R_2* at early gestation in normal and IPD pregnancies, further investigation with additional IPD

subjects is needed to determine the relationship between R_2* characteristics and IPD. In future studies, additional healthy subjects and IPD subjects can be included to determine the behavior of R_2* as a function of GA and differences between healthy subjects and IPD subjects.

7.6 Conclusion

FB radial MRI has many potential applications in the liver and abdomen. This technique can provide accurate fat and R_2* quantification which may help diagnose, evaluate, and manage diseases such as IPD, obesity, and NAFLD. FB radial provides greater inherent robustness to motion enabling FB MRI and provides improved image quality in children with NAFLD and infants who may have limited or no breath-hold ability, respectively. This technique may improve the diagnosis and management of conditions such as NAFLD and IPD, especially in populations where breath-holding is not possible.

8 REFERENCES

1. World Health Organization. Obesity and overweight. http://www.who.int/news-room/fact-sheets/detail/obesity-and-overweight. Published 2018. Accessed April 9, 2018.

2. Sundaram SS, Zeitler P, Nadeau K. The metabolic syndrome and nonalcoholic fatty liver disease in children. *Curr Opin Pediatr*. 2009;21(4):529–535. doi:10.1097/MOP.0b013e32832cb16f.

3. Kim CH, Younossi ZM. Nonalcoholic fatty liver disease: A manifestation of the metabolic syndrome. *Cleve Clin J Med*. 2008;75(10):721–728. doi:10.3949/ccjm.75.10.721.

4. Centers for Disease Control and Prevention. Overweight and Obesity. https://www.cdc.gov/obesity/index.html. Accessed May 19, 2018.

5. Younossi ZM. Review article: Current management of non-alcoholic fatty liver disease and non-alcoholic steatohepatitis. *Aliment Pharmacol Ther*. 2008;28(1):2-12. doi:10.1111/j.1365-2036.2008.03710.x.

6. Giorgio V, Prono F, Graziano F, Nobili V. Pediatric non alcoholic fatty liver disease: old

and new concepts on development, progression, metabolic insight and potential treatment targets. *BMC Pediatr*. 2013;13(1):40. doi:10.1186/1471-2431-13-40.

7. Pardee PE, Lavine JE, Schwimmer JB. Diagnosis and treatment of pediatric nonalcoholic steatohepatitis and the implications for bariatric surgery. *Semin Pediatr Surg*. 2009;18(3):144-151. doi:10.1053/j.sempedsurg.2009.04.004.

8. Feldstein AE, Charatcharoenwitthaya P, Treeprasertsuk S, Benson JT, Enders FB, Angulo P. The natural history of non-alcoholic fatty liver disease in children: a follow-up study for up to 20 years. *Gut*. 2009;58(11):1538-1544. doi:10.1136/gut.2008.171280.

9. Wong RJ, Aguilar M, Cheung R, et al. Nonalcoholic steatohepatitis is the second leading etiology of liver disease among adults awaiting liver transplantation in the United States. *Gastroenterology*. 2015;148(3):547-555. doi:10.1053/j.gastro.2014.11.039.

10. Uppal V, Mansoor S, Furuya KN. Pediatric non-alcoholic fatty liver disease. *Curr Gastroenterol Rep*. 2016;18(5). doi:10.1007/s11894-016-0498-9.

11. Della Corte C, Vajro P, Socha P, Nobili V. Pediatric non-alcoholic fatty liver disease: recent advances. *Clin Res Hepatol Gastroenterol*. 2014;38(4):419-422. doi:10.1016/j.clinre.2014.02.008.

12. Tapper EB, Lok AS-F. Use of Liver Imaging and Biopsy in Clinical Practice. *N Engl J Med*. 2017;377(8):756-768. doi:10.1056/NEJMra1610570.

13. Sumida Y, Nakajima A, Itoh Y. Limitations of liver biopsy and non-invasive diagnostic tests for the diagnosis of nonalcoholic fatty liver disease/nonalcoholic steatohepatitis. *World J Gastroenterol*. 2014;20(2):475-485. doi:10.3748/wjg.v20.i2.475.

14. Loomba R, Sirlin CB, Schwimmer JB, Lavine JE. Advances in pediatric nonalcoholic

fatty liver disease. *Hepatology*. 2009;50(4):1282-1293. doi:10.1002/hep.23119.

15. Lee SS, Park SH. Radiologic evaluation of nonalcoholic fatty liver disease. *World J Gastroenterol*. 2014;20(23):7392-7402. doi:10.3748/wjg.v20.i23.7392.

16. Szczepaniak LS, Nurenberg P, Leonard D, et al. Magnetic resonance spectroscopy to measure hepatic triglyceride content: prevalence of hepatic steatosis in the general population. *Am J Physiol Endocrinol Metab*. 2005;288(2):E462-E468. doi:10.1152/ajpendo.00064.2004.

17. Bohte AE, van Werven JR, Bipat S, Stoker J. The diagnostic accuracy of US, CT, MRI and H-1-MRS for the evaluation of hepatic steatosis compared with liver biopsy: a meta-analysis. *Eur Radiol*. 2011;21(1):87-97. doi:DOI 10.1007/s00330-010-1905-5.

18. Georgoff P, Thomasson D, Louie A, et al. Hydrogen-1 MR spectroscopy for measurement and diagnosis of hepatic steatosis. *AJR Am J Roentgenol*. 2012;199(1):2-7. doi:10.2214/AJR.11.7384.

19. Toro-Ramos T, Paley C, Pi-Sunyer FX, Gallagher D. Body composition during fetal development and infancy through the age of 5 years. *Eur J Clin Nutr*. 2015;69(12):1279-1289. doi:10.1038/ejcn.2015.117.

20. Wells JCK, Fewtrell MS. Is body composition important for paediatricians? *Arch Dis Child*. 2008;93(2):168-172. doi:10.1136/adc.2007.115741.

21. Toomey CM, Cremona A, Hughes K, Norton C, Jakeman P. A review of body composition measurement in the assessment of health. *Top Clin Nutr*. 2015;30(1):16-32. doi:10.1097/TIN.0000000000000017.

22. Ananth C V. Ischemic placental disease: A unifying concept for preeclampsia, intrauterine

growth restriction, and placental abruption. *Semin Perinatol*. 2014;38(3):131-132. doi:10.1053/j.semperi.2014.03.001.

23. Parker SE, Werler MM. Epidemiology of ischemic placental disease: A focus on preterm gestations. *Semin Perinatol*. 2014;38(3):133-138. doi:10.1053/j.semperi.2014.03.004.

24. Parks WT. Placental hypoxia: The lesions of maternal malperfusion. *Semin Perinatol*. 2015;39(1):9-19. doi:10.1053/j.semperi.2014.10.003.

25. Kingdom JCP, Kaufmann P. Oxygen and placental villous development: Origins of fetal hypoxia. *Placenta*. 1997;18(8):613-621. doi:10.1016/S0143-4004(97)90000-X.

26. Vintzileos AM, Ananth C V. First trimester prediction of ischemic placental disease. *Semin Perinatol*. 2014;38(3):159-166. doi:S0146-0005(14)00016-0 [pii]\r10.1053/j.semperi.2014.03.006.

27. Ananth C V., Vintzileos AM. Maternal-fetal conditions necessitating a medical intervention resulting in preterm birth. *Am J Obstet Gynecol*. 2006;195(6):1557-1563. doi:10.1016/j.ajog.2006.05.021.

28. Bamfo JE a K, Odibo AO. Diagnosis and management of fetal growth restriction. *J Pregnancy*. 2011;2011:640715. doi:10.1155/2011/640715.

29. Khong SL, Kane SC, Brennecke SP, Da Silva Costa F. First-trimester uterine artery doppler analysis in the prediction of later pregnancy complications. *Dis Markers*. 2015;2015. doi:10.1155/2015/679730.

30. Sinding M, Peters DA, Frøkjær JB, et al. Placental magnetic resonance imaging T2* measurements in normal pregnancies and in those complicated by fetal growth restriction. *Ultrasound Obstet Gynecol*. 2016;47(6):748-754. doi:10.1002/uog.14917.

31. Sinding M, Peters DA, Frøkjær JB, et al. Prediction of low birth weight: Comparison of placental T2* estimated by MRI and uterine artery pulsatility index. *Placenta*. 2017;49:48-54. doi:10.1016/j.placenta.2016.11.009.

32. Huen I, Morris DM, Wright C, et al. R1 and R2 * changes in the human placenta in response to maternal oxygen challenge. *Magn Reson Med*. 2013;70(5):1427-1433. doi:10.1002/mrm.24581.

33. Sinding M, Peters DA, Poulsen SS, et al. Placental baseline conditions modulate the hyperoxic BOLD-MRI response. *Placenta*. 2018;61:17-23. doi:10.1016/j.placenta.2017.11.002.

34. Hernando D, Kellman P, Haldar JP, Liang Z-P. Robust water/fat separation in the presence of large field inhomogeneities using a graph cut algorithm. *Magn Reson Med*. 2010;63(1):79-90. doi:10.1002/mrm.22177.

35. ISMRM Fat Water Toolbox 2012.

36. Yu H, Shimakawa A, McKenzie CA, Brodsky E, Brittain JH, Reeder SB. Multiecho water-fat separation and simultaneous R2* estimation with multifrequency fat spectrum modeling. *Magn Reson Med*. 2008;60(5):1122-1134. doi:10.1002/mrm.21737.

37. Meisamy S, Hines CDG, Hamilton G, et al. Quantification of hepatic steatosis with T1-independent, T2-corrected MR imaging with spectral modeling of fat: blinded comparison with MR spectroscopy. *Radiology*. 2011;258(3):767-775. doi:10.1148/radiol.10100708.

38. Hines CDG, Yu H, Shimakawa A, McKenzie CA, Brittain JH, Reeder SB. T1 independent, T2* corrected MRI with accurate spectral modeling for quantification of fat: Validation in a fat-water-SPIO phantom. *J Magn Reson Imaging*. 2009;30(5):1215-1222.

doi:10.1002/jmri.21957.

39. Reeder SB, Cruite I, Hamilton G, Sirlin CB. Quantitative assessment of liver fat with magnetic resonance imaging and spectroscopy. *J Magn Reson Imaging*. 2011;34(4):729-749. doi:10.1002/jmri.22775.

40. Wang X, Hernando D, Reeder SB. Sensitivity of chemical shift-encoded fat quantification to calibration of fat MR spectrum. *Magnetic Resonance in Medicine*. 2016.

41. Liu CY, McKenzie CA, Yu H, Brittain JH, Reeder SB. Fat quantification with IDEAL gradient echo imaging: Correction of bias from T1 and noise. *Magn Reson Med*. 2007;58(2):354-364. doi:10.1002/mrm.21301.

42. Horng DE, Hernando D, Hines CDG, Reeder SB. Comparison of R2* correction methods for accurate fat quantification in fatty liver. *J Magn Reson Imaging*. 2013;37(2):414-422. doi:10.1002/jmri.23835.

43. Chavhan GB, Babyn PS, Vasanawala SS. Abdominal MR imaging in children: motion compensation, sequence optimization, and protocol organization. *Radiographics*. 2013;33(3):703-719. doi:10.1148/rg.333125027.

44. Bashir MR, Zhong X, Nickel MD, et al. Quantification of hepatic steatosis with a multistep adaptive fitting MRI approach: Prospective validation against MR spectroscopy. *Am J Roentgenol*. 2015;204(2):297-306. doi:10.2214/AJR.14.12457.

45. Koh H, Kim S, Kim MJ, Kim HG, Shin HJ, Lee MJ. Hepatic fat quantification magnetic resonance for monitoring treatment response in pediatric nonalcoholic steatohepatitis. *World J Gastroenterol*. 2015;21(33):9741-9748. doi:10.3748/wjg.v21.i33.9741.

46. Achmad E, Yokoo T, Hamilton G, et al. Feasibility of and agreement between MR

imaging and spectroscopic estimation of hepatic proton density fat fraction in children with known or suspected nonalcoholic fatty liver disease. *Abdom Imaging*. 2015;40(8):3084-3090. doi:10.1007/s00261-015-0506-9.

47. Schwimmer JB, Middleton MS, Behling C, et al. Magnetic resonance imaging and liver histology as biomarkers of hepatic steatosis in children with nonalcoholic fatty liver disease. *Hepatology*. 2015;61(6):1887-1895. doi:10.1002/hep.27666.

48. Joshi M, Dillman JR, Singh K, et al. Quantitative MRI of fatty liver disease in a large pediatric cohort: correlation between liver fat fraction, stiffness, volume, and patient-specific factors. *Abdom Radiol*. 2017. doi:10.1007/s00261-017-1289-y.

49. Rasmussen JM, Entringer S, Nguyen A, et al. Brown adipose tissue quantification in human neonates using water-fat separated MRI. *PLoS One*. 2013;8(10). doi:10.1371/journal.pone.0077907.

50. Entringer S, Rasmussen J, Cooper DM, et al. Association between supraclavicular brown adipose tissue composition at birth and adiposity gain from birth to 6 months of age. *Pediatr Res*. 2017;82(6):1017-1021. doi:10.1038/pr.2017.159.

51. Hu HH, Yin L, Aggabao PC, Perkins TG, Chia JM, Gilsanz V. Comparison of brown and white adipose tissues in infants and children with chemical-shift-encoded water-fat MRI. *J Magn Reson Imaging*. 2013;38(4):885-896. doi:10.1002/jmri.24053.

52. Dyke JP, Garfinkel AC, Groves AM, Kovanlikaya A. High-resolution rapid neonatal whole-body composition using 3.0 Tesla chemical shift magnetic resonance imaging. *Pediatr Res*. 2018;83(3):638-644. doi:10.1038/pr.2017.294.

53. Yu NY, Wolfson T, Middleton MS, et al. Bone marrow fat content is correlated with

hepatic fat content in paediatric non-alcoholic fatty liver disease. *Clin Radiol*. 2017;72(5):425.e9-425.e14. doi:10.1016/j.crad.2016.11.017.

54. Yokoo T, Bydder M, Hamilton G, et al. Nonalcoholic Fatty Liver Disease: Diagnostic and Fat-Grading Accuracy of Low-Flip-Angle Multiecho Gradient-Recalled-Echo MR Imaging at 1.5 T. *Radiology*. 2009;251(1):67-76. doi:10.1148/radiol.2511080666.

55. Yokoo T, Shiehmorteza M, Hamilton G, et al. Estimation of hepatic proton-density fat fraction by using MR imaging at 3.0 T. *Radiology*. 2011;258(3):749-759. doi:10.1148/radiol.10100659.

56. Zhong X, Nickel MD, Kannengiesser SAR, Dale BM, Kiefer B, Bashir MR. Liver fat quantification using a multi-step adaptive fitting approach with multi-echo GRE imaging. *Magn Reson Med*. 2014;72:1353-1365. doi:10.1002/mrm.25054.

57. Horng DE, Hernando D, Reeder SB. Quantification of liver fat in the presence of iron overload. *J Magn Reson Imaging*. 2017. doi:10.1002/jmri.25382.

58. Courtier J, Rao AG, Anupindi SA. Advanced imaging techniques in pediatric body MRI. *Pediatr Radiol*. 2017;47(5):522-533. doi:10.1007/s00247-017-3778-0.

59. Jaimes C, Gee MS. Strategies to minimize sedation in pediatric body magnetic resonance imaging. *Pediatr Radiol*. 2016;46(6):916-927. doi:10.1007/s00247-016-3613-z.

60. Peters DC, Derbyshire JA, McVeigh ER. Centering the projection reconstruction trajectory: Reducing gradient delay errors. *Magn Reson Med*. 2003;50:1-6. doi:10.1002/mrm.10501.

61. Block KT, Chandarana H, Milla S, et al. Towards routine clinical use of radial stack-of-stars 3D gradient-echo sequences for reducing motion sensitivity. *J Korean Soc Magn*

Reson Med. 2014;18(2):87-106. doi:10.13104/jksmrm.2014.18.2.87.

62. Fujinaga Y, Kitou Y, Ohya A, et al. Advantages of radial volumetric breath-hold examination (VIBE) with k-space weighted image contrast reconstruction (KWIC) over Cartesian VIBE in liver imaging of volunteers simulating inadequate or no breath-holding ability. *Eur Radiol*. 2016;26(8):2790-2797. doi:10.1007/s00330-015-4103-7.

63. Winkelmann S, Schaeffter T, Koehler T, Eggers H, Doessel O. An optimal radial profile order based on the golden ratio for time-resolved MRI. *IEEE Trans Med Imaging*. 2007;26(1):68-76. doi:10.1109/TMI.2006.885337.

64. Motosugi U, Hernando D, Bannas P, et al. Quantification of liver fat with respiratory-gated quantitative chemical shift encoded MRI. *J Magn Reson Imaging*. 2015;42(5):1241-1248. doi:10.1002/jmri.24896.

65. Coakley F V., Glenn OA, Qayyum A, Barkovich AJ, Goldstein R, Filly RA. Fetal MRI: A Developing Technique for the Developing Patient. *Am J Roentgenol*. 2004;182(1):243-252. doi:10.2214/ajr.182.1.1820243.

66. Prayer D, Brugger PC, Prayer L. Fetal MRI: Techniques and protocols. *Pediatr Radiol*. 2004;34(9):685-693. doi:10.1007/s00247-004-1246-0.

67. Armstrong T, Liu D, Martin T, et al. Free-breathing R2* Characterization of the Placenta During Normal Early Gestation Using a Multiecho 3D Stack-of-Radial Technique. In: *Proceedings of the International Society for Magnetic Resonance in Medicine 25th*. Honolulu, Hawaii, United States; 2017:0117.

68. Bydder M, Yokoo T, Hamilton G, et al. Relaxation effects in the quantification of fat using gradient echo imaging. *Magn Reson Imaging*. 2008;26:347-359.

doi:10.1016/j.mri.2007.08.012.

69. Hu HH, Li Y, Nagy TR, Goran MI, Nayak KS. Quantification of Absolute Fat Mass by Magnetic Resonance Imaging: a Validation Study against Chemical Analysis. *Int J Body Compos Res*. 2011;9(3):111-122. http://www.pubmedcentral.nih.gov/articlerender.fcgi?artid=3509746&tool=pmcentrez&rendertype=abstract.

70. Reeder SB, Hu HH, Sirlin CB. Proton density fat-fraction: A standardized mr-based biomarker of tissue fat concentration. *J Magn Reson Imaging*. 2012;36(5):1011-1014. doi:10.1002/jmri.23741.

71. Shen W, Liu H, Punyanitya M, Chen J, Heymsfield SB. Pediatric obesity phenotyping by magnetic resonance methods. *Curr Opin Clin Nutr Metab Care*. 2005;8(6):595-601. doi:10.1097/01.mco.0000171150.49248.14.

72. Idilman IS, Aniktar H, Idilman R, et al. Hepatic steatosis: quantification by proton density fat fraction with MR imaging versus liver biopsy. *Radiology*. 2013;267(3):767-775. doi:10.1148/radiol.13121360.

73. Dong Z, Luo Y, Cai H, et al. Noninvasive fat quantification of the liver and pancreas may provide potential biomarkers of impaired glucose tolerance and type 2 diabetes. *Med (United States)*. 2016;95(23):e3858. doi:10.1097/MD.0000000000003858.

74. Unger RH. Minireview: Weapons of Lean Body Mass Destruction: The Role of Ectopic Lipids in the Metabolic Syndrome. *Endocrinology*. 2003;144(12):5159-5165. doi:10.1210/en.2003-0870.

75. Després J-P, Lemieux I, Bergeron J, et al. Abdominal Obesity and the Metabolic

Syndrome: Contribution to Global Cardiometabolic Risk. *Arterioscler Thromb Vasc Biol*. 2008;28(6):1039-1049. doi:10.1161/ATVBAHA.107.159228.

76. Dunn W, Xu R, Wingard DL, et al. Suspected Nonalcoholic Fatty Liver Disease and Mortality Risk in a Population-based Cohort Study. *Am J Gastroenterol*. 2008;103(9):2263-2271. doi:10.1111/j.1572-0241.2008.02034.x.

77. Fabbrini E, Magkos F, Mohammed BS, et al. Intrahepatic fat, not visceral fat, is linked with metabolic complications of obesity. *Proc Natl Acad Sci*. 2009;106(36):15430-15435. doi:10.1073/pnas.0904944106.

78. Francque SM, van der Graaff D, Kwanten WJ. Non-alcoholic fatty liver disease and cardiovascular risk: Pathophysiological mechanisms and implications. *J Hepatol*. 2016;65(2):425-443. doi:10.1016/j.jhep.2016.04.005.

79. Wahba IM, Mak RH. Obesity and obesity-initiated metabolic syndrome: Mechanistic links to chronic kidney disease. *Clin J Am Soc Nephrol*. 2007. doi:10.2215/CJN.04071206.

80. Björntorp P. Metabolic implications of body fat distribution. *Diabetes Care*. 1991. doi:10.2337/diacare.14.12.1132.

81. Snijder MB, van Dam RM, Visser M, Seidell JC. What aspects of body fat are particularly hazardous and how do we measure them? *Int J Epidemiol*. 2006. doi:10.1093/ije/dyi253.

82. Liu CY, Redheuil A, Ouwerkerk R, Lima JAC, Bluemke DA. Myocardial fat quantification in humans: Evaluation by two-point water-fat imaging and localized proton spectroscopy. *Magn Reson Med*. 2010. doi:10.1002/mrm.22289.

83. Heber SD, Hetterich H, Lorbeer R, et al. Pancreatic fat content by magnetic resonance imaging in subjects with prediabetes, diabetes, and controls from a general population

without cardiovascular disease. *PLoS One*. 2017;12(5). doi:10.1371/journal.pone.0177154.

84. Sijens PE, Edens MA, Bakker SJL, Stolk RP. MRI-determined fat content of human liver, pancreas and kidney. *World J Gastroenterol*. 2010;16(16):1993–1998. doi:10.3748/wjg.v16.i16.1993.

85. Lee JS, Kim SH, Jun DW, et al. Clinical implications of fatty pancreas: Correlations between fatty pancreas and metabolic syndrome. *World J Gastroenterol*. 2009;15(15):1869-1875. doi:10.3748/wjg.15.1869.

86. Chavhan GB, Babyn PS, Thomas B, Shroff MM, Haacke EM. Principles, techniques, and applications of T2*-based MR imaging and its special applications. *Radiographics*. 2009;29(62983):1433-1449. doi:10.1148/rg.295095034.

87. Lu W, Yu H, Shimakawa A, Alley M, Reeder SB, Hargreaves B a. Water-fat separation with bipolar multiecho sequences. *Magn Reson Med*. 2008;60(1):198-209. doi:10.1002/mrm.21583.

88. Yu H, Shimakawa A, McKenzie CA, et al. Phase and amplitude correction for multi-echo water-fat separation with bipolar acquisitions. *J Magn Reson Imaging*. 2010;31:1264-1271. doi:10.1002/jmri.22111.

89. Peterson P. Fat quantification using multiecho sequences with bipolar gradients: Investigation of accuracy and noise performance. *Magn Reson Med*. 2014;71(1):219-229. doi:10.1002/mrm.24657.

90. Pineda AR, Reeder SB, Wen Z, Pelc NJ. Cramér-Rao bounds for three-point decomposition of water and fat. *Magn Reson Med*. 2005;54(3):625-635.

doi:10.1002/mrm.20623.

91. Sinding M, Peters D a., Frøkjaer JB, et al. Placental T2* measurements in normal pregnancies and in pregnancies complicated by fetal growth restriction. *Ultrasound Obstet Gynecol*. 2015:n/a-n/a. doi:10.1002/uog.14917.

92. Hernando D, Kramer JH, Reeder SB. Multipeak fat-corrected complex R2* relaxometry: Theory, optimization, and clinical validation. *Magn Reson Med*. 2013;70(5):1319-1331. doi:10.1002/mrm.24593.

93. Hernando D, Hines CDG, Yu H, Reeder SB. Addressing phase errors in fat-water imaging using a mixed magnitude/complex fitting method. *Magn Reson Med*. 2012;67(3):638-644. doi:10.1002/mrm.23044.

94. Hernando D, Liang ZP, Kellman P. Chemical shift-based water/fat separation: A comparison of signal models. *Magn Reson Med*. 2010;64(3):811-822. doi:10.1002/mrm.22455.

95. Kühn J-P, Hernando D, Muñoz del Rio A, et al. Effect of multipeak spectral modeling of fat for liver iron and fat quantification: correlation of biopsy with MR imaging results. *Radiology*. 2012;265(1):133-142. doi:10.1148/radiol.12112520.

96. Ren J, Dimitrov I, Sherry AD, Malloy CR. Composition of adipose tissue and marrow fat in humans by 1H NMR at 7 Tesla. *J Lipid Res*. 2008;49(9):2055-2062. doi:10.1194/jlr.D800010-JLR200.

97. Ehman RL, McNamara MT, Pallack M, Hricak H, Higgins CB. Magnetic resonance imaging with respiratory gating: Techniques and advantages. *Am J Roentgenol*. 1984;143(6):1175-1182. doi:10.2214/ajr.143.6.1175.

98. Feng L, Axel L, Chandarana H, Block KT, Sodickson DK, Otazo R. XD-GRASP: Golden-angle radial MRI with reconstruction of extra motion-state dimensions using compressed sensing. *Magn Reson Med*. 2016;75(2):775-788. doi:10.1002/mrm.25665.

99. Thomas B, Li F, K. SD, Hersh C, Tobias BK. Free-breathing volumetric fat/water separation by combining radial sampling, compressed sensing, and parallel imaging. *Magn Reson Med*. 2017;78(2):565-576. doi:10.1002/mrm.26392.

100. Arboleda C, Aguirre-Reyes D, García MP, et al. Total liver fat quantification using three-dimensional respiratory self-navigated MRI sequence. *Magn Reson Med*. 2016;76(5):1400-1409. doi:10.1002/mrm.26028.

101. Mendes J, Kholmovski E, Parker DL. Rigid-body motion correction with self-navigation MRI. *Magn Reson Med*. 2009;61(3):739-747. doi:10.1002/mrm.21883.

102. Spincemaille P, Liu J, Nguyen T, Prince MR, Wang Y. Z intensity-weighted position self-respiratory gating method for free-breathing 3D cardiac CINE imaging. *Magn Reson Imaging*. 2011;29(6):861-868. doi:10.1016/j.mri.2011.02.011.

103. Azevedo RM, De Campos ROP, Ramalho M, Herédia V, Dale BM, Semelka RC. Free-breathing 3D T1-weighted gradient-echo sequence with radial data sampling in abdominal MRI: Preliminary observations. *Am J Roentgenol*. 2011;197(3):650-657. doi:10.2214/AJR.10.5881.

104. Reiner CS, Neville AM, Nazeer HK, et al. Contrast-enhanced free-breathing 3D T1-weighted gradient-echo sequence for hepatobiliary MRI in patients with breath-holding difficulties. *Eur Radiol*. 2013;23(11):3087-3093. doi:10.1007/s00330-013-2910-2.

105. Huo D, Li Z, Aboussouan E, Karis JP, Pipe JG. Turboprop IDEAL: A motion-resistant

fat-water separation technique. *Magn Reson Med*. 2009;61(1):188-195. doi:10.1002/mrm.21825.

106. Moran CJ, Brodsky EK, Bancroft LH, et al. High-resolution 3D radial bSSFP with IDEAL. *Magn Reson Med*. 2014;71(1):95-104. doi:10.1002/mrm.24633.

107. Moriguchi H, Lewin JS, Duerk JL. Dixon Techniques in Spiral Trajectories With Off-Resonance Correction: A New Approach for Fat Signal Suppression Without Spatial-Spectral RF Pulses. *Magn Reson Med*. 2003;50(5):915-924. doi:10.1002/mrm.10629.

108. Börnert P, Koken P, Eggers H. Spiral water-fat imaging with integrated off-resonance correction on a clinical scanner. *J Magn Reson Imaging*. 2010;32(5):1262-1267. doi:10.1002/jmri.22336.

109. Wu HH, Jin HL, Nishimura DG. Fat/water separation using a concentric rings trajectory. *Magn Reson Med*. 2009;61(3):639-649. doi:10.1002/mrm.21865.

110. Williams S. Pearson's correlation coefficient. *N Z Med J*. 1996;109(1015):38. doi:10.1136/bmj.e4483.

111. Lin LI. A concordance correlation coefficient to evaluate reproducibility. *Biometrics*. 1989;45(1):255-268. doi:10.2307/2532051.

112. Bland JM, Altman DG. Measuring agreement in method comparison studies. *Stat Methods Med Res*. 1999;8(2):135-160. doi:10.1191/096228099673819272.

113. Bartlett JW, Frost C. Reliability, repeatability and reproducibility: Analysis of measurement errors in continuous variables. *Ultrasound Obstet Gynecol*. 2008;31(4):466-475. doi:10.1002/uog.5256.

114. Obuchowski NA, Reeves AP, Huang EP, et al. Quantitative imaging biomarkers: A review

of statistical methods for computer algorithm comparisons. *Stat Methods Med Res*. 2014;24(1):68-106. doi:10.1177/0962280214537390.

115. Vernon G, Baranova A, Younossi ZM. Systematic review: the epidemiology and natural history of non-alcoholic fatty liver disease and non-alcoholic steatohepatitis in adults. *Aliment Pharmacol Ther*. 2011;34:274-285. doi:10.1111/j.1365-2036.2011.04724.x.

116. Rinella ME. Nonalcoholic fatty liver disease: a systematic review. *JAMA*. 2015;313(22):2263-2273. doi:10.1001/jama.2015.5370.

117. Bellentani S, Marino M. Epidemiology and natural history of non-alcoholic fatty liver disease (NAFLD). *Ann Hepatol*. 2009;8:s4-s8.

118. de Alwis NMW, Day CP. Non-alcoholic fatty liver disease: The mist gradually clears. *J Hepatol*. 2008;48. doi:10.1016/j.jhep.2008.01.009.

119. Than NN, Newsome PN. A concise review of non-alcoholic fatty liver disease. *Atherosclerosis*. 2015;239(1):192-202. doi:10.1016/j.atherosclerosis.2015.01.001.

120. Ratziu V, Charlotte F, Heurtier A, et al. Sampling variability of liver biopsy in nonalcoholic fatty liver disease. *Gastroenterology*. 2005;128(7):1898-1906. doi:10.1053/j.gastro.2005.03.084.

121. Yu H, McKenzie CA, Shimakawa A, et al. Multiecho reconstruction for simultaneous water-fat decomposition and T2* estimation. *J Magn Reson Imaging*. 2007;26(4):1153-1161. doi:10.1002/jmri.21090.

122. Glover GH, Pauly JM. Projection reconstruction techniques for reduction of motion effects in MRI. *Magn Reson Med*. 1992;28:275-289. doi:10.1002/mrm.1910280209.

123. Song T, Laine AF, Chen Q, et al. Optimal k-space sampling for dynamic contrast-

enhanced MRI with an application to MR renography. *Magn Reson Med*. 2009;61(5):1242-1248. doi:10.1002/mrm.21901.

124. Vigen KK, Peters DC, Grist TM, Block WF, Mistretta CA. Undersampled projection-reconstruction imaging for time-resolved contrast-enhanced imaging. *Magn Reson Med*. 2000;43(2):170-176. doi:10.1002/(SICI)1522-2594(200002)43:2<170::AID-MRM2>3.0.CO;2-P.

125. Block K, Uecker M. Simple method for adaptive gradient-delay compensation in radial MRI. *Proc Int Soc Magn Reson Imaging*. 2011;19:2816. http://cds.ismrm.org/protected/11MProceedings/files/2816.pdf.

126. Moussavi A, Untenberger M, Uecker M, Frahm J. Correction of gradient-induced phase errors in radial MRI. *Magn Reson Med*. 2014;71:308-312. doi:10.1002/mrm.24643.

127. Peterson P, Månsson S. Fat quantification using multiecho sequences with bipolar gradients: investigation of accuracy and noise performance. *Magn Reson Med*. 2014;71(1):219-229. doi:10.1002/mrm.24657.

128. Reeder SB, Atalar E, Faranesh AZ, McVeigh ER. Referenceless interleaved echo-planar imaging. *Magn Reson Med*. 1999;41(1):87-94. doi:10.1002/(SICI)1522-2594(199901)41:1<87::AID-MRM13>3.0.CO;2-X.

129. Pineda N, Sharma P, Xu Q, Hu X, Vos M, Martin DR. Measurement of hepatic lipid: high-speed T2-corrected multiecho acquisition at 1H MR spectroscopy--a rapid and accurate technique. *Radiology*. 2009;252:568-576. doi:10.1148/radiol.2523082084.

130. Reeder SB, Cruite I, Hamilton G, Sirlin CB. Quantitative Assessment of Liver Fat with Magnetic Resonance Imaging and Spectroscopy. *J Magn Reson Imaging*.

2011;34(4):spcone-spcone. doi:10.1002/jmri.22775.

131. Walsh DO, Gmitro AF, Marcellin MW. Adaptive reconstruction of phased array MR imagery. *Magn Reson Med*. 2000;43(5):682-690. doi:10.1002/(SICI)1522-2594(200005)43:5<682::AID-MRM10>3.0.CO;2-G.

132. Gleich DF. Models and algorithms for pagerank sensitivity. 2009. http://www.stanford.edu/group/SOL/dissertations/pagerank-sensitivity-thesis-online.pdf.

133. Brodsky EK, Holmes JH, Yu H, Reeder SB. Generalized K-space decomposition with chemical shift correction for non-Cartesian water-fat imaging. *Magn Reson Med*. 2008;59(5):1151-1164. doi:10.1002/mrm.21580.

134. Breuer FA, Blaimer M, Heidemann RM, Mueller MF, Griswold MA, Jakob PM. Controlled aliasing in parallel imaging results in higher acceleration (CAIPIRINHA) for multi-slice imaging. *Magn Reson Med*. 2005;53:1-8. doi:10.1002/mrm.20401.

135. Hu H, Li Y, Nagy TR, Goran MI, Nayak K. Quantification of Absolute Fat Mass by Magnetic Resonance Imaging: a Validation Study against Chemical Analysis. *Int J Body Compos Res*. 2011;9(3):111-122.

136. Bismuth H. Surgical anatomy and anatomical surgery of the liver. *World J Surg*. 1982;6(1):3-9. doi:10.1007/BF01656368.

137. Couinaud C, Delmas A, Patel J. *Le Foie: Études Anatomiques et Chirurgicales.* Paris: Masson & Cie; 1957.

138. Liu H, Matson GB. Accurate Measurement of Magnetic Resonance Imaging Gradient Characteristics. *Materials (Basel)*. 2014;7(1):1-15. doi:10.3390/ma7010001.

139. Yu H, Shimakawa A, Hines CDG, et al. Combination of complex-based and magnitude-

based multiecho water-fat separation for accurate quantification of fat-fraction. *Magn Reson Med*. 2011;66(1):199-206. doi:10.1002/mrm.22840.

140. Goceri E, Shah ZK, Layman R, Jiang X, Gurcan MN. Quantification of liver fat: A comprehensive review. *Comput Biol Med*. 2016;71:174-189. doi:10.1016/j.compbiomed.2016.02.013.

141. Wells SA. Quantification of hepatic fat and iron with magnetic resonance imaging. *Magn Reson Imaging Clin N Am*. 2014;22(3):397-416. doi:10.1016/j.mric.2014.04.010.

142. Reeder SB, Robson PM, Yu H, et al. Quantification of hepatic steatosis with MRI: The effects of accurate fat spectral modeling. *J Magn Reson Imaging*. 2009;29(6):1332-1339. doi:10.1002/jmri.21751.

143. Hussain HK, Chenevert TL, Londy FJ, et al. Hepatic fat fraction: MR imaging for quantitative measurement and display--early experience. *Radiology*. 2005;237:1048-1055. doi:10.1148/radiol.2373041639.

144. Centers for Disease Control and Prevention. Overweight and Obesity: Childhood Obesity Facts. https://www.cdc.gov/obesity/data/childhood.html. Published 2018.

145. Schwimmer JB, Deutsch R, Kahen T, Lavine JE, Stanley C, Behling C. Prevalence of fatty liver in children and adolescents. *Pediatrics*. 2006;118(4):1388-1393. doi:10.1542/peds.2006-1212.

146. Ovchinsky N, Moreira RK, Lefkowitch JH, Lavine JE. Liver biopsy in modern clinical practice: a pediatric point-of-view. *Adv Anat Pathol*. 2012;19(4):250-262. doi:10.1097/PAP.0b013e31825c6a20.

147. Manning DS, Afdhal NH. Diagnosis and quantitation of fibrosis. *Gastroenterology*.

2008;134(6):1670-1681. doi:10.1053/j.gastro.2008.03.001.

148. Malamateniou C, Malik SJ, Counsell SJ, et al. Motion-compensation techniques in neonatal and fetal MR imaging. *Am J Neuroradiol*. 2013;34(6):1124-1136. doi:10.3174/ajnr.A3128.

149. Armstrong T, Dregely I, Stemmer A, et al. Free-breathing liver fat quantification using a multiecho 3D stack-of-radial technique. *Magn Reson Med*. 2018;79(1):370-382. doi:10.1002/mrm.26693.

150. Mann HB, Whitney DR. On a test of whether one of two random variables is stochastically larger than the other. *Ann Math Stat*. 1947;18(1):50-60. doi:10.1214/aoms/1177730491.

151. Sawilowsky SS. Misconceptions Leading to Choosing the t Test Over the Wilcoxon Mann-Whitney Test for Shift in Location Parameter. *J Mod Appl Stat Methods*. 2005;4(2):598-600.

152. Bowker AH. A Test for Symmetry in Contingency Tables. *J Am Stat Assoc*. 1948;43(244):572-574. doi:10.1080/01621459.1948.10483284.

153. Venkatesh SK, Hennedige T, Johnson GB, Hough DM, Fletcher JG. Imaging patterns and focal lesions in fatty liver: a pictorial review. *Abdom Radiol*. 2017;42(5):1374-1392. doi:10.1007/s00261-016-1002-6.

154. Lee H, Jun DW, Kang BK, et al. Estimating of hepatic fat amount using MRI proton density fat fraction in a real practice setting. *Medicine (Baltimore)*. 2017;96(33):e7778. doi:10.1097/MD.0000000000007778.

155. Hamer OW, Aguirre D a, Casola G, Lavine JE, Woenckhaus M, Sirlin CB. Fatty liver:

imaging patterns and pitfalls. *Radiographics*. 2006;26(6):1637-1653. doi:10.1148/rg.266065004.

156. Özcan HN, Oğuz B, Haliloğlu M, Orhan D, Karçaaltıncaba M. Imaging patterns of fatty liver in pediatric patients. *Diagnostic Interv Radiol*. 2015;21(4):355-360. doi:10.5152/dir.2015.14505.

157. Fazeli Dehkordy S, Wolfson T, William Hong C, et al. Liver fat reduction following bariatric weight loss surgery is greater in the right lobe of the liver. In: *Proceedings of the International Society for Magnetic Resonance in Medicine 25th*. Honolulu, Hawaii, United States; 2017:0123. http://indexsmart.mirasmart.com/ISMRM2017/PDFfiles/0123.html.

158. Uecker M, Lai P, Murphy MJ, et al. ESPIRiT - An eigenvalue approach to autocalibrating parallel MRI: Where SENSE meets GRAPPA. *Magn Reson Med*. 2014;71(3):990-1001. doi:10.1002/mrm.24751.

159. Armstrong T, Stemmer A, Natsuaki Y, Wu HH. Free-breathing liver fat quantification using an undersampled multi-echo 3D stack-of-radial technique. In: *Proceedings of the International Society for Magnetic Resonance in Medicine 24th*. Suntec City, Singapore; 2016:3837.

160. Armstrong T, Martin T, Stemmer A, et al. Free-breathing fat quantification in the liver using a multiecho 3D stack-of-radial technique: investigation of motion compensation and quantification accuracy. In: *Proceedings of the International Society for Magnetic Resonance in Medicine 25th*. Honolulu, Hawaii, United States; 2017:0363.

161. Hankins JS, McCarville MB, Loeffler RB, et al. R2* magnetic resonance imaging of the liver in patients with iron overload. *Blood*. 2009;113:4853-4855. doi:10.1182/blood-2008-

12-191643.

162. Manco M, Alisi A, Real JMF, et al. Early interplay of intra-hepatic iron and insulin resistance in children with non-alcoholic fatty liver disease. *J Hepatol*. 2011;55(3):647-653. doi:10.1016/j.jhep.2010.12.007.

163. Pierre TGS, Clark PR, Chua-anusorn W, et al. Noninvasive measurement and imaging of liver iron concentrations using proton magnetic resonance. *Blood*. 2005;105(2):855-861. doi:10.1182/blood-2004-01-0177.Supported.

164. Doyle EK, Toy K, Valdez B, Chia JM, Coates T, Wood JC. Ultra-short echo time images quantify high liver iron. *Magn Reson Med*. 2018;79(3):1579-1585. doi:10.1002/mrm.26791.

165. Krafft AJ, Loeffler RB, Song R, et al. Quantitative ultrashort echo time imaging for assessment of massive iron overload at 1.5 and 3 Tesla. *Magn Reson Med*. January 2017. doi:10.1002/mrm.26592.

166. Tipirneni-Sajja A, Krafft AJ, McCarville MB, et al. Radial ultrashort TE imaging removes the need for breath-holding in hepatic iron overload quantification by R2* MRI. *Am J Roentgenol*. 2017;209(1):187-194. doi:10.2214/AJR.16.17183.

167. Gesta S, Tseng YH, Kahn CR. Developmental Origin of Fat: Tracking Obesity to Its Source. *Cell*. 2007. doi:10.1016/j.cell.2007.10.004.

168. Deng J, Schoeneman SE, Zhang H, et al. MRI characterization of brown adipose tissue in obese and normal-weight children. *Pediatr Radiol*. 2015;45(11):1682-1689. doi:10.1007/s00247-015-3391-z.

169. Lonardo A, Ballestri S, Marchesini G, Angulo P, Loria P. Nonalcoholic fatty liver disease:

A precursor of the metabolic syndrome. *Dig Liver Dis*. 2015. doi:10.1016/j.dld.2014.09.020.

170. Modi N, Murgasova D, Ruager-Martin R, et al. The influence of maternal body mass index on infant adiposity and hepatic lipid content. *Pediatr Res*. 2011;70(3):287-291. doi:10.1203/PDR.0b013e318225f9b1.

171. Brumbaugh DE, Tearse P, Cree-Green M, et al. Intrahepatic fat is increased in the neonatal offspring of obese women with gestational diabetes. *J Pediatr*. 2013;162(5). doi:10.1016/j.jpeds.2012.11.017.

172. Modi N, Thomas EL, Uthaya SN, Umranikar S, Bell JD, Yajnik C. Whole body magnetic resonance imaging of healthy newborn infants demonstrates increased central adiposity in Asian Indians. *Pediatr Res*. 2009;65(5):584-587. doi:10.1203/PDR.0b013e31819d98be.

173. Harrington TAM, Thomas EL, Frost G, Modi N, Bell JD. Distribution of Adipose Tissue in the Newborn. *Pediatr Res*. 2004;55(3):437-441. doi:10.1203/01.PDR.0000111202.29433.2D.

174. Ponrartana S, Aggabao PC, Chavez TA, Dharmavaram NL, Gilsanz V. Changes in Brown Adipose Tissue and Muscle Development during Infancy. *J Pediatr*. 2016;173:116-121. doi:10.1016/j.jpeds.2016.03.002.

175. Olhager E, Flinke E, Hannerstad U, Forsum E. Studies on human body composition during the first 4 months of life using magnetic resonance imaging and isotope dilution. *Pediatr Res*. 2003;54(6):906-912. doi:10.1203/01.PDR.0000088064.63106.5E.

176. Bellentani S, Marino M. Epidemiology and natural history of non-alcoholic fatty liver disease (NAFLD). *Ann Hepatol*. 2009;8 Suppl 1:S4-8.

http://www.ncbi.nlm.nih.gov/pubmed/19381118.

177. Haney B, Reavey D, Atchison L, et al. Magnetic resonance imaging studies without sedation in the neonatal intensive care unit: Safe and efficient. *J Perinat Neonatal Nurs*. 2010;24(3):256-266. doi:10.1097/JPN.0b013e3181e8d566.

178. Golan A, Marco R, Raz H, Shany E. Imaging in the newborn: Infant immobilizer obviates the need for anesthesia. *Isr Med Assoc J*. 2011;13(11):663-665.

179. Mathur AM, Neil JJ, McKinstry RC, Inder TE. Transport, monitoring, and successful brain MR imaging in unsedated neonates. *Pediatr Radiol*. 2008;38(3):260-264. doi:10.1007/s00247-007-0705-9.

180. Windram J, Grosse-Wortmann L, Shariat M, Greer ML, Crawford MW, Yoo SJ. Cardiovascular MRI without sedation or general anesthesia using a feed-and-sleep technique in neonates and infants. *Pediatr Radiol*. 2012;42(2):183-187. doi:10.1007/s00247-011-2219-8.

181. Armstrong T, V. Ly K, Murthy S, et al. Free-breathing quantification of hepatic fat in healthy children and children with nonalcoholic fatty liver disease using a multi-echo 3-D stack-of-radial MRI technique. *Pediatr Radiol*. 2018;48(7):941–953. doi:10.1007/s00247-018-4127-7.

182. Leddy MA, Power ML, Schulkin J. The impact of maternal obesity on maternal and fetal health. *Rev Obstet Gynecol*. 2008;1(4):170-178. doi:10.1111/ajo.12253.

183. Gillman MW, Rifas-Shiman S, Berkey CS, Field AE, Colditz GA. Maternal Gestational Diabetes, Birth Weight, and Adolescent Obesity. *Pediatrics*. 2003;111(3):e221-e226. doi:10.1542/peds.111.3.e221.

184. Boney CM, Verma A, Tucker R, Vohr BR. Metabolic Syndrome in Childhood: Association With Birth Weight, Maternal Obesity, and Gestational Diabetes Mellitus. *Pediatrics*. 2005;115(3):e290-e296. doi:10.1542/peds.2004-1808.

185. Newton KP, Feldman HS, Chambers CD, et al. Low and High Birth Weights Are Risk Factors for Nonalcoholic Fatty Liver Disease in Children. *J Pediatr*. 2017;187. doi:10.1016/j.jpeds.2017.03.007.

186. Nobili V, Marcellini M, Marchesini G, et al. Intrauterine growth retardation, insulin resistance, and nonalcoholic fatty liver disease in children. *Diabetes Care*. 2007;30(10):2638-2640. doi:10.2337/dc07-0281.

187. Calkins K, Devaskar SU. Fetal origins of adult disease. *Curr Probl Pediatr Adolesc Health Care*. 2011;41(6):158-176. doi:10.1016/j.cppeds.2011.01.001.

188. Breij LM, Kerkhof GF, Hokken-Koelega ACS. Risk for nonalcoholic fatty liver disease in young adults born preterm. *Horm Res Paediatr*. 2015;84(3):199-205. doi:10.1159/000437054.

189. Faienza MF, Brunetti G, Ventura A, et al. Nonalcoholic fatty liver disease in prepubertal children born small for gestational age: Influence of rapid weight catch-up growth. *Horm Res Paediatr*. 2013;79(2):103-109. doi:10.1159/000347217.

190. Thayyil S, Cleary JO, Sebire NJ, et al. Post-mortem examination of human fetuses: a comparison of whole-body high-field MRI at 9·4 T with conventional MRI and invasive autopsy. *Lancet*. 2009;374(9688):467-475. doi:10.1016/S0140-6736(09)60913-2.

191. Deans HE, Smith FW, Lloyd DJ, Law AN, Sutherland HW. Fetal fat measurement by magnetic resonance imaging. *Br J Radiol*. 1989;62(739):603-607. doi:10.1259/0007-1285-

62-739-603.

192. Berger-Kulemann V, Brugger PC, Reisegger M, et al. Quantification of the subcutaneous fat layer with MRI in fetuses of healthy mothers with no underlying metabolic disease vs. fetuses of diabetic and obese mothers. *J Perinat Med*. 2012;40(2):179-184. doi:10.1515/JPM.2011.122.

193. Reeder SB, Cruite I, Hamilton G, Sirlin CB. Quantitative assessment of liver fat with magnetic resonance imaging and spectroscopy. *J Magn Reson Imaging*. 2011;34(4):729-749. doi:10.1002/jmri.22580.

194. Armstrong T, Ly K V., Wang Y, et al. Free-breathing hepatic fat quantification in children and infants using a 3D stack-of-radial technique: assessment of accuracy and repeatability. In: *Proceedings of the International Society for Magnetic Resonance in Medicine 26th*. Paris, France; 2018:522.

195. Sammet S. Magnetic resonance safety. *Abdom Radiol*. 2016;41(3):444-451. doi:10.1007/s00261-016-0680-4.

196. Zia S. Placental location and pregnancy outcome. *J Turkish Ger Gynecol Assoc*. 2013;14(4):190-193. doi:10.5152/jtgga.2013.92609.

197. Martin T, Liu D, Chanlaw T, et al. Evaluation of placenta motion througout gestation. In: *Proceedings of the International Society for Magnetic Resonance in Medicine 25th*. Honolulu, Hawaii, United States; 2017:4802.

198. Sinding M, Peters DA, Frøkjær JB, Christiansen OB, Uldbjerg N, Sørensen A. Reduced placental oxygenation during subclinical uterine contractions as assessed by BOLD MRI. *Placenta*. 2016;39:16-20. doi:10.1016/j.placenta.2015.12.018.

199. Winkelmann S, Schaeffter T, Weiss S, Eggers H, Doessel O. Simultaneous imaging and R2* mapping using a radial multi-gradient-echo (rMGE) sequence. *J Magn Reson Imaging*. 2006;24(4):939-944. doi:10.1002/jmri.20712.

200. Lu A, Daniel BL, Pauly JM, Pauly KB. Improved slice selection for R2* mapping during cryoablation with eddy current compensation. *J Magn Reson Imaging*. 2008;28(1):190-198. doi:10.1002/jmri.21396.

201. Doyle EK, Toy K, Valdez B, Chia JM, Coates T, Wood JC. Ultra-short echo time images quantify high liver iron. *Magnetic Resonance in Medicine*. http://doi.wiley.com/10.1002/mrm.26791. Published June 22, 2017. Accessed August 28, 2017.

202. American College of Obstetricians and Gynecologists. Committee Opinion No 579: Definition of Term Pregnancy. *Obstet Gynecol*. 2013;122(5):1139–1140. https://journals.lww.com/greenjournal/Fulltext/2013/11000/Committee_Opinion_No_579___Definition_of_Term.39.aspx.

203. The American College of Obstetricians and Gynecologists Task Force. *Hypertension in Pregnancy*.; 2013.

204. The American College of Obstetricians and Gynecologists Task Force. Bleeding During Pregnancy. https://www.acog.org/Patients/FAQs/Bleeding-During-Pregnancy. Published 2016. Accessed March 10, 2018.

205. Hernando D, Vigen KK, Shimakawa A, Reeder SB. R2* mapping in the presence of macroscopic B0 field variations. *Magn Reson Med*. 2012;68(3):830-840. doi:10.1002/mrm.23306.

206. Patel MR, Klufas RA, Alberico RA, Edelman RR. Half-fourier acquisition single-shot turbo spin-echo (HASTE) MR: Comparison with fast spin-echo MR in diseases of the brain. *Am J Neuroradiol*. 1997;18(9):1635-1640.

207. Advanced Normalization Tools (ANTs).

208. Avants BB, Tustison NJ, Song G, Cook PA, Klein A, Gee JC. A reproducible evaluation of ANTs similarity metric performance in brain image registration. *Neuroimage*. 2011;54(3):2033-2044. doi:https://doi.org/10.1016/j.neuroimage.2010.09.025.

209. Avants BB, Yushkevich P, Pluta J, et al. The optimal template effect in hippocampus studies of diseased populations. *Neuroimage*. 2010;49(3):2457-2466. doi:https://doi.org/10.1016/j.neuroimage.2009.09.062.

210. Obuchowski NA, Reeves AP, Huang EP, et al. Quantitative imaging biomarkers: A review of statistical methods for computer algorithm comparisons. *Stat Methods Med Res*. 2015;24(1):68-106. doi:10.1177/0962280214537390.

211. Devore JL. *Probability and Statistics for Engineering and the Sciences*. Vol Seventh.; 2009.

212. Lisa S, Mary R. Advances and applications in fetal magnetic resonance imaging. *Obstet Gynaecol*. 2015;17(3):189-199. doi:10.1111/tog.12203.

213. Shao X, Liu D, Martin T, et al. Measuring human placental blood flow with multidelay 3D GRASE pseudocontinuous arterial spin labeling at 3T. *Journal of Magnetic Resonance Imaging*. 2017.

214. Sharma SD, Hernando D, Horng DE, Reeder SB. Quantitative susceptibility mapping in the abdomen as an imaging biomarker of hepatic iron overload. *Magn Reson Med*.

2015;74(3):673-683. doi:10.1002/mrm.25448.

215. The American College of Obstetricians and Gynecologists. Practice Bulletin No. 134: Fetal Growth Restriction. *Obstet Gynecol*. 2013;121(5):1122–1133. doi:10.1097/01.AOG.0000429658.85846.f9.

216. Sharma D, Shastri S, Sharma P. Intrauterine Growth Restriction: Antenatal and Postnatal Aspects. *Clin Med Insights Pediatr*. 2016;10:67-83. doi:10.4137/CMPed.S40070.

217. Harkness UF, Mari G. Diagnosis and management of intrauterine growth restriction. *Clin Perinatol*. 2004;31(4):743-764. doi:https://doi.org/10.1016/j.clp.2004.06.006.

218. Zhou Z, Han F, Yan L, Wang DJJ, Hu P. Golden-ratio rotated stack-of-stars acquisition for improved volumetric MRI. *Magn Reson Med*. 2017;78(6):2290-2298. doi:10.1002/mrm.26625.

219. Song HK, Dougherty L. k-Space weighted image contrast (KWIC) for contrast manipulation in projection reconstruction MRI. *Magn Reson Med*. 2000;44(6):825-832. doi:10.1002/1522-2594(200012)44:6<825::AID-MRM2>3.0.CO;2-D.

220. Feng L, Grimm R, Block KT obias, et al. Golden-angle radial sparse parallel MRI: combination of compressed sensing, parallel imaging, and golden-angle radial sampling for fast and flexible dynamic volumetric MRI. *Magn Reson Med*. 2014;72(3):707-717. doi:10.1002/mrm.24980.

221. King KF, Ganin A, Zhou XJ, Bernstein MA. Concomitant gradient field effects in spiral scans. *Magn Reson Med*. 1999;41(1):103-112. doi:10.1002/(SICI)1522-2594(199901)41:1<103::AID-MRM15>3.0.CO;2-M.

222. Colgan TJ, Hernando D, Sharma SD, Reeder SB. The effects of concomitant gradients on

chemical shift encoded MRI. *Magn Reson Med*. September 2016. doi:10.1002/mrm.26461.

223. Reeder SB, Sirlin CB. Quantification of liver fat with magnetic resonance imaging. *Magn Reson Imaging Clin N Am*. 2010;18(3):337-357. doi:10.1016/j.mric.2010.08.013.

224. Armstrong T, Dregely I, Han F, et al. Free-breathing fat-water-separated liver MRI using a multi-echo 3D stack-of-stars technique. In: *Proceedings of the International Society for Magnetic Resonance in Medicine 23rd*. Toronto, Ontario, Canada; 2015:0143.

225. Fernndez-Seara MA, Wehrli FW. Postprocessing technique to correct for background gradients in image-based R2/(*) measurements. *Magn Reson Med*. 2000;44(3):358-366. doi:10.1002/1522-2594(200009)44:3<358::AID-MRM3>3.0.CO;2-I.

226. Felker ER, Choi K-S, Sung K, et al. Liver MR Elastography at 3 T: Agreement Across Pulse Sequences and Effect of Liver R2* on Image Quality. *Am J Roentgenol*. 2018;211(3):588-594. doi:10.2214/AJR.17.19288.

227. Serai SD, Dillman JR, Trout AT. Spin-echo Echo-planar Imaging MR Elastography versus Gradient-echo MR Elastography for Assessment of Liver Stiffness in Children and Young Adults Suspected of Having Liver Disease. *Radiology*. 2016;282(3):761-770. doi:10.1148/radiol.2016160589.

228. Wagner M, Besa C, Ayache JB, et al. MR Elastography of the liver: qualitative and quantitative comparison of gradient echo and spin echo echoplanar imaging sequences. *Invest Radiol*. 2016;51(9):575-581. doi:10.1097/RLI.0000000000000269.

229. Kim YS, Jang YN, Song JS. Comparison of gradient-recalled echo and spin-echo echo-planar imaging MR elastography in staging liver fibrosis: a meta-analysis. *Eur Radiol*.

2018;28(4):1709–1718. doi:10.1007/s00330-017-5149-5.